The Dissertation Committee for Kenneth Robert Tarcza Certifies that this is the approved version of the following dissertation:

The Dynamic Failure Behavior of Tungsten Heavy Alloys Subjected to Transverse Loads

Committee:

Eric M. Taleff, Supervisor

Stephan J. Bless, Co-Supervisor

Kenneth M. Ralls

Desiderio Kovar

Krishnaswamy Ravi-Chandar

The Dynamic Failure Behavior of Tungsten Heavy Alloys Subjected to Transverse Loads

by

Kenneth Robert Tarcza, B.S., M.S.

Dissertation

Presented to the Faculty of the Graduate School of
The University of Texas at Austin
in Partial Fulfillment
of the Requirements
for the Degree of

Doctor of Philosophy

The University of Texas at Austin
August, 2004

Dedication

> [38] Then Saul dressed David in his own tunic. He put a coat of armor on him and a bronze helmet on his head. [39] David fastened on his sword over the tunic and tried walking around, because he was not used to them. "I cannot go in these," he said to Saul, "because I am not used to them." So he took them off. [40] Then he took his staff in his hand, chose ***five smooth stones*** from the stream, put them in the pouch of his shepherd's bag and, with his sling in his hand, approached the Philistine.
>
> I Samuel 17:38-40 (NIV)

I dedicate this opus and degree to my faithful, loving, and tolerant wife, Beth, and my awesome kids, Anna and Aaron, for their love and support during these last almost 3 years. I'm eternally indebted to them. They brought balance and perspective to my existence and made this journey enjoyable and memorable. This degree is as much theirs as it is mine.

I also dedicate this effort to my parents, Robert and Elsie Tarcza, and their parents, John and Anna Tarcza, and Paul and Rose Mihaly, respectively, for dedicating their lives to providing their children a better future. Their efforts set me on a trajectory that I never could have imagined in my wildest dreams.

Lastly, this work is dedicated with love and admiration to John and Myrtle Brown, who have taught me so much about life and what really matters. They are an immeasurable blessing and one of the best things about Austin.

Acknowledgements

There are so many folks to thank that I hardly know where to begin. First and foremost, I'd like to thank GEN Paul Kern and COL (Ret.) Frank Davis for their personal involvement in getting me back to graduate school. I am indebted to both for their vision and persistence, as well as the Army for funding this degree program. Similarly, I'm grateful to Terrie Preusse and Dr. Ken Ralls for facilitating my readmission to U.T. in record time in May, 2001. They are the reasons I was able to even get in the door, and Dr. Ralls personal involvement in laying out a degree plan via email was my motivation in choosing the ME/Materials track.

I'd like to thank my advisors and committee members, Drs. Eric Taleff and Stephan Bless, and Drs. Ken Ralls, Desi Kovar, and Krishnaswamy Ravi-Chandar, respectively, for their valuable input and over watch during this process. I'm particularly thankful to Dr. Taleff for his patient mentoring and friendship, and for his perpetually positive outlook and encouragement. He exemplifies all that collegiate faculty at research institutions should aspire to be. I'm also grateful to Dr. Kovar for allowing me to use his profilometer, and likewise to Dr. Ravi-Chandar for granting me access to his lab and drop-tower setup when other plans fell through.

I'm grateful to Dr. Stephan Bless and IAT for facilitating my research, without whose resources I would never have been able to complete my work in under three years. Specifically, I'd like to thank Rod Russell for his friendship and vast involvement in my experimental work. He was truly my second-in-command and puts MacGyver to shame; he also deserves partial credit for this degree. I'd also like to thank Noah Lowenstein, the IAT librarian, for acquiring every piece of research literature my heart desired, and far more than I could read in the time I had available, and T.Rey Calderon for his (usually short notice) graphics wizardry and “giblet” elimination on my micrographs. I’m equally indebted to Dr. Don Berry’s Leander “North Lab” crew, specifically Laura Mangum, Harry Hart, Richard Eaves, Jay Frisch, and Bob Tucker for their tireless efforts with little recognition. They are the “real deal.” Additionally, I’d like to thank Mike Hampton, Ralph Phelps, Jr., and Bruce Campbell at the IAT machine shop for keeping me amply supplied with EDM rod specimens. Thanks are also due to Rachel Gee and Martha Simmons for showing me the ropes on the optical profilometer and the materials lab, respectively. I’m also grateful for Dr. David Littlefield’s and David Fuentes’ input, whose UT-ACES efforts in modeling reverse ballistics interactions through CTH which were invaluable and enlightening in helping to understand experimental observations. Brad Pederson and Dr. Sikhanda Satapathy are also owed thanks for their commiseration and insights along the way.

I’d also like to thank Dr. Todd Bjerke of the Army Research Laboratory for his friendship, insights, findings, and specimen material over the last few years, as well as Dr. Lee Magness for manuscripts and WHA insights early in my research that were most helpful in getting me started. Similarly, I’d be remiss if I didn’t thank LTC Mike Flanagan and John Atkinson, both formerly of the U.S. Army Science and Technology Center – Europe, for working out the details of a research facility tour that proved as enjoyable as it was invaluable to my research.

Next, I’d like to thank James Sanders, the ME Department technical labs manager, for his help into trying to make lemonade out of instrumented Charpy testing lemons, and for his help in compression specimen testing.

Finally, but certainly not least, I’d be remiss if I didn’t thank my fellow grad students for helping me through a maze of coursework, Qualification Exam preparation, and experimental territory on subject matter which I had little exposure to prior to starting work on this degree. Specifically, I’d like to thank Garud Sridhar, Jim Ciulik, Andre´ Albert, Claudia Torres-Garibay, and Paul Green. They made an awesome ad hoc support team for me, without whose help I probably still be struggling through Thermodynamics of Materials and Solid-State Electronic Devices, re-taking Qualification Exams, or polishing tungsten samples.

The Dynamic Failure Behavior of Tungsten Heavy Alloys Subjected to Transverse Loads

Publication No._____________

Kenneth Robert Tarcza, Ph.D.
The University of Texas at Austin, 2004

Supervisors: Eric M. Taleff and Stephan J. Bless

Tungsten heavy alloys (WHA), a category of particulate composites used in defense applications as kinetic energy penetrators, have been studied for many years. Even so, their dynamic failure behavior is not fully understood and cannot be predicted by numerical models presently in use. In this experimental investigation, a comprehensive understanding of the high-rate transverse-loading fracture behavior of WHA has been developed. Dynamic fracture events spanning a range of strain rates and loading conditions were created via mechanical testing and used to determine the influence of surface condition and microstructure on damage initiation, accumulation, and sample failure under different loading conditions. Using standard scanning electron microscopy metallographic and fractographic techniques, sample surface condition is shown to be extremely influential to the manner in which WHA fails, causing a fundamental change from externally to internally nucleated failures as surface condition is improved. Surface condition is characterized using electron microscopy and surface profilometry. Fracture surface analysis is conducted using electron microscopy, and linear elastic fracture mechanics is used to understand the influence of surface condition, specifically initial flaw size, on sample failure behavior. Loading conditions leading to failure are deduced from numerical modeling and experimental observation. The results highlight parameters and considerations critical to the understanding of dynamic WHA fracture and the development of dynamic WHA failure models.

Table of Contents

List of Tables

List of Figures

Chapter 1: Introduction

Tungsten heavy alloys (WHAs) are a category of particulate composites used in defense applications as kinetic energy penetrators. The microstructures in this class of materials typically consist of relatively isolated W grains contained in a continuous matrix of a solid-solution alloy, such as Fe-Ni or Co-Ni. Typical composition is 90-95 weight percent W, with Ni and either Fe or Co in a 7:3 weight percent ratio. These alloys are most commonly processed by liquid-phase sintering, producing W grains with average diameters from 20 to 50 micrometers, as largely influenced by sintering time and temperature.

While the possible WHA failure modes are well understood, the manner in which damage initiates, accumulates, and leads to dynamic failure is not. In particular, the behavior of WHA rods in response to transverse loading under the conditions of ballistic impact is a practical problem whose understanding remains vague. Numerical simulations, such as those produced using the DYNA3D and CTH codes, accurately predict behavior observed experimentally up to the point of fracture initiation. However, the lack of a useful fracture criterion in these codes greatly limits their ability to predict the full physics of failures observed experimentally.

The goal of the present research is to develop, through experimental investigation, a comprehensive understanding of the high-rate fracture behavior of WHA. Mechanical tests spanning a range of “high” strain rates were conducted to generate dynamic fractures resulting from transverse loading of specimens. Recovered specimens were studied to determine the influence of surface condition and microstructure on damage initiation, accumulation, and sample failure under different loading conditions. The understanding of these parameters is shown to be critical to the development of dynamic WHA failure models.

Chapter 2: Background

2.1 TUNGSTEN OVERVIEW

Since being identified in the 16th century, tungsten and its alloys have been of interest in applications requiring metals with high density and strength. As early as the middle-19th century, tungsten's suitability as an alloying element in high-speed tool steels was recognized, leading to patents detailing processing techniques [1]. However, its use was limited to that and incandescent lamp filaments until the production of the first WHA in 1935. Since then, WHA's have grown in importance and applicability due to their high strength, density, and ductility, features which also make them ideally suited to military use as kinetic energy (KE) penetrators.

Typical WHA penetrator alloys are powder-metallurgy (P-M) products processed by liquid-phase sintering (LPS) followed by swaging [2-6]. They consist of relatively isolated, pure W grains from 20 to 50 micrometers in diameter contained in a continuous matrix of a solid-solution alloy such as Ni-Fe or Ni-Co. Examples of a WHA microstructure are shown in Fig. 1.

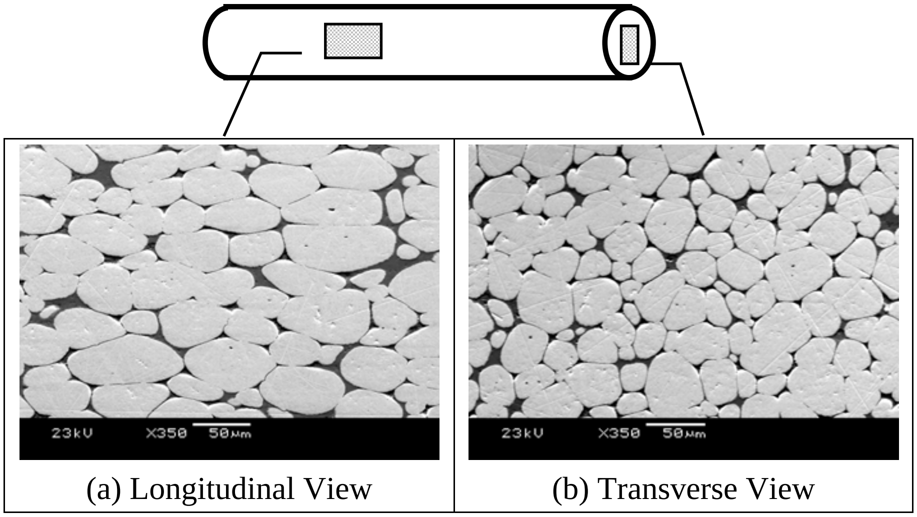

(a) Longitudinal View

(b) Transverse View

Figure 1: Micrographs of WNiFe Alloy Microstructure

A representative composition of WHA is 90-95 weight percent W, with Ni and either Fe or Co in a 7:3 weight percent ratio, all of which have limited solubility (< 1 wt. %) in W [7]. Typical WHA mechanical properties are shown in Table 1. These properties, though, are microstructure dependent and can be greatly influenced by sintering time and temperature [8-14].

Table 1: Typical Tungsten Heavy Alloy Properties [15]

Sintered Density	17.70-18.5 g/cc
Elastic Modulus	350-400 GPa
Poisson’s Ratio	0.28-0.29
Compressive Strength	3500-4500 MPa
Tensile Yield Strength (0.2%)	600-700 MPa
Ultimate Tensile Strength	870-1000 MPa
Fracture Elongation	10-30%
Notched Charpy Impact	0.9-2.8 J

One factor limiting the use of WHA as a KE penetrator material is a lack of detailed understanding concerning the manner in which WHA damage initiates, accumulates, and leads to failure under the conditions of dynamic loading. This is particularly true for the case of transverse loading, which occurs when a rod encounters a side-loading condition. Compounding this issue is the current inability of numerical models used for modeling ballistic interactions to predict fracture. Both of these issues will be discussed in more detail in Chapter 3.

Motivating this research then, is the desire to better understand WHA fracture behavior with the goal of isolating microstructural parameters requiring consideration during the development of dynamic WHA failure models. The contributions of this research include identifying correlations between microstructure, surface condition, and failure conditions, such as stress, strain, and strain rate. Identification is accomplished using a variety of mechanical testing methods and observations of the resulting fracture behaviors and fracture surface morphologies.

2.2 RELEVANT WORK TO DATE

Modern interest in WHA can be traced to the late 1950's and early 1960's [16]. Since then, a vast body of work has been generated, detailing the influence of alloying, processing, temperature and strain rate variation upon alloy behavior. Given the differences in yield stress and work-hardening behaviors of body-centered cubic (BCC) metals, like W, versus that of face-centered cubic (FCC) metals, such as a typical WHA matrix alloy (approximately 50Ni25W25Fe), some of the earliest work considered W and the matrix alloy separately. Because maximum specimen elongation was found to vary with temperature and to correspond directly to the elongation of W particles, W particles were determined to govern the primary deformation characteristics of WHA [17].

Later work established relationships between W content, processing time and temperature, W grain size and contiguity, and alloy strength, revealing the following [18-30]:

1) There are four possible WHA failure modes: 1) W grain cleavage; 2) Matrix failure; 3) W-matrix separation; and 4) Separation of contiguous W grains (W-W grain boundary failure). These are illustrated in Fig. 2. W-W boundaries represent the weakest interface.

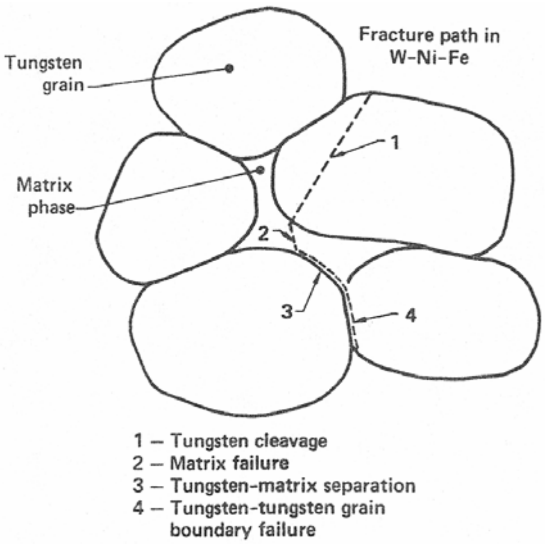

Figure 2: WHA Fracture Path Possibilities [19]

2) Quasi-static tensile, room temperature WHA failure is initiated by cracking at surface W-W grain boundaries (contiguities) oriented nearly perpendicular to tensile axis. This is typically followed by either W transgranular cleavage or W-W failure coalescence via crack bridging through the matrix, which dominates eventual fracture. However, if impurity segregation at W-matrix interfaces occurs, W-matrix separation dominates eventual fracture.
3) Low rate shear failure is also controlled by nuclei originating at the surface of a sample. Shear failure surfaces generally appear flat and have less interior cleavage than do tensile failure surfaces.

4) Ultimate tensile strength (UTS) achieves a maximum at approximately 93 wt. % W, where alloy failure is dominated by cleavage. Above 93 wt.% W, failure is dominated by W-W grain boundary failure; below, failure is dominated by either matrix failure or W-matrix separation.
5) Two keys to improving WHA properties are decreasing W-W grain contiguity by decreasing dihedral angle via chemical additions, and reducing impurities and/or impurity segregation. Conversely, decreasing W-W grain contiguity by increasing sintering temperature increases elongation but reduces YS and UTS.

Much attention has been devoted to WHA behavior at elevated strain rates of 10^2/s to 10^5/s, considering failure under the conditions of tensile, compressive, shear, torsional, and impact loading. It is typically difficult to make a direct comparison of results between different investigations of WHA behavior, even for identical test techniques, due to differences in alloys and processing. Even so, W transgranular cleavage and W-W grain boundary failure tend to dominate high strain rate failure, the former being the most desirable WHA behavior [31-33]. Additionally, cyclic heat treatments have been found to increase high strain rate ductility and Charpy impact energy due to matrix penetration of W-W boundaries [34-37], whereas mechanical alloying [38,39] and cold working [40] have been found to reduce Charpy impact energy over that demonstrated by as-LPS specimens, both being largely functions of W-W grain separation.

Kolsky, or “Split-Hopkinson” Pressure Bar (SHPB), set-ups have been used to generate a variety of WHA strength and failure data [41-61]. An increase in flow stress and decrease in strain to failure are consistently demonstrated with increasing rates of strain. Dynamic tensile failure has been found to initiate due to W-W grain boundary separation; this type of failure was not observed for stresses below the material's yield point, indicating that it was induced by plastic deformation [44]. The dynamic failure sequence that followed was characterized as contiguous W grain crack blunting by matrix plastic flow, then crack tip shear band formation, debonding of W-matrix interface leading to void nucleation, and finally matrix ligament formation and failure. In similar work done under impulsive loading conditions, it was noted that fracture surfaces near crack arrest appeared markedly different from those generated by a running crack [62]. The former was typical of "ductile" behavior and dominated by W grain cleavage and matrix pullout, the latter being typical of "brittle failure" with W-W grain separation predominating. This, however, is in marked contrast to work with W carbide – Co alloys indicating that stable and unstable cracks propagate in the same manner. In these alloys, the features generated by "stable," blunting cracks are indistinguishable from those generated by "unstable," freely running fractures [63,64].

Related and of particular interest is the ductile to brittle transition temperature (DBTT), a well established phenomenon in BCC metals such as W, below which little or no plasticity is demonstrated prior to failure. The DBTT, is generally noted to occur above ~100 degrees Celsius for pure W and at or about room temperature for WHA, though these transition points are known to be influenced by microstructure, alloy composition, and mechanical effects such as surface condition [15,17,19,65-67]. In addition to increased plasticity, a failure mode change generally occurs from primarily W-W grain boundary separation and W grain cleavage below the DBTT to that of ductile rupture in the form of matrix pullout above the DBTT. Also, the DBTT of W and WHA is known to be strain rate sensitive, in that the DBTT increases with strain rate, and material behavior at high strain rates is somewhat analogous to that at low temperatures (below the DBTT) [66,68-71].

Investigators have additionally considered the quasi-static and dynamic behavior of pure, single-crystal, and polycrystalline W, lending useful insight into the fracture behavior of WHA. Anisotropy of various crystal orientations has been identified as having a potentially significant effect on the mechanical properties of pure W, which has been shown to develop a {100} <011> rolling texture, and a <110> fiber texture upon drawing as does WHA upon swaging [2,66,72,73]. {011} and {112} have been identified as the slip planes controlling room temperature deformation; [110] is the most desirable tensile orientation for maximum ductility and minimum work hardening of single crystals [74], while [100] is the preferred orientation for ballistic penetration performance [75,76]. As expected for BCC metals [77], primary cleavage has been found to occur in W single crystals on {100} planes, the preferred cleavage system being {100} <011>, as determined from fracture toughness measurements [78]. Fracture toughness is also found to be extremely temperature dependent, which is attributed to changes in dislocation nucleation versus mobility. River lines on cleaved W grains either follow or significantly deviate from overall crack front direction, depending upon the cleavage system considered [79,80]. Single crystal W fracture behavior has been shown to be indicative of the bending failure behavior of pure, polycrystalline W, which is a function of single versus multi-mode loading and influenced by microscopic and macroscopic texturing [81]. SHPB testing of wrought versus recrystallized pure, polycrystalline W has shown that dynamic tensile failure is surface initiated, controlled by either W grain cleavage or W-W grain separation dependent upon preexisting crystallographic texture, if any. Fracture surface appearance varies with crystallographic texture and strain rate, tending toward W grain cleavage at the highest rates considered regardless of texture [82].

2.3 INFLUENCE OF SURFACE FINISH ON W AND WHA BEHAVIOR

Beyond the aforementioned studies indicating tensile failure initiation of both W and WHA at low and high strain rates is largely surface controlled, it has been shown that loading of a swaged and drawn or rolled pure W (assumed polycrystalline) specimen in transverse-rupture or tensile tests enables flaws in the mechanically distorted surface layer to exert a notch effect, thus unfavorably influencing mechanical properties [83]. Electropolishing (EP) [84] of W surfaces reduces the mobile dislocation density at the surface [85], thereby improving transverse-rupture strength, tensile strength, bend ductility, and elongation. As-swaged P-M tungsten rods have been shown to exhibit increased room temperature ductility with increasing depth of EP [86,87]. Removal of surface material by other means did not produce the same results, and specimens that were EP'd and subsequently scratched with emery paper were observed to exhibit a large reduction in ductility. Bend strength of machined, then EP'd polycrystalline W has also been shown to have a marked improvement with increased EP surface removal and, for a given stress concentration, electrolytically notched tensile specimens exhibited a greater fracture stress than those with machined notches [88,89]. Similarly, the tensile fracture strength and DBTT of pure polycrystalline drawn W wire were shown to be dependent upon the nature of induced surface pre-cracks (spark versus mechanical), whereas specimens that were not pre-cracked exhibited both surface and internally nucleated fractures [90]. Additionally, turning and centerless grinding have been shown to influence the surface micro-flaw distribution of pure polycrystalline W [91].

Similar behaviors hold true for WHA. In research involving tensile testing of centerless ground, then diamond paste polished WHA, it was noted that cleavage of W grains was limited to those on the surface even at temperatures as low as 77K and cleavage was always arrested at a grain-matrix boundary [92]. This was attributed to the detrimental effects of mechanical, as opposed to electrolytic, surface improvement on W ductility. Mechanical working and surface finishing have been shown to adversely affect low strain rate WHA bend ductility [93], and surface finish alone has been identified as influential enough that it may require a separate machining operation to ensure uniformity of behavior and results [94]. For both WHA and pure W, tensile testing at increased strain rates is known to reduce the local fracture strain, leading to increased dynamic notch sensitivity [95]. Additionally, surface carburization has been shown to increase WHA surface hardness while altering the nature of damage at the center of torsional SHPB specimens from primarily shear deformation to that of W grain cleavage [96]. Finally, it has been noted that surface deformation is “different” than that occurring in the interior of WHA due to grain tilting and void nucleation at the surface, leading to a large scatter in the deformation of individual surface W grains [2]; no other details were offered.

Chapter 3: Problem to be Investigated and Research Objectives

3.1 DESCRIPTION OF PROBLEM

Side impact and resulting transverse loading of KE rods can occur when a yawed rod strikes a thick target [97], as shown in Fig. 3. Both the "lateral," Fig. 3(b), and "terminal," Fig. 3(c), penetration stages of yawed impact result in transverse loading and bending and, thus, tensile loading and possible failure of a rod [98]. The same holds true for rod interaction with single [99,100] or multiple [101] thin plate arrays, minus the terminal penetration stage, resulting in "slot cutting" in the plate or plates and lateral loading, erosion, and one reported observation of "hypervelocity gouging" induced failure of a rod [102].

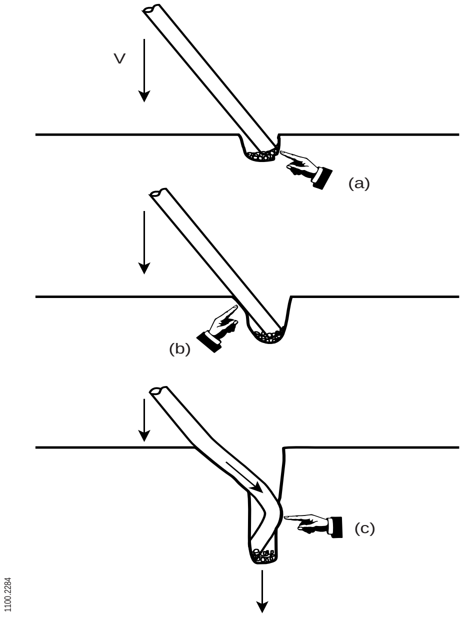

Figure 3: Stages in Yawed Rod Penetration; (a) Primary Penetration; (b) Lateral Penetration; and (c) Terminal Penetration [103]

Due to the lack of an accurate fracture criterion, numerical simulations, such as those produced using the CTH [104] and DYNA3D [105] codes, accurately predict behavior observed experimentally only up to the point of fracture initiation. This greatly limits their ability to predict the full physics of failures observed experimentally and, thus, to accurately predict total penetration from yawed-rod impact. Presently in CTH for example, "fracture" is a numerical phenomenon achieved either when the mean pressure in a model cell as determined by a material constitutive model [106-108] exceeds a designated value, or due to cell boundary tracking and interaction. In either case, affected cells are eliminated and adjoining cells become separated by a void. Unfortunately, it has been demonstrated that removing "numerical fracture" from a representative transverse loading model has no influence on model outcome [109]. Even if this were not true, it is left to the researcher to determine what amount of deformation in a model correlates to the point at which physical fracture occurs.

In contrast, physical fracture occurs when the local stress intensity factor, K_I, for the assumed loading condition of bending resulting in Mode I (opening) tensile failure, exceeds the material's fracture toughness, K_{IC}, leading to an unstable crack running to completion. This relationship is given by [110]:

$$K_{IC} = \sqrt{2\gamma E} \tag{3.1}$$

and

$$\sigma_f = \frac{K_{IC}}{C\sqrt{\pi a}} \tag{3.2}$$

where γ = surface energy

E = elastic modulus

C = geometric constant

a = flaw size

σ_f = failure stress

However, this simple fracture mechanics analysis does not provide a complete solution in that fracture properties of WHA's are known to be anisotropic [111] and dependent upon processing and alloying, as well as temperature, strain rate and loading condition [112-115]. Linear-elastic fracture mechanics solutions for round bars in bending and/or tension are numerous, but require assumptions not necessarily representative of the conditions of yawed-rod impact [116-136].

3.2 RESEARCH OBJECTIVES

The overarching goal of this research effort is to characterize dynamic WHA failure as a function of surface condition under generic transverse loading conditions. The three primary research objectives are to:

1) Characterize damage at different, high strain rates.
2) Quantify the effect of surface condition on damage initiation, accumulation, and the dynamic failure of WHA.
3) Quantify the effect of microstructure on the same.

3.2.1 Damage at Various Strain Rates

There is little prior work devoted solely to the investigation of transverse-loading failure of WHA [137], and not much more that include comparative discussions of the results of varied approaches to induce this type of dynamic failure [138-140]. What work does exist seldom goes beyond the point of identifying loading conditions and the percentage of fracture surfaces devoted to each of the four WHA failure modes. No attempt is made to consider the comparability of test techniques or interpret morphological features generated on fracture surfaces.

A goal of this study is to use two different high strain rate techniques to induce WHA failure by transverse loading. While traditional WHA Charpy testing with standard notched and un-notched specimens is fairly common [141-145], there exists no prior work involving either comparative dynamic three-point bend testing of non-standard geometries or ballistic testing used specifically to induce transverse loading and failure of specimens. Additionally, ballistic impact specimens are seldom recovered in a condition conducive to further analysis. Recovering ballistic rod fragments is critical to this study. Further, gouging has been revealed as a possible failure initiator in long rod – target interactions [102], and a carefully designed test might also serve as a screening criterion for the susceptibility of various ballistic alloys to gouging.

3.2.2 Effect of Surface Finish on Dynamic WHA Failure Behavior

From the literature, a case can be made for the potential influence of surface finish on the dynamic behavior of WHA, but data available are too limited to validate this hypothesis. No data are available in the literature on the influence of surface condition on WHA resistance to transverse loading-related rod failure or its ballistic performance. Accordingly, a goal of the present study is to consider the effect of various surface-finishing techniques upon the failure behavior and fracture morphology of WHA rods. These include as electric-discharge machined (EDM) rods from large bar stock; EDM, then mechanically “superpolished” (SP) rods (prepared by hand using a stainless steel buffing compound with a cotton buffing wheel); EDM, then electropolished (EP) rods; EDM, then centerless ground (CG) between opposing grinding wheels, resulting in round rods of uniform diameter throughout their length; and EDM, then CG, SP, and EP rod, for a total of five distinct surface finishes:

1) EDM
2) EDM and SP
3) EDM and EP
4) EDM and CG
5) EDM and CG, SP, and EP

EP of WHA is somewhat noteworthy in and of itself. EP of pure W [146-149 in addition to instances already cited] and W-Re [150] is not new. However, there is only one reported comparison of polished W versus EP W, but under different loading conditions than those considered in this work [151], and one reported instance of EP a WHA similar to those used in this work [73].

3.2.3 Effect of Microstructure on Dynamic WHA Failure Behavior

A number of investigations have compared the dynamic behavior of different LPS, swaged WHA, some even using alloys similar to those used for this effort [31,152], with one subjecting samples to instrumented 3-point bend testing, as is done for the present investigation [31]. However, no attempts were made to determine the influence of surface condition on alloy behavior or interpret fracture surface morphology beyond identifying the predominant failure modes (W-W grain separation and W grain cleavage). Accordingly, for alloys considered in the present investigation, a goal is to develop an understanding of local and global rod failure behavior through metallographic analysis and fractographic examination of recovered rod fragments. Various aspects of these have been addressed for pure, single crystal W [74,78-81,153-156] and other brittle materials, such as polymers and epoxy resins [for example, 157-161], but never for WHA.

3.3 EXPERIMENTAL APPROACH

Experimental methods used in this work include three-point bend testing at moderate strain rates conducted on an instrumented drop tower, and high-strain- rate transverse load testing conducted in a ballistic format. Each is discussed in greater detail in Chapters 5 and 6, respectively.

Chapter 4: Sample Preparation and Microstructural Observations

4.1 ALLOYS CONSIDERED

Two WHAs were considered in this investigation. One was a WNiFe alloy provided in the form of 32 mm diameter bar stock. The other, a WNiCo alloy, was obtained in 12.7 mm (0.5 in) diameter bar stock. Nominal property data are summarized in Table 2.

Table 2: WHA Property Data

Alloy	93W-5.6Ni-1.4Fe	91.2W-6Ni-2.8Co
Manufacturer	OSRAM-Sylvania	Aerojet Ordnance
Designation	WN308F	Aero-224W
Sintered Density [162]	17.76 g/cc	17.54 g/cc
Processing*	LPS, 20% Swaged	LPS, Proprietary
Elastic Modulus [162]	362 GPa	365 GPa
Tensile Yield Strength (0.2%)*	1186 MPa	958 MPa
Ultimate Tensile Strength*	1255 MPa	1227 MPa
Elongation*	14%	24.5%

* manufacturer-provided data

Because both alloys were swaged and there is little mention in the literature of radial property variation as a result of swaging or its effect on performance [72], microstructural analysis was conducted on samples of virgin bar stock from each material to determine if there were radial differences in microstructure, and to measure grain sizes and aspect ratios.

4.2 METALLOGRAPHIC SAMPLE PREPARATION AND MICROSTRUCTURAL OBSERVATIONS

4.2.1 Metallographic Sample Preparation

Metallographic preparation for all specimens was initially accomplished using a Buehler Datamet™ for initial rough (120 grit) grinding on SiC papers, followed by a

Struers RotoPol-15™ equipped with a RotoForce-1™ automated polisher, using the procedure suggested on the Struers website [163] and shown in Table 3. This was modified at the recommendation of a Struers field representative to use a force of 35N.

Table 3: Struers Metallographic Preparation Procedure for W and WHA

Step	**PG**	**FG 1**	**DP 1**	**DP 2**
Surface	**MD-Piano 220**[1]	**MD-Largo**[2]	**MD-Largo**[2]	**MD-Largo**[2]
Abrasive Type		**DP-Susp. P 9 µm**	**DP-Susp. P 3 µm**	**DP-Susp. P 1 µm**
Lubricant Type	**Water**	**DP-Blue**	**DP-Blue**	**DP-Blue**
Speed [RPM]	**300**	**150**	**150**	**150**
Force [N]	**180**	**180**	**180**	**180**
Holder direction	**>>**	**>>**	**>>**	**>>**
Time [min]	**1**	**4**	**4**	**2**

Notes:

1) MD-Piano™ is a diamond embedded magnetic disc (MD) designed for plane grinding materials in the HV 150-2000 hardness range.
2) MD-Largo™ is a composite magnetic disc (MD) designed for fine grinding of soft materials in the HV 40-150 hardness range using diamond product (DP) suspensions or sprays.

It was found that the recommended steps were not sufficient to remove damage from the initial rough grinding, resulting in W grain distortion as shown in Fig. 4. The observed grain distortion by grinding calls into question reports in literature of grain distortion being achieved through processing [33].

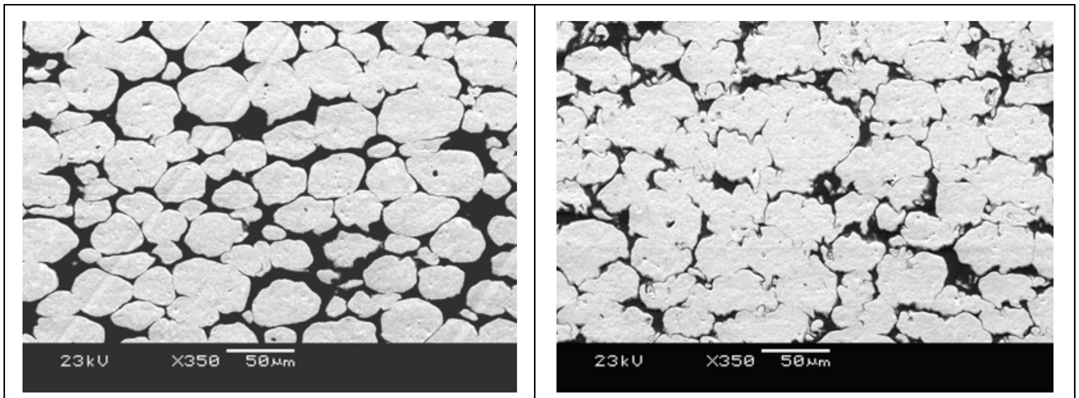

a) Minor Distortion **b) Severe Distortion**

Figure 4: Metallographic Preparation Induced Grain Distortion in a WNiCo Alloy (Longitudinal View)

Murakami's Reagent and Nital were both tried to eliminate this problem [164] and were found to effectively etch the W grains and matrix, respectively. While elimination of existing distortion was particularly helpful, the best approach was found to be sufficient post-grinding polishing, which can remove the grain distortion. Subsequently, the Struers-recommended process evolved to include all suggested times being at least being doubled, and a 16 μm DP (DiaDuo™) suspension step for at least 8 minutes prior to the 9 μm polishing step, while maintaining a 35 N force with automatic force reduction activated for all steps, as reflected in Table 4.

Table 4: Modified Struers Metallographic Preparation Procedure for WHA

Step	PG	FG 1	DP 1	DP 2	DP 3
Surface	MD-Piano 220	MD-Largo	MD-Largo	MD-Largo	MD-Largo
Abrasive Type		DiaDuo 16 µm	DiaDuo 9 µm	DiaDuo 3 µm	DiaDuo 1 µm
Lubricant Type	Water	-	-	-	-
Speed [RPM]	300	150	150	150	150
Force [N]	35	35	35	35	35
Holder direction	>>	>>	>>	>>	>>
Time [min]	2	8	8	8	4

4.2.2 Microstructural Observations

Microstructural analysis was performed on representative travsverse and longitudinal sections from both alloys, as shown in Fig. 5. Observations were made using a JEOL JSM-5610 Scanning Electron Microscope (SEM). W grain size (equivalent circular diameter), area fraction (analogous to volume fraction [165]), and aspect ratio were measured from the micrographs in Fig. 5 with ImageJ, a shareware program available on the National Institutes of Health website [166]. Original SEM micrographs were not amenable to ImageJ analysis, as contiguous W grains, of which there were many in both alloys considered, could not be distinguished during the “thresholding” process and would be counted as a single, large grain. Because of this, grain outlines were traced by

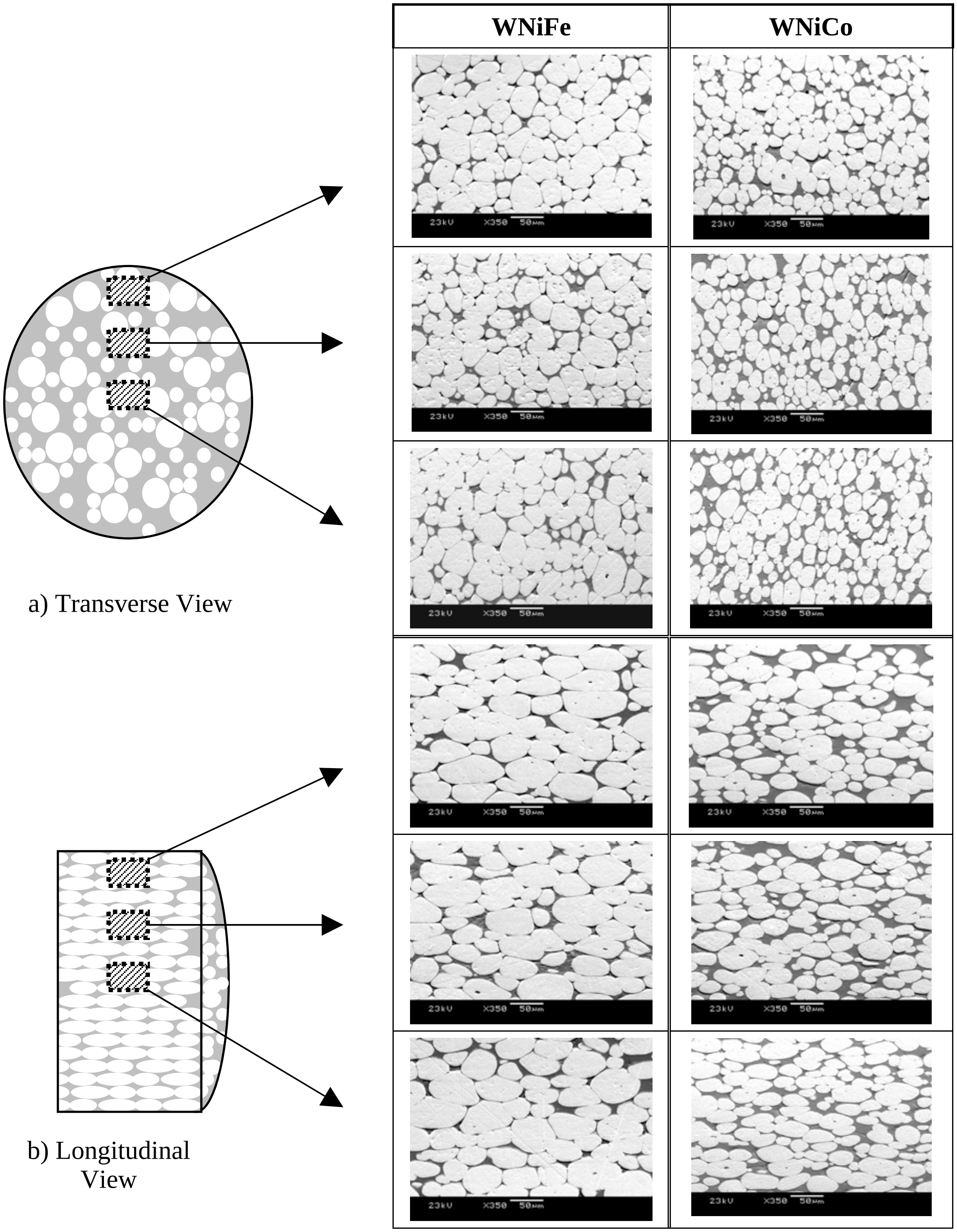

Figure 5: WHA Axial and Radial Cross Sections

hand on paper copies of the micrographs, which were then electronically scanned and subsequently analyzed.

For the WNiFe alloy, the axial micrographs each contained an average of 90 complete grains, and the longitudinal micrographs each contained an average 49 complete grains. Micrographs of the WNiCo alloy each contained an average of 178 and 114 complete grains for the axial and longitudinal sections, respectively. The results, reflected in Table 5, indicate the dimensional measurements plus or minus one standard deviation, providing an idea of the scatter of the measured values.

Table 5: Details of WHA Microstructural Analysis

		WNiFe			**WNiCo**		
		Equiv. Circular Dia. (μm)	**W Area Frac. (%)**	**Aspect Ratio**	**Equiv. Circular Dia. (μm)**	**W Area Frac. (%)**	**Aspect Ratio**
Transverse Sections	**Near Surface**	43 ± 19	82	1.51 ± 0.34	30 ± 13	71	1.43 ± 0.33
	Mid Radius	42 ± 22	83	1.50 ± 0.45	29 ± 13	62	1.53 ± 0.34
	Near Center	43 ± 18	77	1.43 ± 0.27	27 ± 13	62	1.61 ± 0.45
Longitudinal Sections	**Near Surface**	58 ± 26	82	2.00 ± 0.56	38 ± 17	66	2.02 ± 0.55
	Mid Radius	55 ± 23	78	2.27 ± 0.76	35 ± 17	65	2.20 ± 0.69
	Near Center	59 ± 25	82	1.97 ± 0.58	34 ± 16	65	2.33 ± 0.61

As is suggested by a visual inspection of the micrographs in Fig. 5, it was found that both alloys displayed grains with similar aspect ratios elongated due to swaging, but presented fairly uniform microstructures across their radii. The WNiCo alloy’s grains were approximately 50% smaller in both orientations than those of WNiFe alloy. The well-known Hall-Petch relationship, which has been shown to hold true for WHA [14], indicates that WNiCo should have the higher strength of the two alloys, as [167]:

$$\sigma_y = \sigma_o + k_y d^{-1/2} \tag{4.1}$$

where: σ_y = yield strength

σ_o = intrinsic strength

k_y = material constant

d = grain size

A similar trend has been reported for two-phase microstructures, such as WHA, where yield strength is inversely related to the grain size and average matrix thickness between hard phases, by [39,168]:

$$\sigma_y = \sigma_o + k_1 G b \lambda^{-1/2} \tag{4.2}$$

where σ_y = yield strength

σ_o = intrinsic strength

k_1 = material constant

G = shear modulus

b = Burgers vector

and λ = average matrix phase thickness = $\frac{2}{3} d \left(\frac{V_M}{1 - V_M} \right)$

where d = grain size

V_M = matrix volume fraction

These predictions are counter to the σ_y values in Table 2. Therefore, the WNiCo matrix material is likely stronger than the WNiFe matrix material.

A limited number of EDS matrix scans were conducted on the surfaces of specimens of the two alloys. The weight percent matrix compositions of the WNiFe and WNiCo alloys were determined to be approximately 53Ni26W13Fe and 40Ni35W19Co, respectively, with the remainders comprised of minor constituents. The greater amount of W dissolved in the WNiCo matrix may account for its high strength. W grains were determined to contain greater than 96 wt. % W in both alloys, with the remainder consisting of minor constituents. Both alloys were also noted to have some W grain porosity (visible in the micrographs of Figure 5), which is known to have a detrimental effect on the strength of WHA [9,20,21].

4.2.3 Post-Testing Metallographic Sample Evaluation

Recovered WHA rod segments from drop tower testing were reunited, mounted, photographed, and then evaluated to determine the residual bend angle associated with fracture. For ballistic specimens, the characterization process included cleaning and weighing the recovered fragments. Representative segments were then investigated for tensile surface damage and fracture surface characterization using an SEM. Other segments were metallographically prepared for microstructural analysis by SEM. This was done by mounting specimens horizontally (normal to the tensile plane) in a clear thermoplastic, then, using the metallographic procedures previously described, grinding and polishing the specimens to remove approximately half of the cross-section, thereby revealing the interior microstructure, as shown in Fig. 6.

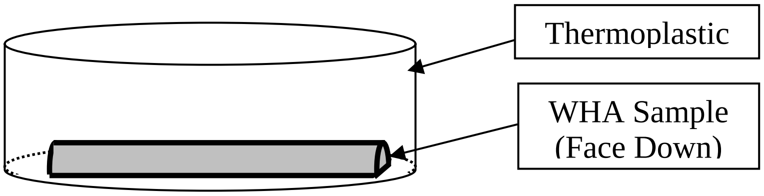

Figure 6: Schematic of WHA Metallographic Specimen

Intuitively, and from preliminary examination, it is known that damage accumulation, if present, is most significant on rod tensile surfaces immediately adjacent to fractures resulting in rod failure. Because of that, and the fact that WHA fractures are known to be largely surface-initiated events, tensile surfaces were the focus of rod surface, normal cross-section, and fracture surface SEM analysis.

4.2.4 SEM Fractography

SEM fractography, the science of interpreting fracture surfaces to deduce information about the conditions present during fracture, was used in this investigation to interpret and understand the implications of generated fracture surface morphologies. As previously discussed, fractographic techniques have been applied to pure W single crystals, but never to WHA's. Though discussions of WHA fracture surface appearance are plentiful [31-39], they have seldom gone beyond identifying loading conditions and the percentage of fracture surfaces devoted to each of the four WHA failure modes. In the present work, it was desired to: 1) understand the origins of fracture surface features; 2) compare fracture surfaces of both alloys, in both ranges of strain rate tested, and with all surface finishes to identify similarities and differences in their appearances; and 3) develop a description of the manner in which fracture initiates and propagates in WHA in terms of local and global crack front development.

This was accomplished through extensive SEM investigation of representative pre- and post-testing sample surfaces, metallographically prepared specimens, and fracture surface analysis. The latter was useful for developing an understanding of local and global fracture propagation characteristics. Specimen surface investigation, both before and after testing, combined with observations of metallographically prepared specimens revealed the causes and nature of WHA damage initiation and accumulation leading to failure.

4.3 ROD PREPARATION

All rods used in these experiments were EDM'd from the original bar stock on a FANUC ROBOCUT α-0iA using 0.254 mm (0.010 in) diameter Hitachi hard brass EDM wire and the standard settings for tungsten carbide. A brief description of the EDM and EP processes are in order at this point, as both proved to have an influential effect on dynamic WHA behavior, though for different reasons. The SP and CG processes were briefly described in Section 3.2.2.

4.3.1 Electric Discharge Machining (EDM) [169]

EDM is based upon the principle of metal erosion by spark discharges. The spark is a transient electric discharge through the space between two charged electrodes, in this case the EDM wire tool and a WHA work piece. Discharge occurs when the potential difference between electrodes is sufficiently large to cause a breakdown in the dielectric fluid medium, resulting in an electrically conductive spark channel. Discharge can be rapidly repeated, each one causing removal of a minute amount of work piece material. The amount of material removed per discharge is a function of the discharge circuit current, electrode characteristics, electrical parameters, dielectric fluid, and thermal capacity, conductivity, and latent heats of melting and vaporization of the work piece material. In general, higher rates of material removal produce rougher surfaces, on the order 25 μm average roughness (Ra), whereas finishing cuts can produce surfaces as fine as 0.6 μm Ra.

4.3.2 Electropolishing (EP) [84]

Electropolishing is the process of anodically smoothing a metal surface in a concentrated acid or alkaline solution. Direct current supplied to the setup results in an oxidation reaction at the anode, a reduction reaction at the cathode, and consumption of the electrolytic bath as anodic metal dissolution products react with the electrolytic solution to form a film at the sample surface consisting of oxidation products. Among other factors, material removal rate is a function of the composition, concentration, and temperature of the electrolytic bath, voltage and current densities, and distance between anode and cathode.

4.3.3 Rod Characteristics

As EDM rods were approximately 3 mm in diameter, 108 mm in length, and had a mass of approximately 13 grams. Each 108 mm length of WNiFe bar stock provided thirty-one samples from four different radii (twelve each from outer and middle rings, six from an innermost ring, and one from the center), as shown in Fig. 7, making rod accountability a necessity.

Figure 7: An EDM WNiFe Rod with Original Bar Stock

EDM rods were assigned an identity that was maintained through subsequent finishing and testing. In cases where identities were "lost," as occurred during CG due to batch processing, the "ring" from which rods originated was still known. In addition and to minimize possible influences due to radial variations, all WNiFe rods used in testing originated almost exclusively from the outer two rings. Each WNiCo bar section provided only six specimens from a single radius plus one from the center, making tracking and usage of this alloy less of an issue. After EDM and each subsequent finishing step, rods were weighed and their length and diameter measured. EDM rods were noted to have diameter variations along their length, having slightly larger diameters at the ends than in the middle, as well as one or two ridges running their length marking the start and/or end point of the EDM pass. To minimize the uncertainty caused by these features, equivalent rod diameters were back-calculated after EDM and each subsequent processing step, using rod mass, length, and documented alloy density from Table 2, where:

$$d = \left(\frac{4m}{\pi l \rho} \right)^{\frac{1}{2}} \tag{4.3}$$

and d = rod diameter

m = rod mass

l = measured rod length

ρ = alloy density

These diameter values were averaged for each alloy and finish combination, which provided a useful measure of the average mass loss and diameter reduction induced by each finishing step.

4.3.4 Sample Surface Finish Variation

Surface finish variation consisted of the mechanical and electrochemical processes outline in Section 3.2.2. Visual inspection alone indicated that the EDM surface finish represented the poorest of the surface finishes studied; this was confirmed by initial surface roughness measurements. Because the response of materials to EDM depends in part upon their thermal properties, it would not be unusual for the constituents of a composite alloy to each react differently to the EDM process. This proved true for WHA, which develops a “heat affected zone” of primarily W-Cu, due the use of brass (Cu-Zn) wire as the electrode, and variable etching of surface constituents, as shown in Fig. 8. Oxides may also be present, though EDS fidelity may not accurately indicate this or the presence of O_2.

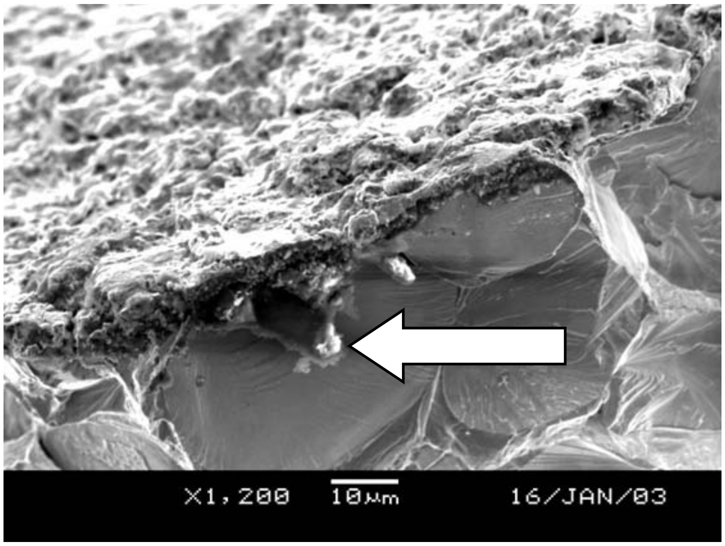

Figure 8: WNiFe Fracture Surface Showing EDM Surface Layer and W Grain Erosion

Of note is the manner in which W grains can be attacked by the EDM process. Given that numerous authors have characterized WHA tensile failure as a surface-initiated process frequently begun by W grain cleavage, this seemed particularly significant. Preparing specimens using only the EDM process with no other treatment might increase the alloy's propensity to fracture or, at a minimum, induce initial flaws that reduce the residual fracture toughness and the energy required to induce and/or propagate fracture. This is alluded to in literature detailing in early work in which spark discharge intentionally was used to induce surface pre-cracks in single crystal W tensile specimens [153-156] and pure polycrystalline drawn W wire [90].

From all indications in prior work, final treatment by EP should rank among the best of the surface finishes being considered. Accordingly, vendors capable of EPing WHA were sought, keeping the focus of this work on failure analysis rather than electrochemical engineering. This proved to be a wise decision, as EP is admitted by some involved with the process for many years to still be very much of an art. The difficulty encountered in this work in locating sources for WHA EP also indicated why there might be so few references to the process in the WHA literature. Success was eventually achieved, though with less than ideal results. EP preferentially attacked the matrix phase, leaving the W grains as raised islands, as shown in Fig. 9. It was not known if this would prove significant given the fracture behavior of WHA. SP and CG surface finishing were similarly obtained from commercial sources.

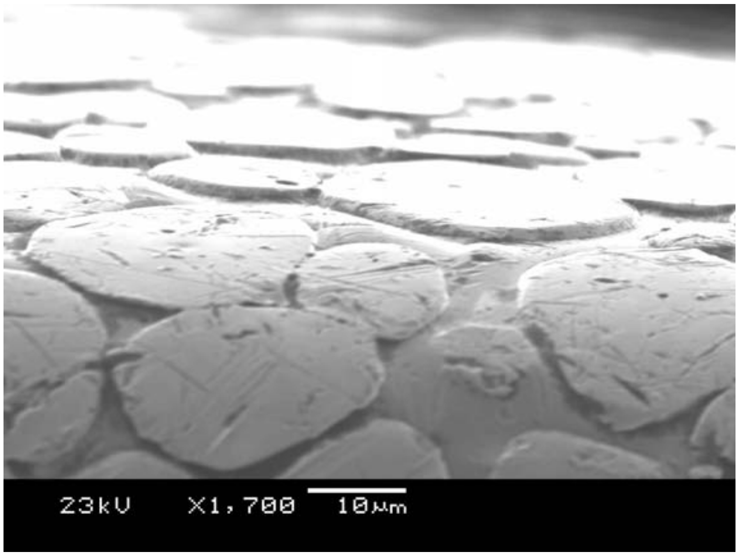

Figure 9: Transverse Edge of an EP WNiFe Rod

From EDM to SP, EP, CG, and CG-SP-EP, surface finishing progressively reduced the equivalent rod diameter (calculated using Eqn. 4.3) and mass, as reflected in Table 6. Each surface condition was studied on both alloys considered in the context of mechanical testing to determine their influence, if any, upon transverse-loading-induced dynamic WHA failure behavior.

Table 6: WHA Rod Parameter Variation Due to Surface Finish Enhancement

Alloy	**Parameter**	**EDM**	**SP**	**EP**	**CG**	**CG-SP-EP**
WNiFe	Avg. Initial Dia. (mm)	3.039	3.037	3.039	3.044	3.037
	Avg. Dia. Reduction From Finishing (mm)	-	0.010	0.049	0.294	0.306
	Avg. Resultant Dia. (mm)	3.039	3.026	2.991	2.751	2.730
	Avg. Initial Mass (g)	13.912	13.905	13.922	13.900	13.886
	Avg. Mass Loss From Finish (g)	-	0.094	0.442	2.485	2.626
	Avg. Resultant Mass (g)	13.912	13.811	13.48	11.415	11.26
	# of rods prepared	62 total	10	5	10	5
WNiCo	Avg. Initial Dia. (mm)	3.055	3.084	3.081	3.039	3.034
	Avg. Dia. Reduction From Finishing (mm)	-	0.012	0.030	0.259	0.260
	Avg. Resultant Dia. (mm)	3.055	3.072	3.051	2.781	2.774
	Avg. Initial Mass (g)	13.912	14.161	14.138	13.735	13.690
	Avg. Mass Loss From Finish (g)	-	0.107	0.274	2.238	2.244
	Avg. Resultant Mass (g)	13.912	14.055	13.864	11.497	11.446
	# of rods prepared	36 total	5	5	10	5

4.4 SURFACE FINISH COMPARISON

In addition to visual comparisons using SEM surface micrographs, the improvements rendered by the various surface finishes were quantified via optical and mechanical profilometry using a WYKO Roughness/Step Test (RST Plus)™, and a Veeco Dektak^3™ equipped with a standard 12.5 μm diamond stylus, respectively. Both devices allow average roughness (Ra), root mean square average roughness (RMS), and other parameters to be determined to an accuracy of 0.01 μm. Other than one system being optical and the other mechanical, the significant difference between the two systems proved to be the available scan (cutoff) length, which could be as much as 30 mm for the Veeco, depending upon the scan rate selected, but was limited to approximately 600 μm for the Wyko at the magnification of interest (10.4x). Both systems offered the disadvantage of being designed for measuring flat specimens, making them challenging to use for measuring surface roughness along the long axis of a cylindrical geometry, as required for this work.

Three to five scans were conducted with each device on rods of each surface finish. Setup parameters for the Veeco™ were a scan length of 30,000 μm, "low" scan speed of 50 seconds, 1200 data points, and a resulting scan resolution of 25 μm/sample. The Wyko™ was used in the vertical scanning-interferometry (VSI) mode using a "bulls-eye" fringe pattern with a scan depth of 20 μm, modulation threshold of 2%, scan back distance of 5 μm, full-view resolution of 368 x 238 pixels, and a low scan speed. The trends of surface roughness reduction with surface finish improvement were similar in data from both techniques, but there were disparities between Ra (and similarly Rq) measurements returned by the two devices. In particular, Ra values were found to increase with cutoff length, most noticeably in scans greater than 10 mm on the Veeco device, due to macro rod profile variations. This is illustrated in the data of Fig. 10.

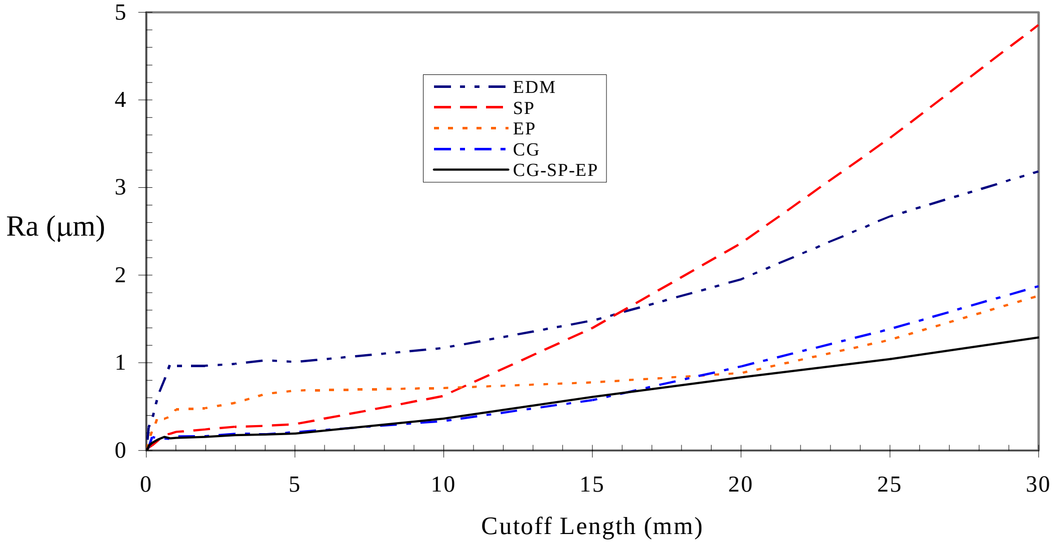

Figure 10: Comparative Veeco WHA Surface Roughness Measurements

Additionally, it was found that at short cutoff lengths, neither device could truly distinguish between SP, EP, and CG-SP-EP, the best three finishes considered, even though there are visible differences between them. Because of these factors, the Ra values determined are at best qualitative comparisons. Comparative surface finishes, which are the averaged value of results determined by both devices at a cutoff length of 600 µm, are reflected in Table 7, as are SEM images of the various surface finishes. Also shown are images of metallographic sample cross-sections, which are discussed in detail in Section 4.5.

Table 7: Comparative WNiFe Surface Finishes

Finish	**~Ra (μm)**	**SEM Image of Rod Surface**	**Metallographic Cross-Sections Revealing Preexisting Damage**
EDM	1.25	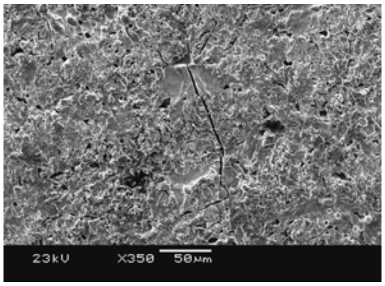	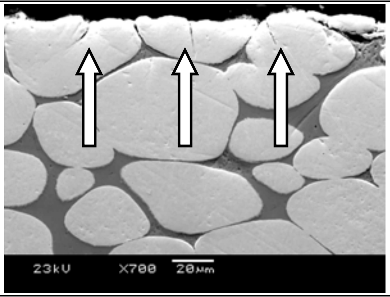
SP	0.28	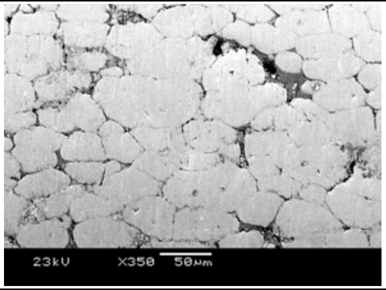	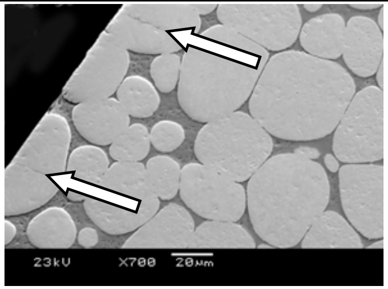
EP	0.61	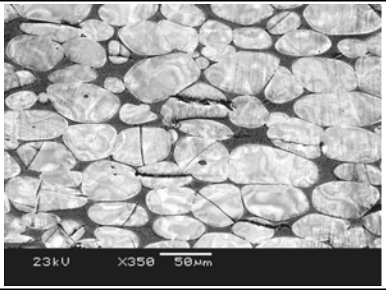	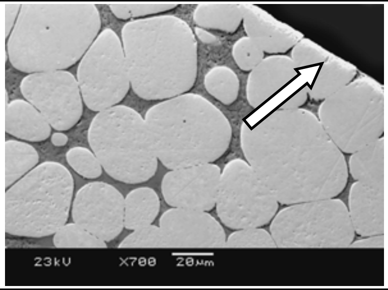
CG	0.26	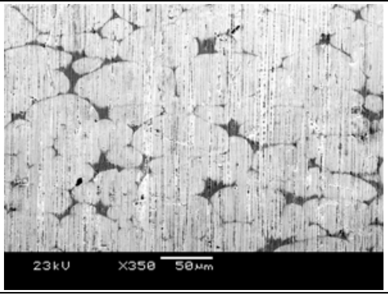	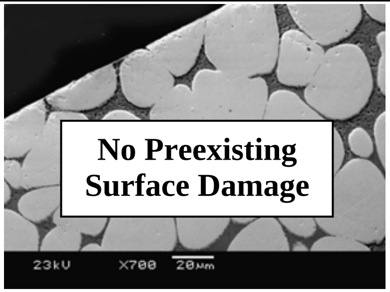
CG-SP-EP	0.27	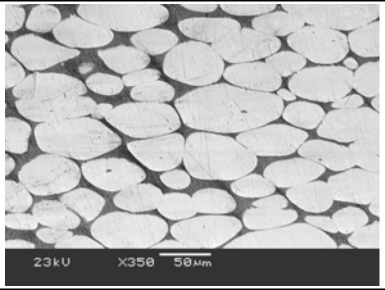	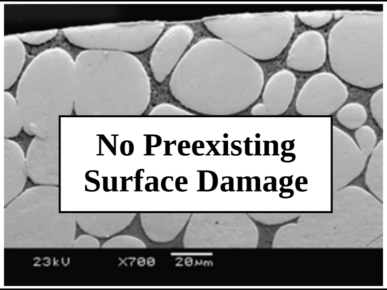

4.5 PROCESSING INDUCED SURFACE DAMAGE

Not realized during initial sample surface comparison was a fundamental difference in the nature of the different surface finishes, causing them to fall into two distinct categories – those with processing-induced surface damage and those without. Upon close SEM examination of the EDM, SP, and EP surfaces of both alloys, it became apparent that significant damage existed in the form of extensive microcracking of W grains. EP surfaces offer the best proof of this, having harmlessly removed the EDM residue layer from the surface and revealing the true nature of the base material. In the EP surface micrograph in Table 7, shown again in Fig. 11 below, fully 33% of complete surface grains in the image (20 out of 60) are either flawed or associated with flaws.

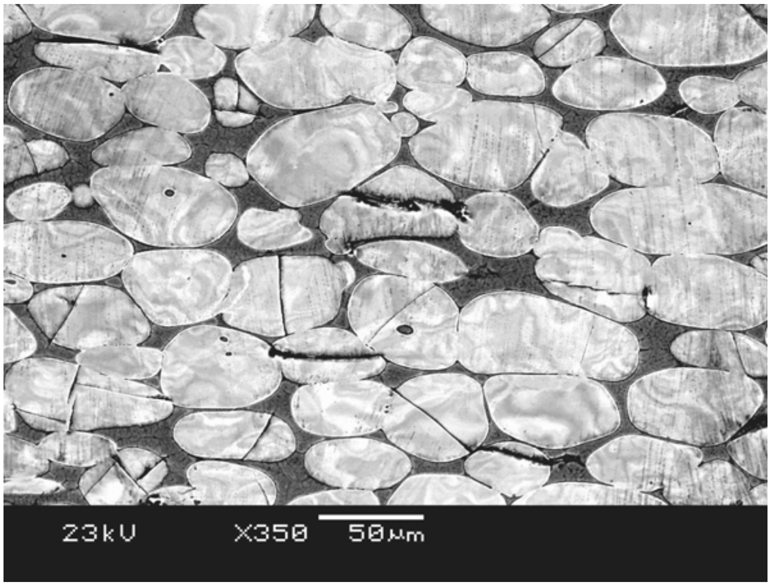

Figure 11: SEM Surface Micrograph of EP WNiFe

The majority of these (19 of 20) are at least partially cleaved. In addition, three matrix cracks and one W-W grain separation are visible, none of which bode well for the alloys' performance at high strain rate.

Because neither alloy's original bar stock or CG-SP-EP specimens presented similar surface damage, it was concluded that the EDM process must be the source of the microcracks. This finding was much more significant than the EDM-induced grain erosion previously identified. Because spark-discharge has been used to intentionally induce sharp pre-cracks in pure single and polycrystalline W [90,153-156], it should come as no surprise that EDM induces microcracks in WHA.

The depth of damage penetration is not revealed in specimen surface images. This could only be determined by studying cross sections from surface-finished samples, which reveal significant cracking in the EDM, SP, and EP specimen surface W grains. These surface cracks sometimes extend through the surface grains and into the matrix beyond, but are usually blunted within grains, as shown in Table 7. It also appears that EP has reduced the initial flaw size, which is in keeping with the equivalent rod diameter reductions per surface finish shown in Table 6.

Quantitative analysis of numerous micrographs detailing the influence of surface finishing on the average initial flaw size confirmed this effect. Surface flaws observed consisted primarily of cleaved W grains, though W-W grain contiguities attacked by EP and exposed W grain pores were also noted, as well as one instance of a cleaved W surface grain revealing striations on the exposed grain face, shown in Fig. 12. Surface flaws appeared in clusters, particularly on the EDM specimens considered, and the variation from high to low flaw density regions was on a microstructural order of less than ten times the average grain size for the respective alloys. Their density per unit surface area was not specifically evaluated, but it can be said that qualitatively, the smaller the average flaw size, the more dispersed the flaws tend to be.

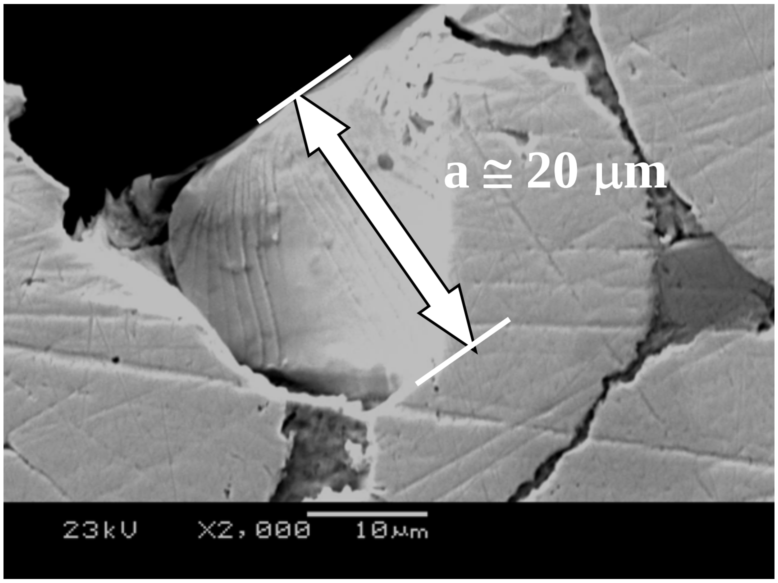

Figure 12: SP WNiFe Cross Section Revealing Cleaved Surface Grain

Flaws were measured by determining their deepest penetration normal to the sample surface. In cases where portions of grains were missing, this flaw size was measured to approximately where the sample surface would have been were the grain intact, as indicated in Fig. 12. These values were averaged and the standard deviations were calculated for each alloy and surface. No less than fifteen measurements were used to determine the average flaw size for a given alloy and finish; the average number of measurements considered for each alloy and finish combination was thirty-one. These data are shown in Table 8 and Figure 13.

Table 8: Measured Average Initial Flaw Sizes

	Measured Average Initial Surface Flaw Size (μm)				
	EDM	**SP**	**EP**	**CG**	**CG-SP-EP**
WNiFe	17.9 ± 8.6	13.3 ± 7.9	8.6 ± 6.8	None Discernible	None Discernible
WNiCo	17.1 ± 9.0	15.1 ± 6.3	7.7 ± 5.8	None Discernible	None Discernible

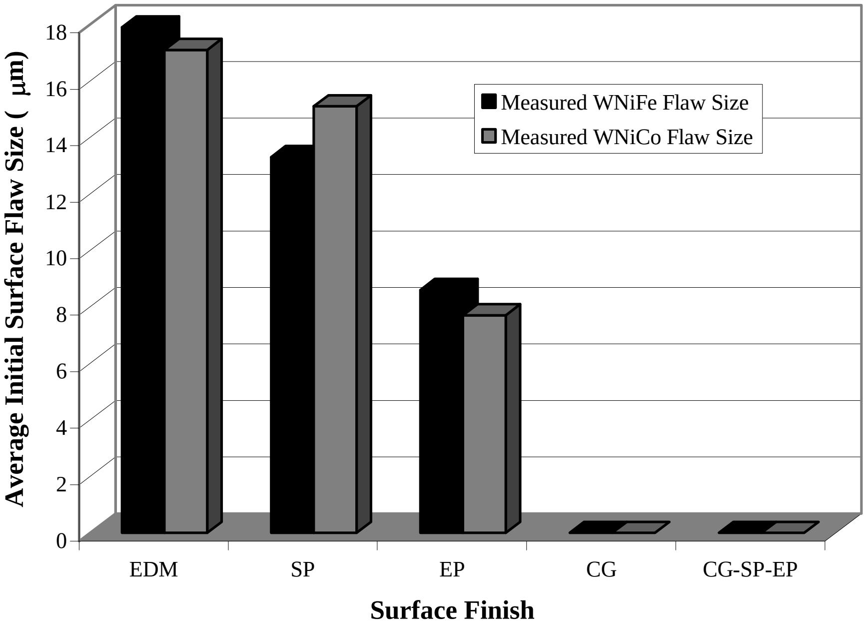

Figure 13: Comparative Average Initial Surface Flaw Sizes

Surprisingly, the average initial flaw size in EDM samples was found to be comparable for both alloys, despite WNiFe having a larger average grain size (see Table 5). No conclusive evidence of preexisting flaws was found on the CG and CG-SP-EP samples of either alloy.

The diameter reduction data in Table 6 indicate that EP should have eliminated all WNiFe surface flaws, when this clearly is not the case. To pursue this line of investigation by comparison with the microstructural observations, the expected average initial flaw size reduction due for each alloy and surface finish combination was computed from equivalent rod diameter reductions as determined from mass loss (shown in Table 6). One-half of the diameter reduction resulting from a finishing step, or the radius reduction, subtracted from the average initial flaw size determined from EDM samples should indicate the flaw size resultanting from that step. These values, plus or minus one standard deviation, are shown in Table 9 and Figure 14. In this case though, standard deviations are less meaningful as the data sets considered usually included ten or fewer values.

Table 9: Expected Average Initial Flaw Sizes Calculated from Rod Diameter Reduction

	Expected Average Initial Surface Flaw Size (μm)				
	EDM*	**SP**	**EP**	**CG**	**CG-SP-EP**
WNiFe	17.9 ± 8.6	12.1 ± 0.9	0	0	0
WNiCo	17.1 ± 9.0	12.1 ± 0.9	2.1 ± 0.5	0	0

* original measured values

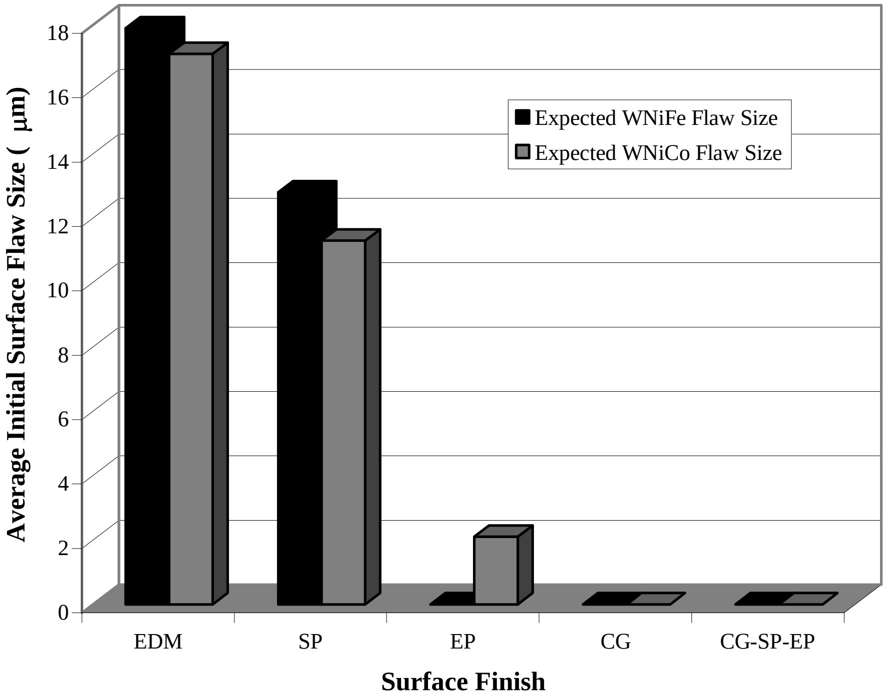

Figure 14: Comparative Expected Average Initial Surface Flaw Sizes Calculated from Rod Diameter Reduction

From these predictions and the microstructural observations, it is concluded that the EDM, SP, and EP surfaces of both alloys will likely have preexisting flaws large and numerous enough to significantly affect the alloys’ fracture behavior under the conditions of dynamic transverse loading. Intrinsic failure mechanisms and surface roughness considerations may play a greater role in the failure behavior of specimens with CG and CG-SP-EP surface finishes.

Chapter 5: Moderate Strain Rate Mechanical Testing

5.1 DYNAMIC 3-POINT BEND TESTING DESCRIPTION AND PROCEDURE

5.1.1 Test Setup

Dynamic 3-point bend testing was conducted with the 2.5 m tall instrumented drop tower shown in Figs. 15 and 16, enabling representative force – time relationships for each alloy and surface finish to be recorded [170]. The loading tup runner block is guided by a 55 mm wide monorail and bolted to a carriage that rides the guide rail. The tup consists of a Dytran Instruments™ model 1051V5 force transducer (5 mV/lbf), equipped with a standard 12.70 mm (0.5 in) diameter Rockwell spherical indenter, and is attached to the runner block by a threaded rod connected to an Al 6061-T6 support arm. The assembled runner block with tup has a mass of 11 kg (~ 24 lbf) and is raised with an electromagnet connected to a hand winch by a pulley and cable. The rail, rail support fin, and sample support are attached to a Al 6061-T6 base plate, all of which are supported by a test stand constructed of 59 mm x 59 mm (1.5 in x 1.5 in) square steel tubing with a 0.49 mm (0.125 in) wall thickness, as shown in Fig. 15(a). After initial proof-of-principle work, the drop height used for all testing in was 1 m, providing a strain rate of approximately 10^3/s.

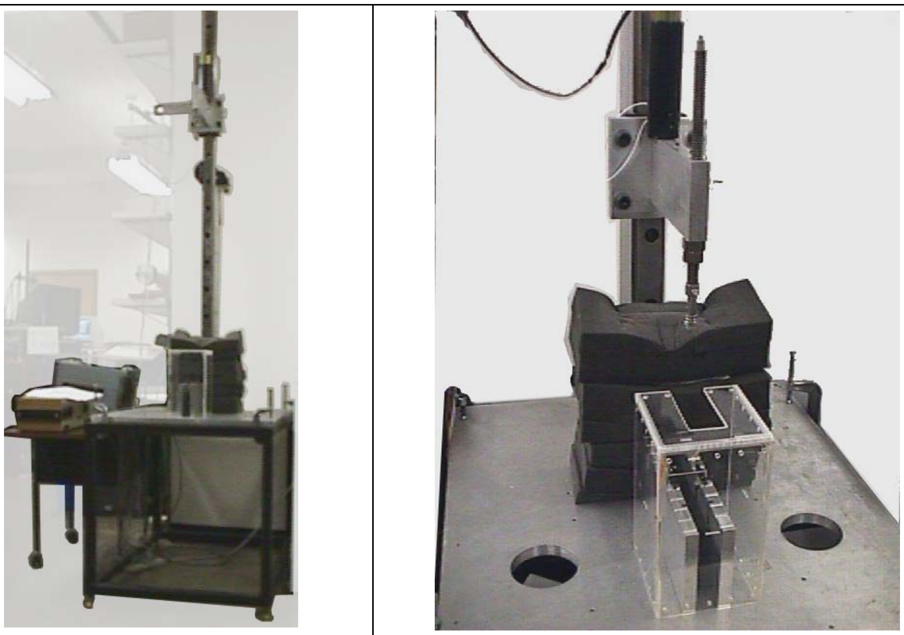

(a) Complete Set Up

(b) Guide Rail, Runner Block, Tup, and Base Plate with Sample Support

Figure 15: Instrumented Drop Tower Impact Tester

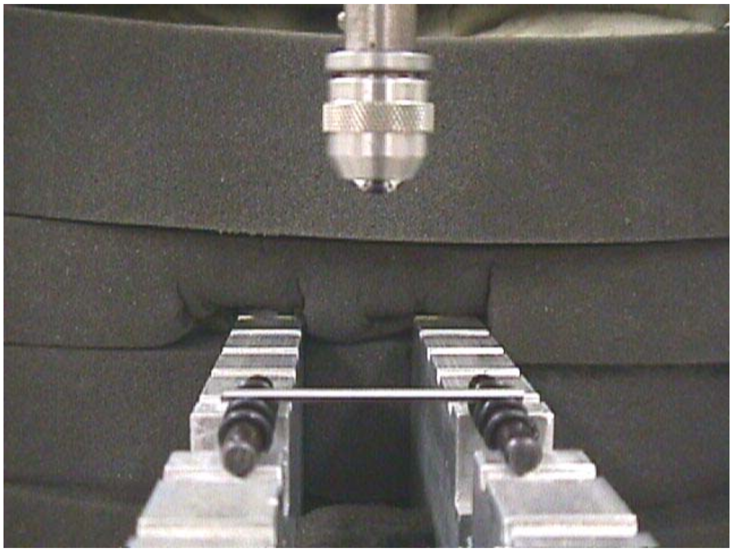

Figure 16: Drop Tower Tup and Sample Support with Sample in Place

Upon release, the tup assembly would accelerate down the rail due to gravity, making contact with specimens supported on 0.49 mm (0.125) diameter rollers resting in cutouts on the sample support. Impact force data were captured by a Tektronix TDS460™ digitizing oscilloscope and stored on a floppy disc. The oscilloscope settings used were 10.0 Ms/s, 500 μm per division on the abscissa, 200 mV/division on the ordinate, and a trigger of 100 mV. After specimen impact, the tup assembly was decelerated with stacked hollow foam rubber blocks filled with clay.

5.1.2 Specimen Geometry

Drop tower testing was conducted using half-length (54 mm), un-notched rods in a dynamic 3-point bend configuration. Though not a standard geometry for this type of testing, rods were chosen for ease of specimen production and so that comparable geometries would be used in both testing techniques considered in this work. This is a valid approach in accordance with ASTM E 23-02, which details standard test methods for notched-bar impact testing of metallic materials, as is usually performed with a Charpy Impact tester [171]. Beyond the standard notched, rectangular geometry, there are multiple alternative geometries outlined that may be substituted, depending upon the type of material to be tested and testing to be done. P-M specimens, for example, can be tested in an un-notched form, and Izod testing may be conducted with a cylindrical geometry, with or without notches; results from differing geometries “cannot be reliably compared.” With that in mind, and because the present investigation was a direct comparison between two testing techniques and two alloys with various surface finishes, it was decided to use the same, cylindrical specimens in both testing techniques.

5.1.3 Data Capture and Analysis

5.1.3.1 Raw Data Manipulation

Raw data captured consisted of a voltage-time history of the loading event, as shown in the plot of Fig. 17. Using the load cell conversion of 5 mV/lbf, raw data plots were converted into force-time relationships. Oscillations in the raw data were repeatable and attributed to elastic wave reflections in the test apparatus. To eliminate these oscillations and simplify analysis of the data of interest in these plots, those from tup initial contact to specimen failure, the data were approximated by curve-fit relationships, also shown in Fig. 17. Second-order polynomials were chosen because they matched the loading curve shape expected (discussed further in Section 5.1.3.3), and their area was found to have an excellent correlation (<< 1% error) with that of the raw data.

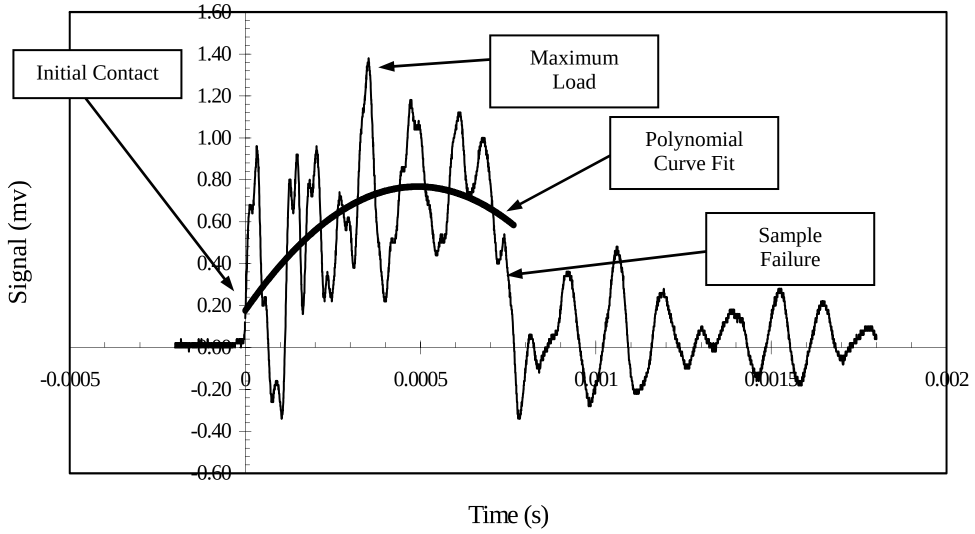

Figure 17: Drop Tower Data Plot for an EDM WNiFe Specimen

5.1.3.2 Bend Angle and Bending Strain Determination

The bend angles of tested specimens were determined from scanned images of the recovered, reassembled specimens. The measurements, repeatable to plus or minus one degree, were averaged for a given surface finish. The average bend angles were used to approximate the maximum fiber bending strain, as shown in Fig. 18 using Eqns. 5.1 and 5.2 [adapted from 172], which would occur at the furthest possible distance from a rod's neutral axis, or at the tensile and compressive surfaces. It was assumed that plane sections remain planar, and that the deformation of specimen fibers would be proportional to their distance from the neutral axis, which would remain unchanged in length.

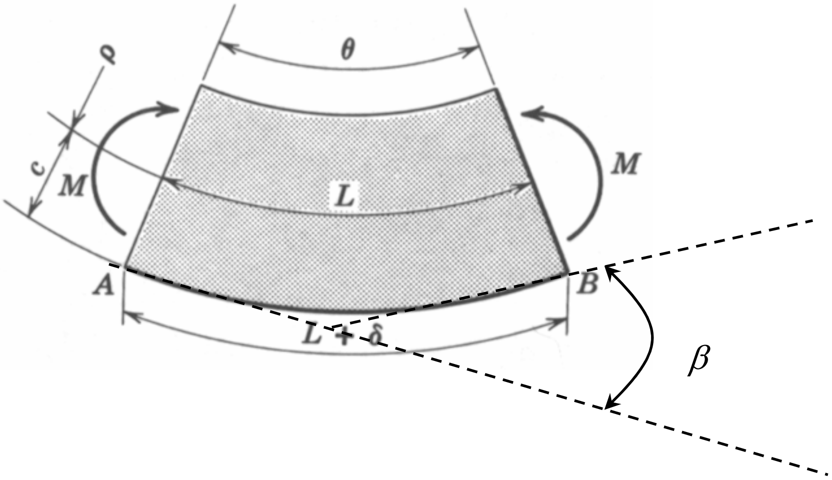

Figure 18: Schematic of Radius of Curvature Resulting From Beam Deflection [adapted from 173]

$$\beta = \theta = \frac{L}{\rho} \tag{5.1}$$

$$\frac{c}{\rho} = \frac{\delta}{L} = e \tag{5.2}$$

where: $\theta = \beta$ = measured minor bend angle

L = length of neutral axis

ρ = radius of curvature

c = distance from rod neutral axis to fiber of interest, or one-half of the surface-finish specific average diameter (shown in Table 6)

e = bending strain

5.1.3.3 Fracture Energy Determination

The force-time relationships can be manipulated to yield force-displacement and fracture energy relationships. Given a known relationship between tup load and time, as well as the mass of the tup assembly, *m*, the position of the tup, *y*, at any time, *t*, is given by [173]:

$$y(t) = \int_0^t \left[v_0 - \int_0^{t'} \frac{F(\xi)}{m} d\xi \right] dt' \qquad (5.3)$$

where v_0 = tup velocity at impact

$F(\xi)$ = load variation with respect to time

Once the load-displacement relationship is known, the energy absorbed by a specimen, *E(t)*, which is the area under the load-displacement curve, can be determined from:

$$E(t) = \int_{0}^{s(t)} F(s')\,ds' \tag{5.4}$$

Load-displacement relationships also allow for distinguishing between fracture initiation (pre “maximum-load”) energy, fracture propagation (post “maximum-load”) energy, and final (post brittle) fracture energy, as has been applied to instrumented Charpy impact testing and is shown in Fig. 18 [174,175]. If the influence of surface finish has a significant effect on impact behavior, it is expected to be revealed, at a minimum, through differences in the fracture initiation energy for otherwise identical samples.

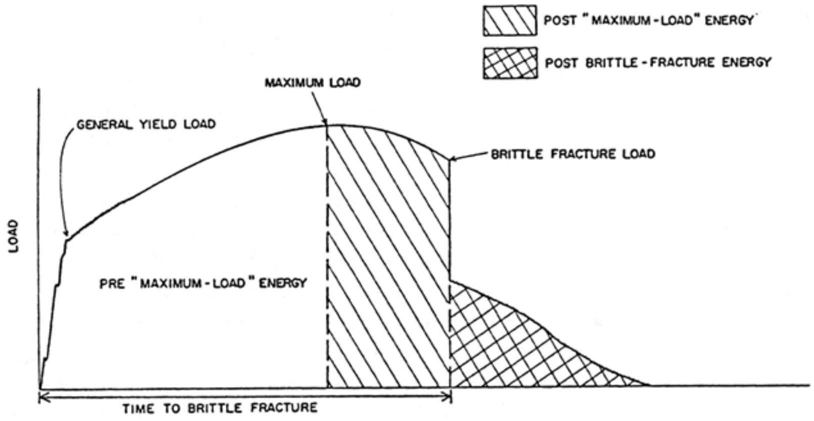

Figure 19: Idealized Load-Time Trace for a Charpy V-Notch Specimen [175]

The load-displacement relationships for each test were second-order polynomial curve-fitted, providing a good match with the idealized curve shape shown in Fig. 18. Though this may artificially induce symmetry around the peak load values, the same bias was applied to all data and did not affect the fracture energy calculations. The curve-fit coefficients were averaged to produce a characteristic equation and loading curve for a given alloy-surface finish combination. These curves were then integrated to yield representative fracture initiation, fracture propagation, and total fracture energies for that alloy finish combination; no post brittle fracture energy was noted for any specimen. Finally, the energy values were normalized by the rod mass, yielding specific fracture energy values for the alloy-surface finish combinations tested.

5.1.3.4 Elastic-Plastic Analysis

Using basic beam theory, the force-displacement relationships can be used to determine the yielding and full plastic moments associated with specimen loading and failure by considering the experimental geometry, shown in Fig. 20, and the average diameter reductions caused by the various surface finishes (shown in Table 6).

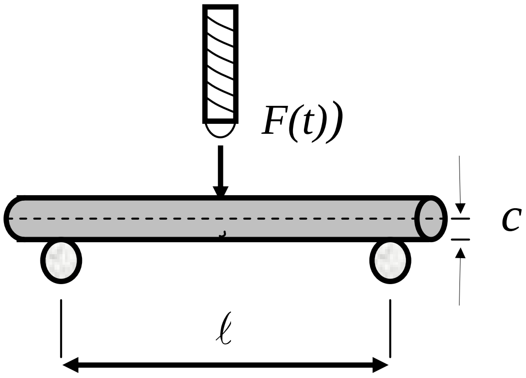

Figure 20: Drop Tower Setup Geometry

Rods experience maximum tensile (and compressive) stresses on their outer surfaces at a distance of the rod’s radius from the neutral axis. From elastic theory, the moment experienced by a beam subjected to a three-point bending load is:

$$M_E = \frac{F_A \ell}{2} \tag{5.5}$$

where M_E = elastic moment

F_A = applied load

ℓ = span length, or 46 mm (1.81 in)

From an analysis of yielding at the outer fiber:

$$M_y = \frac{\sigma_y I}{c} \tag{5.6}$$

and $$I = \frac{\pi r^4}{4} \tag{5.7}$$

where: M_y = yielding moment

σ_y = yield stress (from Table 2, 1186 MPa for WNiFe)

I = mass moment of inertia for a rod cross section

$c = r$ = distance from rod neutral axis to surface of interest,

i.e. rod radius, or ~ 1.5 mm

Setting Eqns. 5.5 and 5.6 equal to each other and solving for the force at yielding, F_y:

$$F_y = \frac{\pi r^3}{2\ell}\sigma_y \tag{5.8}$$

≅ 141 N for a 3.0 mm WNiFe diameter rod

The yield force predicted by Eqn. 5.8 can be used to normalize the applied force, F_A, and determine if the loading conditions for each set of surface finishes exceed that required for yielding to occur.

Similarly, the plastic moment, M_p, and plastic force, F_p, can be calculated, assuming that the material is perfectly plastic [176]:

$$M_p = \sigma_y Z \tag{5.9}$$

and

$$Z = A\frac{(y_1 + y_2)}{2} = A\bar{y} \tag{5.10}$$

where: Z = plastic modulus for a circular cross-section

$A = \pi r^2$ = rod cross-sectional area

$y_{1,2}$ = distance to the rod neutral axis from the centroids of the areas above and below the rod neutral axis, respectively, or $\frac{4r}{3\pi}$ for both

$\bar{y}$ = average distance from section centroids to neutral axis

and

$$F_p = \frac{8r^3}{3\ell}\sigma_y \tag{5.11}$$

Normalizing the result of Eqn. 5.11 with that from Eqn. 5.8 reveals the loading condition beyond which full plastic deformation will occur for a cylindrical geometry, or:

$$\frac{F_p}{F_y} = \frac{\frac{8r^3}{3\ell}\sigma_y}{\frac{\pi r^3}{2\ell}\sigma_y} = 1.70 \tag{5.12}$$

5.2 EXPERIMENTAL RESULTS

5.2.1 Drop Tower Physical Results

The alloys considered in this investigation exhibited markedly different behavior in drop tower tests. WNiFe specimens of all surfaces finishes, less CG-SP-EP, were easily broken at room temperature, whereas WNiCo specimens displayed far greater room-temperature ductility and could only be broken after immersion in liquid N_2 (LN_2). Three to for trials were conducted at each surface condition. At room temperature, the WNiFe CG-SP-EP specimens did not break. Room temperature SP and EP WNiFe specimens displayed comparable bend angles sustained in conjunction with fracture. WNiFe specimens tested after immersion in LN_2 display no measured ductility and failed with no measureable bend angle. Representative specimens of both alloys, with average minor bend angles determined from recovered specimens (θ, in parentheses), are shown in Table 10.

Because of the room temperature WNiCo results, additional experiments were conducted while allowing the WNiCo alloy to warm from LN_2 temperatures. This was done with the goals of determining a ductile-to-brittle transition range and of demonstrating behavior comparable to that of the Fe alloy behavior at room temperature. It was determined that specimens warmed from –196^{o}C to approximately –140^{o}C in the time it took to remove them from the LN_2 bath, place them on the sample supports, and release the tup (~5 seconds). However, WNiCo behavior proved extremely inconsistent among these tests because of a lack of adequate temperature control. Repeated tests after identical warming delays produced widely varying results. Eventually, it was concluded that the WNiCo DBTT must fall in a narrow range between –70^{o}C and –30^{o}C, and this technique was not further pursued. Consequently, no clear surface-finish associated improvement trend could be established for this alloy from drop tower tests.

Table 10: WHA Drop Tower Physical Results

Surface Finish	**WNiFe**		**WNiCo**	
	Room Temperature	**After LN$_2$ Immersion**	**Room Temperature**	**After LN$_2$ Immersion**
EDM	(14°) 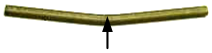	(0°) 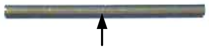	**_(55°)*_** 	(1°) 
SP	(25°) 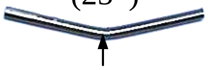	(0°) 	Not Tested	Not Tested
EP	(24°) 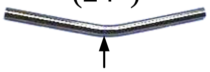	Not Tested	Not Tested	Not Tested
CG	(28°) 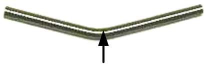	(0°) 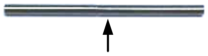	Not Tested	(5°) 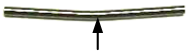
CG-SP-EP	**_(35°)*_** 	Not Tested	Not Tested	(6°) 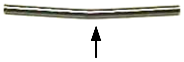

↑ = site of fracture, * = did not break

5.2.2 Bending Strain Determination

With surface finish improvement and/or initial flaw size reduction, WNiFe specimens exhibited an increase in average bend angle sustained prior to fracture. These angles were used to calculate maximum fiber strain at the tensile surfaces in accordance with Eqns. 5.1 and 5.2. The length of neutral axis, *L*, over which bending occurred was determined from recovered specimens to be approximately 5 mm for all surface finishes. The resulting radii of curvature and calculated bending strains are shown in Table 11.

Table 11: WHA Drop Tower Bending Strain Data

Surface Finish	**WNiFe**						**WNiCo**					
	Room Temperature			**After LN_2 Immersion**			**Room Temperature**			**After LN_2 Immersion**		
	θ	ρ	e	θ	ρ	e	θ	ρ	e	θ	ρ	e
EDM	14	20.46	0.07	0	N/A	0.00	55	5.21	0.29	1	286.48	0.01
SP	25	11.46	0.13	0	N/A	0.00	Not Tested			Not Tested		
EP	24	11.94	0.13	Not Tested			Not Tested			Not Tested		
CG	28	10.23	0.13	0	N/A	0.00	Not Tested			5	57.30	0.02
CG-SP-EP	35	8.19	0.17	Not Tested			Not Tested			6	47.75	0.03

5.2.3 Fracture Energy Determination

The recorded room temperature WNiFe voltage-time relationships were manipulated as discussed in Section 5.1.3.3 to yield force-displacement relationships and curve-fitted characteristic loading curves. The loading curves for the various surface finishes are shown in Fig. 21. The CG-SP-EP curve was included, even though the majority of these specimens did not break in testing, because the characteristic loading curves of the unbroken and broken specimens matched very well. It was felt that the "average" curve for this finish was fairly representative of both outcomes. The fracture and specific fracture energies for each finish are shown in Table 12.

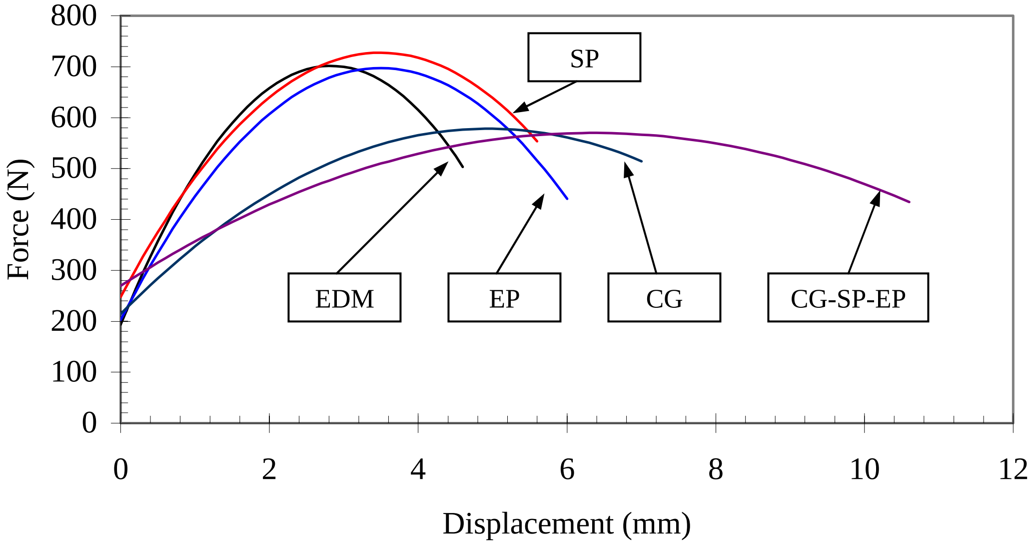

Figure 21: Comparative WNiFe Drop Tower Loading Curves

Table 12: Computed WNiFe Drop Tower Data

	Curve-Fitted Load Parameter (N)			Curved-Fitted Fracture Energy (J)			Specific Fracture Energy (J/g)		
	Yield	**Max**	**Fracture**	**Init.**	**Prop.**	**Total**	**Init.**	**Prop.**	**Total**
EDM	194	702	495	1.508	1.142	2.650	0.217	0.164	0.381
SP	248	728	553	1.985	1.412	3.397	0.287	0.204	0.492
EP	208	697	430	1.857	1.559	3.416	0.276	0.231	0.507
CG	215	578	508	2.256	1.205	3.461	0.395	0.211	0.606
CG-SP-EP	270	570	435	2.978	2.229	5.207	0.529	0.396	0.925

The normalized specific fracture energy data in Table 12 reflects quantitatively what was qualitatively conveyed by the physical results shown in Tables 10 and 11. Surface finish improvement has resulted in a marked improvement in rod performance, illustrated by increasing facture energy with average initial flaw size reduction for the

EDM, SP, and EP finishes, and with surface finish improvement alone for the CG and CG-SP-EP finishes (in which preexistent surface flaws were not observed). CG-SP-EP specimens showed the greatest improvement, exhibiting a remarkable 143% increase in total specific fracture energy over EDM specimens, and a 53% increase over CG specimens. The latter is of particular note and contrasts with the notion that the surface finishes are comparable due to their lack of initial flaws and nearly identical measured Ra values. Even the least aggressive surface treatment, SP, resulted in a 29% improvement in total specific fracture energy over that of EDM surfaces. These data, plotted in Fig. 22, reflect linear curve fits extrapolated to smaller initial flaw sizes. Data points for the CG and CG-SP-EP finishes assume the initial flaw size to be equal to the average Ra values for these finishes (0.26 and 0.27, respectively) and are omitted from the curve fit analysis.

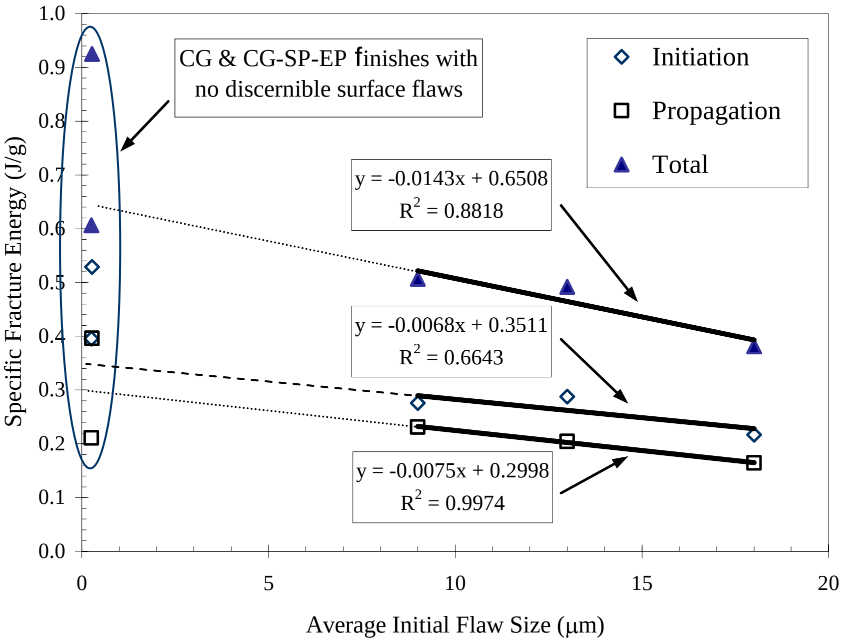

Figure 22: WNiFe Specific Drop Tower Fracture Energy - Average Initial Flaw Size Relationship

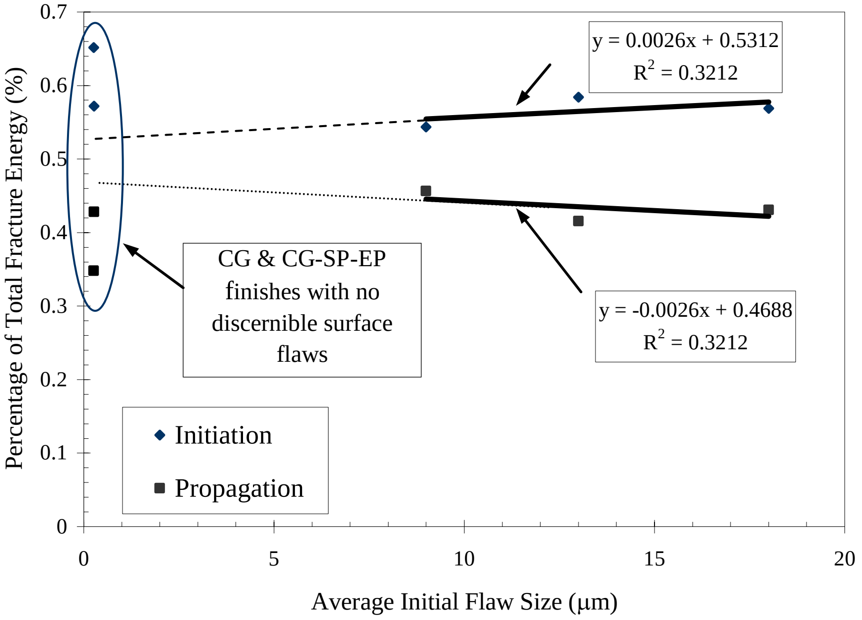

Figure 23: Percent Contribution of Initiation and Propagation Energies to Total Fracture Energy

Fig. 22 indicates increases in specific fracture initiation, propagation, and total energies with reduction of the average initial flaw size. Fig. 23 indicates that the contributions of fracture initiation energy and fracture propagation energy to the total fracture energy remain fairly constant at about 60% and 40%, respectively. This analysis was not attempted for the WNiFe alloy after LN_2 immersion, or for the WNiCo alloy at any temperature.

5.2.4 Elastic-Plastic Analysis

Using the approach detailed in Section 5.1.3.4, the comparative drop tower loading curves for WNiFe reflected in Fig. 21 were normalized by a diameter-dependent F_y (yield force) value of approximately 141 N. These data are reflected Fig. 24, along with the F_p/F_y (plastic-yielding) force ratio of 1.70, beyond which fully-plastic bending is expected to occur. It is clear from this plot that under drop tower loading conditions, the WNiFe alloy is almost immediately pushed far beyond its yielding and fully plastic limits, regardless of surface finish and well before fracture occurs. The normalized maximum force increases slightly with surface finish improvement, while rod displacement and, thus, energy absorbed by the rods increase significantly as surface finish is improved.

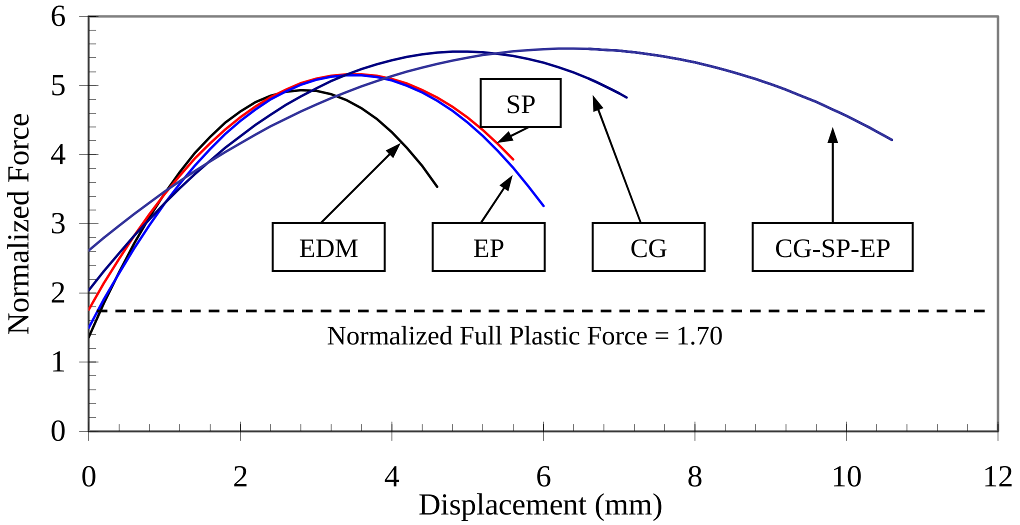

Figure 24: Room Temperature WNiFe Drop Tower Force Normalized by the Force Required for Yielding

5.3 DROP TOWER SPECIMEN SEM ANALYSIS

5.3.1 Exterior Tensile Surfaces

Clear trends emerge upon studying tensile surfaces approaching and adjacent to fracture surfaces. For all surface finishes, damage (i.e. surface cracks) progressively accumulates along surfaces approaching the final failure, becoming most severe immediately adjacent to the final facture. However, for specimens whose surfaces had preexisting flaws in the form of W grain microcracking (EDM, SP, and EP), damage is extensive and includes significant opening and sometimes linking of these microcracks. Upon tensile loading of the surface due to bending of the rod, microcracks normal to the tensile axis open quickly and easily; those parallel to the tensile axis appear to remain largely unaffected. Subsequently, microcracks normal to the tensile axis link to other opening microcracks in contiguous W grains, only passing through the matrix or around grains when necessary, to form large fractures dominated by W grain cleavage. Eventually, one of these large fractures close to the point of greatest tensile stress on the rod surface becomes unstable, causing final fracture of the rod while simultaneously quenching nearby fractures. Regularity was noted in the spacing of surface fractures created during testing. Parallel fractures were usually no farther than 4-6 grain lengths apart or longer than about 3-6 grain widths (~200 μm). Examples of sample tensile surfaces adjacent to final fracture are shown in Fig. 25.

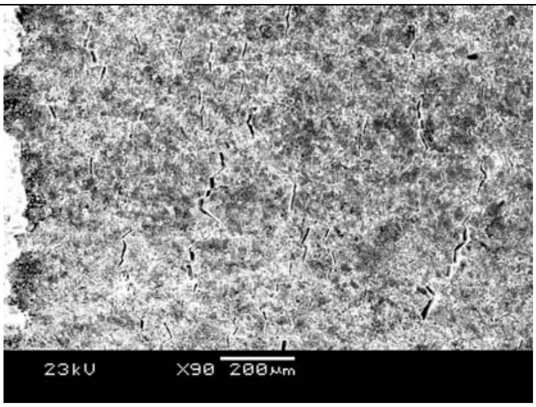

(a) EDM

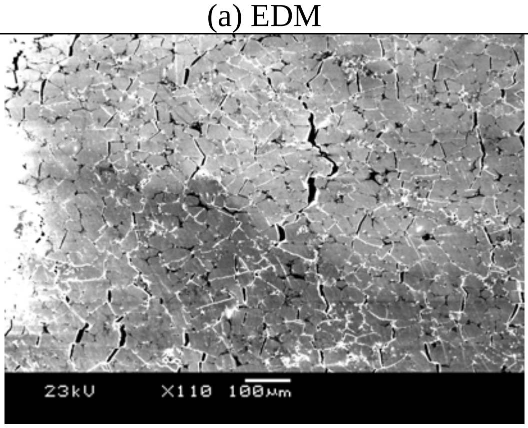

(b) SP

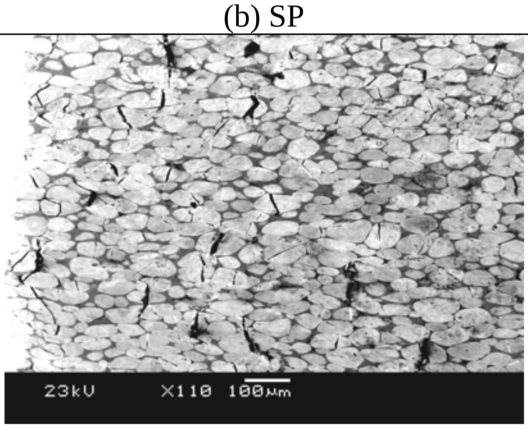

(c) EP

Figure 25: Room Temperature WNiFe Drop Tower Tensile Surface Damage Accumulation Adjacent to Fracture at Left (Tensile Stress Orientation ←→)

In contrast, for specimen surfaces with an absence of preexisting flaws (CG and CG-SP-EP), surface damage from testing is much more limited and localized to the region adjacent to final fracture. The resultant fractures are still almost entirely W cleavage. This was particularly true in the case of the one CG-SP-EP specimen that broke, where much of the resultant damage appears no more severe then preexistent damage visible most clearly in the SP and EP specimens. A schematic comparison between tensile surfaces adjacent to fracture in specimens with and without preexisting surface flaws is shown in Fig. 26. CG and CG-SP-EP tensile surface SEM images are shown in Fig. 27.

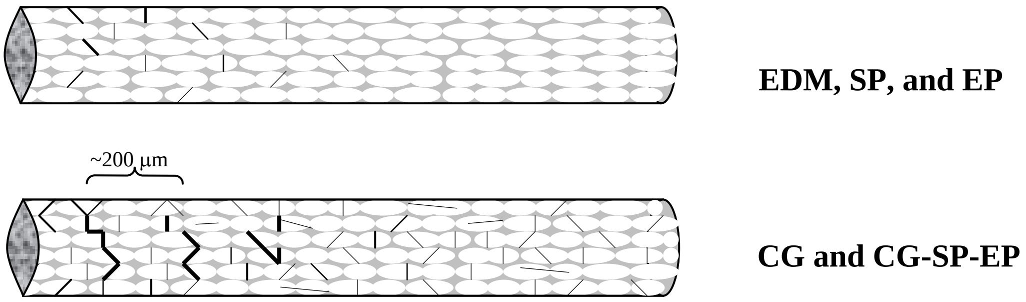

Figure 26: Drop Tower Specimen Tensile Surface Representations with Fracture Surface at Left (Tensile Stress Orientation ←→)

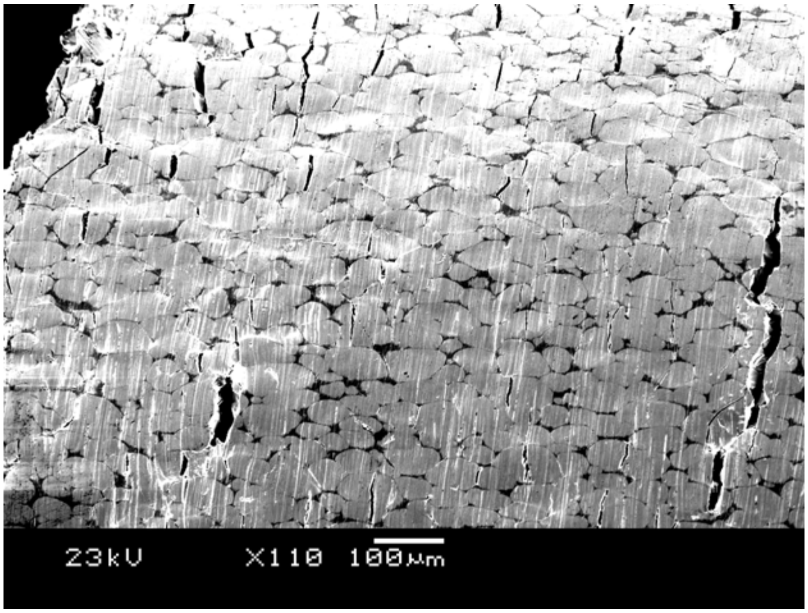

(a) CG

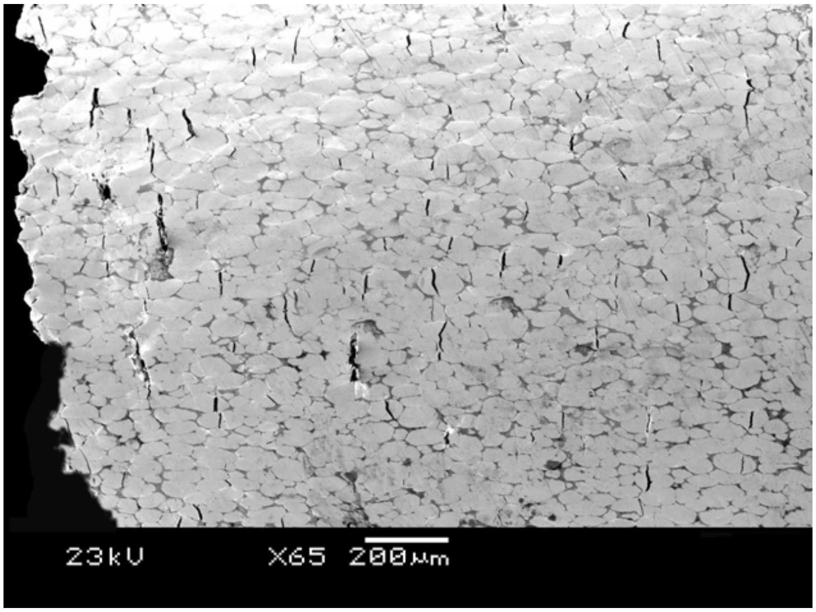

(b) CG-SP-EP

Figure 27: Room Temperature WNiFe Drop Tower Tensile Surface Damage Accumulation Adjacent to Fracture at Left (Tensile Stress Orientation ←→)

5.3.2 Normal Cross-Sections

A study of specimen cross-sections normal to the tensile plane revealed a more remarkable trend, one that accounted for the apparent lessening of surface damage with surface finish improvement. In the tested EDM specimen, extensive cracks in the form of W cleavage are apparent, but only at the tensile surface, as shown in Fig. 28(a). The regularity observed during tensile surface examination was again noted here, with surface fractures separated by about 200 μm. In contrast, surface finish improvement resulted in the development of internal fracture nucleation, so much so that in the case of the CG-SP-EP specimen there is significantly more internal damage nucleation than there is on the surface, as shown in Fig. 28(b). This internal damage is fairly evenly distributed between W grain cleavage and W-W separation. The same holds true for even the least aggressive surface treatment, SP, as shown in Fig. 29(a), where removal of an average of only 5 μm from the rod radius (from data in Table 6) caused the onset of internally nucleated fractures. In the EP specimens in Fig. 29(b), surface and internal damage appear evenly distributed. In the CG specimen in Fig. 29(c), surface damage appears more extensive than interior damage.

These results mirror findings in earlier work, where the absence of surface flaws in pure polycrystalline W resulted in both surface and internally nucleated failure initiation [90]. They also suggest a close competition between W grain cleavage and contiguous W grain separation as modes competing to initiate fracture. Because they are the weakest of the four failure modes, they can be considered the fracture initiation mechanisms, whereas W-matrix separation and matrix failure are primarily fracture propagation mechanisms.

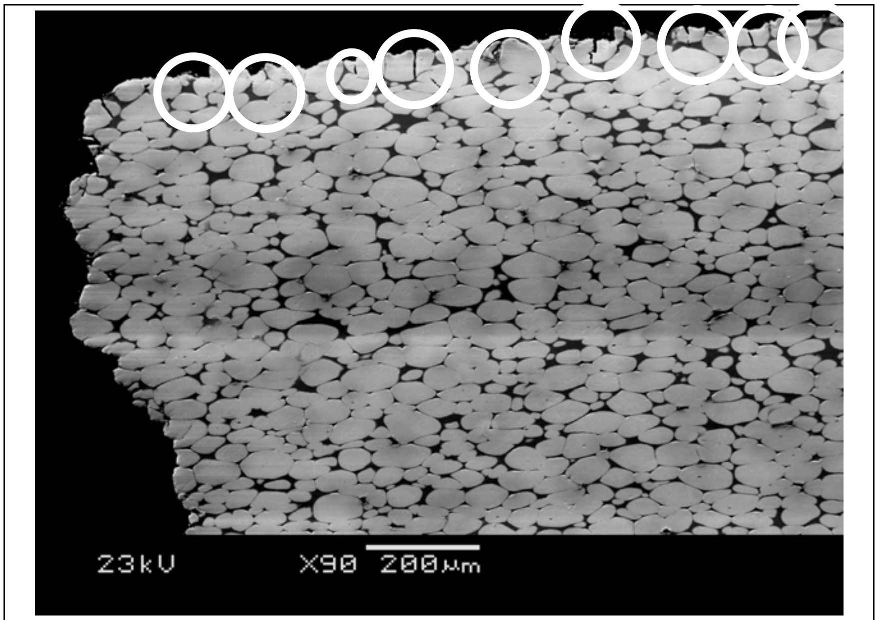

(a) EDM Specimen with Surface Damage Nucleation Only

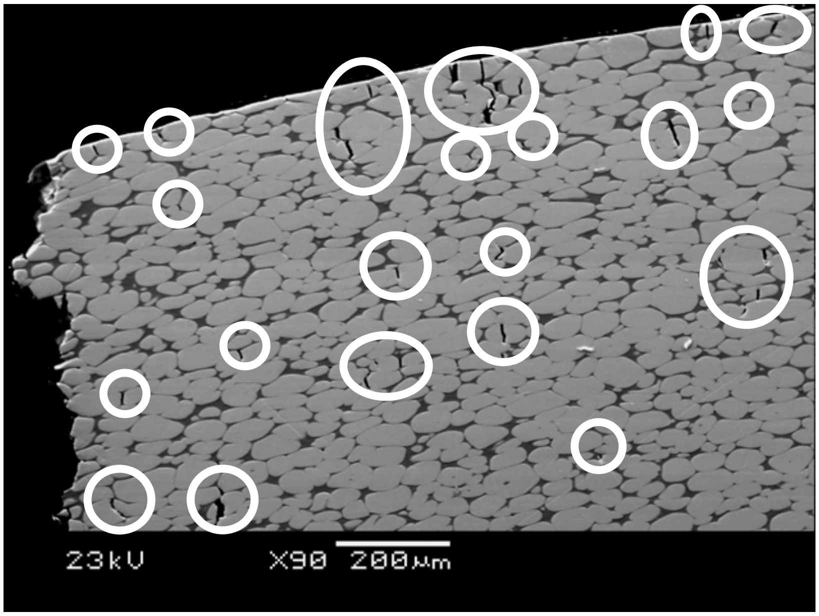

(b) CG-SP-EP Specimen with More Significant Internal than Surface Damage Nucleation

Figure 28: WNiFe Drop Tower Specimen Normal Cross-Sections of Tensile (at Top) and Fracture (at Left) Surfaces (Tensile Stress Orientation ←→)

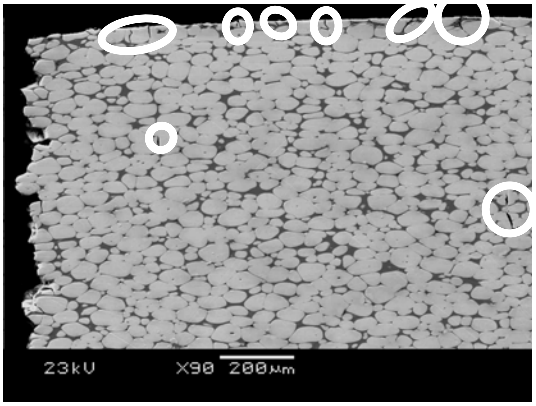

(a) SP

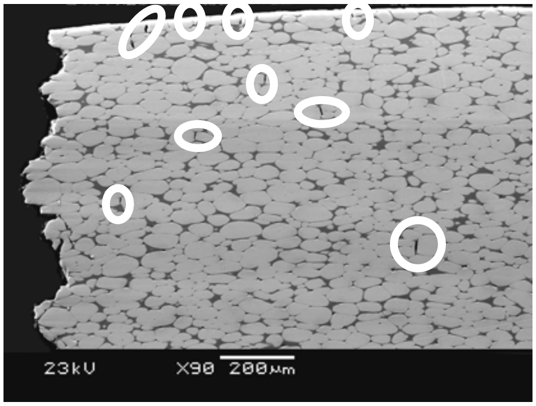

(b) EP

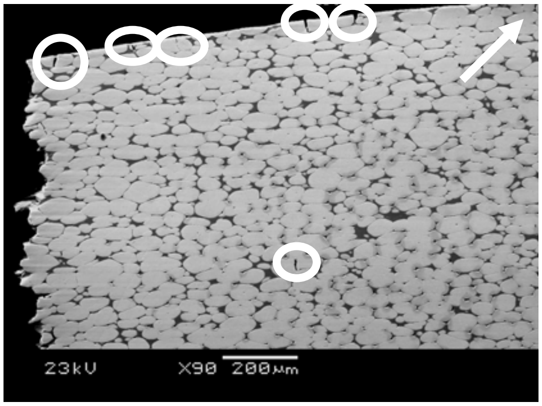

(c) CG

Figure 29: WNiFe Drop Tower Specimen Normal Cross-Sections of Tensile (at Top) and Fracture (at Left) Surfaces (Tensile Stress Orientation ←→)

The results from CG-SP-EP specimens suggest that the absence of preexisting surface flaws serving as fracture initiation sites delays the onset of fracture. This leads to internal fracture nucleation and greater strain to failure, explaining the greater specific fracture energy of surface-improved rods. This is more readily illustrated in a cross-section of a CG-SP-EP WNiFe specimen that did not break, as shown in Fig. 30 (inverted so that the tensile surface is at the top), which illustrates the dominance of internally nucleated fractures.

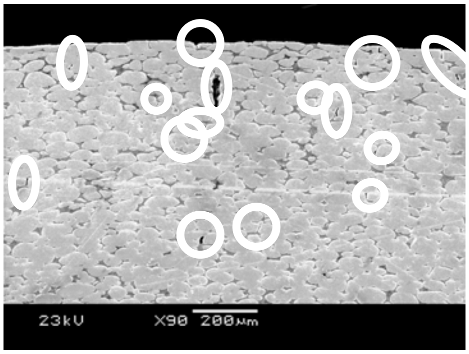

(a) Tensile Surface

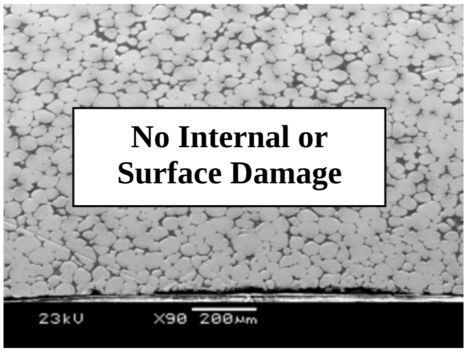

(b) Compressive Surface

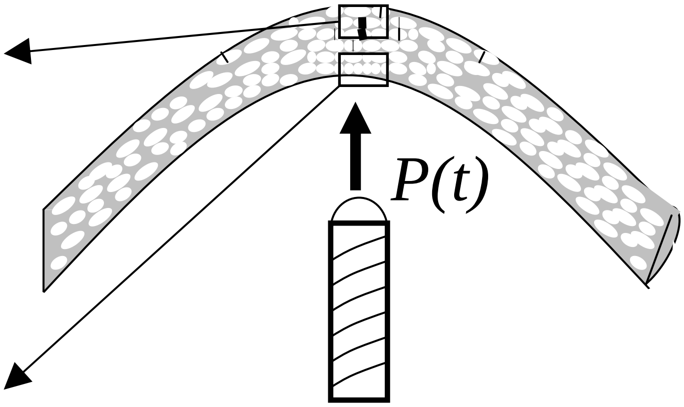

(c) Specimen Sketch

Figure 30: Micrographs and Sketch of Internal Fracture Nucleation in Unbroken CG-SP-EP WNiFe Drop Tower Specimen

The largest nucleated fracture shown in Fig. 30(a), CG-SP-EP WNiFe, is an internal, multi-grain W cleavage, shown at greater magnification below in Fig. 31. A developing fracture adjacent to this feature and consisting of the link-up of individual damage features is apparent, among which are incompletely cleaved W grains. Additionally, and as in the case of the broken specimen of the same surface treatment shown in Fig. 28(b), there is a fairly even distribution of internal W-W separations and unlinked W cleavages; there are also a limited number of surface W grain cleavages beyond the view of the micrograph, as indicated in the sketch in Fig. 30(c).

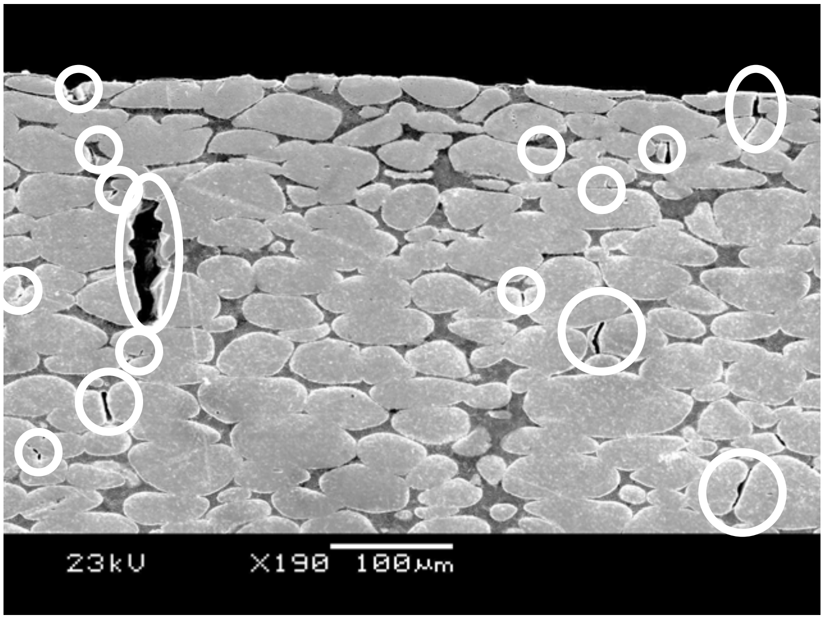

Figure 31: Primarily Internal Fracture Nucleation Detail in Unbroken WNiFe CG-SP-EP Drop Tower Specimen

Also of note from Fig. 30(b) is the absence of fracture features at the compressive surface and grain compression that has resulted in the originally ellipsoidal grains (due to swaging) becoming spheroidal.

Because of these apparent microstructural changes, ImageJ was used to analyze the micrographs of longitudinal sections adjacent to the compressive and tensile surfaces shown in Figs. 30(a) and 30(b). The results, plus or minus one standard deviation, were compared to those from the original WNiFe bar stock analysis, all of which are shown in Table 13.

Table 13: Comparison of WNiFe Original Bar Stock and Drop Tower Specimen Microstructural Analysis

		Equivalent Circular Diameter (μm)	**W Area Fraction (%)**	**Aspect Ratio**
Original Longitudinal Sections	**Near Surface**	58 ± 26	82	2.00 ± 0.56
	Mid Radius	55 ± 23	78	2.27 ± 0.76
	Near Center	59 ± 25	82	1.97 ± 0.58
CG-SP-EP Drop Tower Sections	**Tensile Surface**	55 ± 25	72	2.29 ± 0.80
	Compressive Surface	55 ± 27	79	1.63 ± 0.41

The unbroken CG-SP-EP drop tower specimen equivalent circular grain diameters match well with those from the original analysis, particularly the “mid radius” value. As the specimen being considered originated from the “middle ring” near the center of the bar radius, this is expected. However, the tensile W area fraction is lower, likely due to the presence of cleaved W grains. The aspect ratio of grains on the compressive surface has been significantly altered by compressive plastic deformation.

The reduction in W grain aspect ratio on the compressive surface of the sample indicates a local engineering strain, *e*:

$$e = \frac{(l - l_o)}{l_o} \tag{5.13}$$

where l_o = original length

l = subsequent length

and $l-l_o$ = elongation or compression

An estimate for the compressive strain can be calculated with Eqn. 5.13 using the change in the average W grain long axis length from the original bar stock mid-radius, 81 μm, to that of the micrograph in Fig. 29(b), 68 μm. Accordingly:

$$e = \frac{(68\ \mu m - 81\ \mu m)}{81\ \mu m}$$

= -0.160, or 16.0% compressive strain

In terms of true strain, ε:

$$\varepsilon = \ln\left(\frac{l}{l_o}\right) = \ln\left(\frac{68\ \mu m}{81\ \mu m}\right) \tag{5.14}$$

= -0.175, or 17.5% compressive strain

These values of strain match well with the value of 17% bending (engineering) strain determined from the average bend angle for CG-SP-EP specimens and reflected in Table 11.

5.3.3 Fracture Surfaces

SEM fracture surface images from WNiFe specimens of all surface finishes indicate the predominant failure mode to be W grain cleavage. An example fractograph is shown in Fig. 32. This result agrees well with findings in other WHA dynamic failure work [30-39]. The other failure modes (contiguous W grain separation, W grain-matrix separation, and matrix failure) are also present, but are fewer in number. Cleaved W grains appear flat or faceted and have either “river line” striations radiating from an apex or predominantly parallel steps. Both the flat and faceted (ridged) natures are functions of WHA’s preferred [110] fiber texture upon swaging [72,73] and the resolved tensile stresses within BCC crystals. For BCC crystals subjected to tensile loading parallel to [011], two planes of the primary {100} cleavage system, the (001) and (010), have equivalent resolved normal tensile stresses which are less than that on the (011) plane. Consequently, cleavage may occur either on orthogonal {100} planes resulting in a ridged appearance, or on a (011) plane, producing a flat surface [77]. Additionally, cleavage should be expected to be the predominant failure mode in a WHA microstructure with elongated grains aligned with the tensile axis, as it would be difficult for fractures on planes normal to the tensile axis to avoid passing through W grains; this has been shown to be the case for pure, polycrystalline W [81].

Contiguous W-W grain separations are generally smaller and appear absolutely flat with no extraneous features; these are sometimes obscured by matrix material dimpled through cavitation due to void nucleation. Both W cleavages and W-W separations are also sometime visible penetrating into the plane of the micrograph. The white, fibrous features surrounding W grains represent matrix failure, which is caused by matrix ductility leading to plastic deformation and work hardening prior to failure. W grain - matrix separations appear as dark voids between W grains and the matrix in Fig. 32.

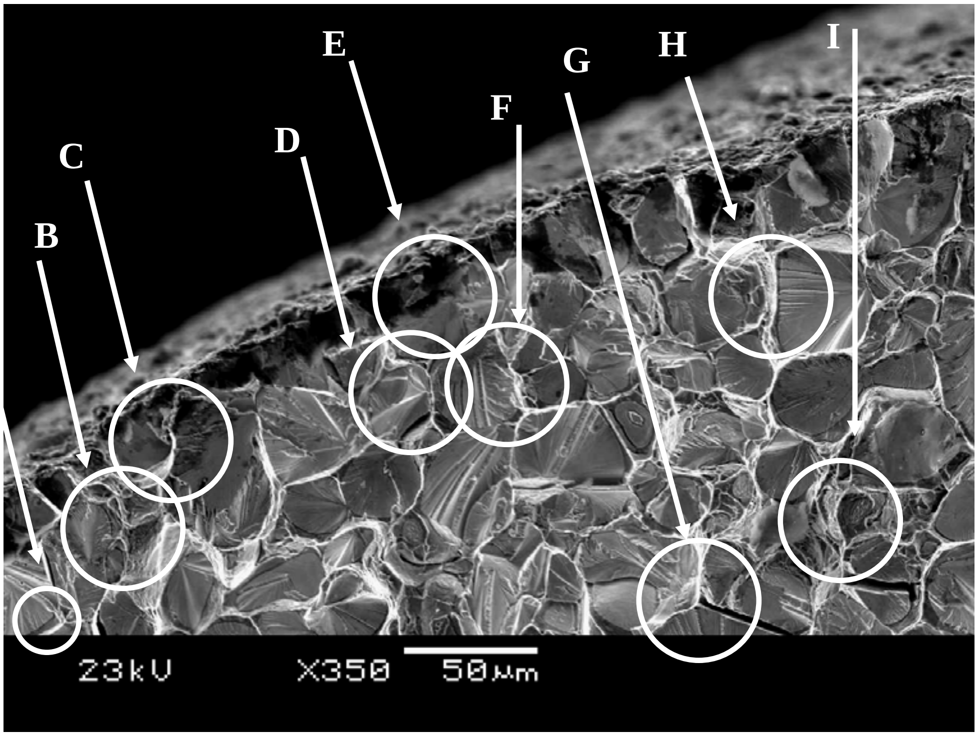

Figure 32: Fracture Surface of EDM WNiFe Drop Tower Specimen Near Fracture Initiation (Tensile Surface at Top) -- (A) W Grain-Matrix Separation; (B) Matrix Pull Out; (C) Flat W Grain Cleavage; (D) Cleavage Steps; (E) Faceted W Grain Cleavage; (F) Contiguous W-W Grain Separation; (G) W Grain Cleavage Penetrating Plane of Micrograph; (H) W Grain Cleavage with River Markings: (I) Matrix Void Nucleation on W-W Contiguous Grain Separation

Because the EDM WNiFe specimens have been shown to fail due to surface-initiated fracture resulting from preexisting W grain microcracks, this information can be used to guide a closer investigation of the fracture surfaces. In so doing, it is possible to attempt to locate discrete fracture initiation sites. Observations of fracture surfaces indicate fracture regions radiating inward from the exposed surface. Abrupt changes of fracture morphology, as shown in Fig. 33, indicate stages of initial pre-cracking followed by fracture leading to final failure of the specimen.

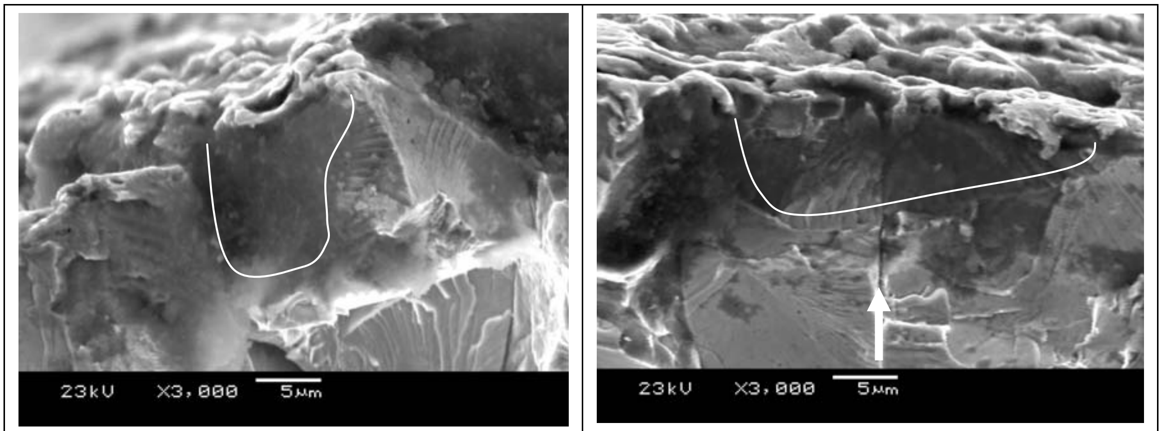

(a) Partial W Grain Pre-crack Indicated by Flat Cleavage Region Surrounded by Striations

(b) Partial W Grain Pre-crack Indicated by Stepped Cleavage Region and Crack Penetrating into Plane of Micrograph

Figure 33: Possible Fracture Initiation Pre-Crack Sites at Tensile Surface of EDM'd WNiFe Drop Tower Specimen

It is also possible to develop an understanding of the overall fracture propagation direction by studying and mapping local directional indicators. Such a technique has been employed for W single crystals [77] and for the analysis of stress corrosion cracking in uni-directional glass-fiber reinforced polyester resin composite [177], but has not yet been pursued in the analysis of WHA fracture at any strain rate. River lines and cleavage steps on the surfaces of fractured W grains are known to run primarily parallel to the direction of local fracture growth [77], though exceptions have been noted [78-80,153,155]. Assuming the former to generally hold true, each feature can be assigned a vector representing the local fracture propagation direction. Taking the technique a (new) step further, these local, or micro directional indicators can be treated as unit vectors, then summed and averaged to determine an overall, or macro, crack front propagation direction. These vectors can also be interpreted, much the same as "connecting the dots," to develop an understanding of the manner in which WHA fractures actually progress, as is demonstrated in Fig. 34. Initial work led to the use of micrographs taken at 350x to ensure a statistically reliable number of grains to evaluate (greater than thirty) while maintaining sufficient detail so that grain surface markings could be interpreted.

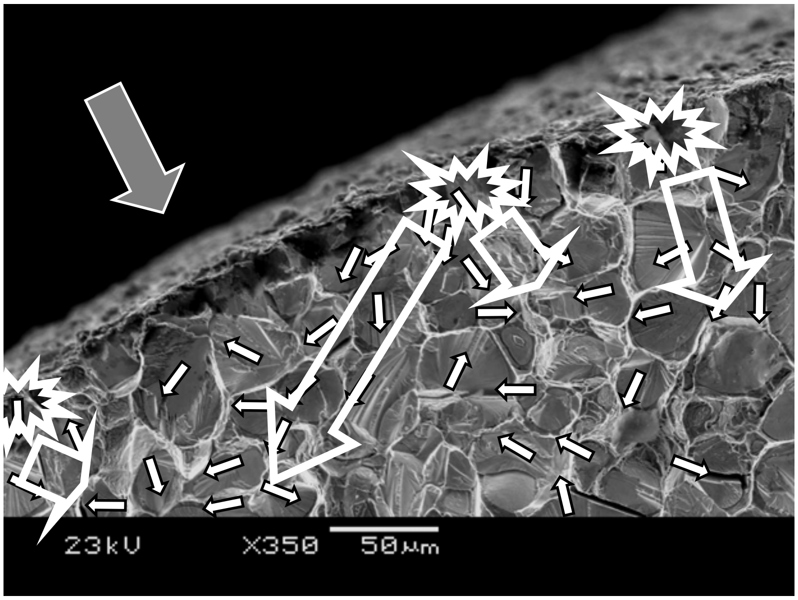

Figure 34: Tensile Fracture Surface of EDM WNiFe Drop Tower Specimen Near Fracture Initiation

Fig. 34 Legend:

Apparent nucleation site as indicated by local visual evidence = ✸

Directional unit vector indicating cleavage of individual W grains = ⇨

Local microstructural fracture propagation direction over several grains = ⇨

Average of W grain unit vector directional indicators over entire micrograph = ⇨

Immediately apparent and interesting to note is the frequency with which the local fracture propagation directions *do not* match the global direction, due to the activation of fracture nuclei ahead of an advancing crack front and their subsequent growth toward the approaching front.

To increase the number of features available for evaluation and, thus, the statistical reliability of the technique, macro-directional analysis indicating the overall direction of crack-front propagation can also be performed over composite images, as shown in Fig. 35.

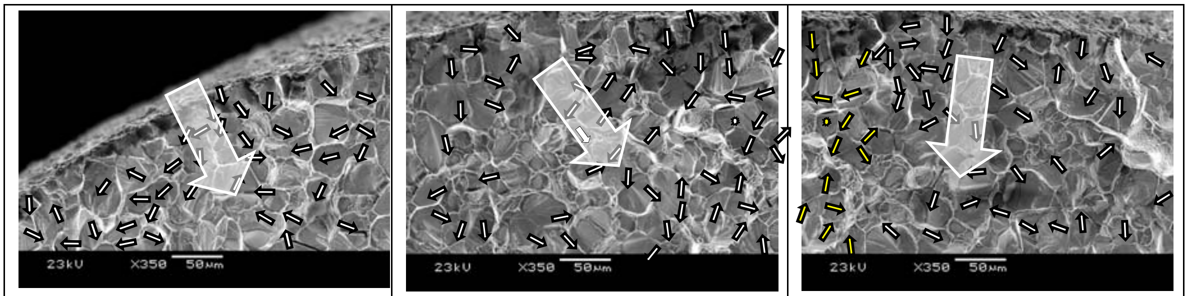

(a) Surface Left (b) Surface Center (c) Surface Right

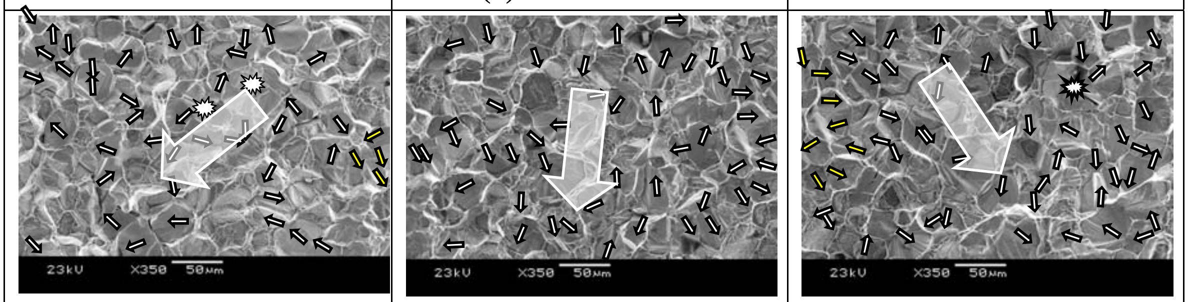

(d) Subsurface Left (e) Subsurface Center (f) Subsurface Right

Figure 35: Composite Tensile Fracture Surface Images of an EDM WNiFe Room Temperature Drop Tower Specimen with Micro and Macro Directional Indicators

Here, the global fracture propagation direction determined from more than 250 local W grain cleavage indicators matches well with what is inferred by the individual frames. For both the single and composite images, the "determined" direction of crack front propagation reasonably matches that which is known to be true from the loading conditions and failure of the rod, initiating near the tensile surface-center at the top of the composite image and progressing toward the compressive surface at the bottom of the image.

The same technique was applied to micrographs from the EDM WNiFe fracture surface midsection and near the compressive surface in Fig. 36, and for room temperature CG-SP-EP WNiFe drop tower micrographs in Fig. 37.

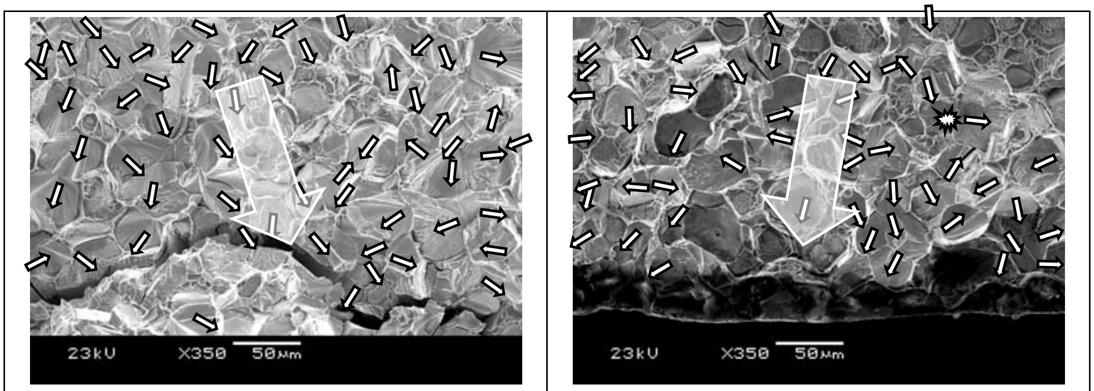

(a) Mid-Section Center

(b) Compressive Surface Center

Figure 36: Fracture Surface Image of an EDM WNiFe Room Temperature Drop Tower Specimen with Micro and Macro Directional Indicators

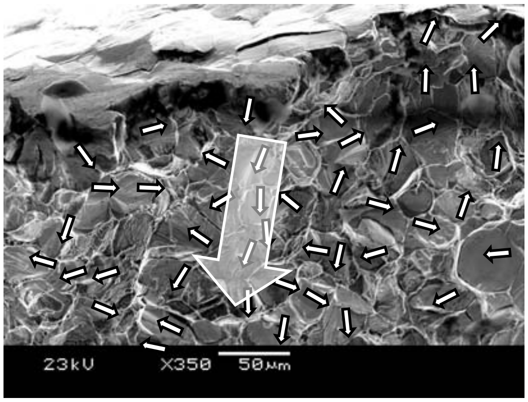

(a) Tensile Surface Center

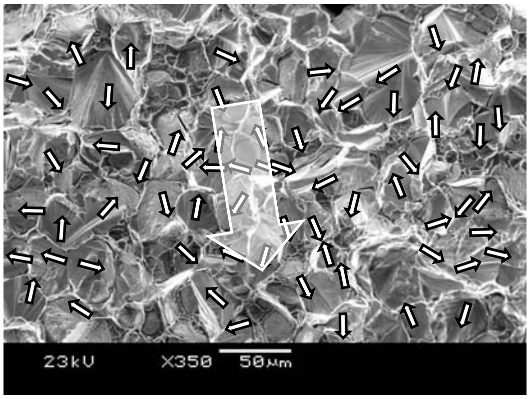

(b) Mid-Section Center

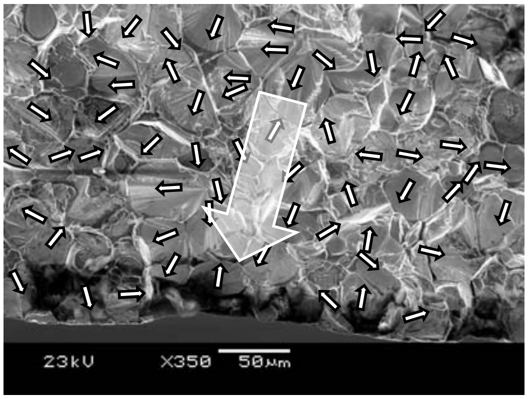

(c) Compressive Surface Center

Figure 37: Fracture Surface Images of a CG-SP-EP WNiFe Room Temperature Drop Tower Specimen with Micro and Macro Directional Indicators

Among the numerous fracture surfaces observed, a number of particularly noteworthy local features were noted. These include: multiple surface cleavage initiation sites on a single W grain, sometimes with complementary directional indicators and sometimes opposing; radial cleavage indicators on a individual grains, usually associated with what appeared to be a bisected grain pore; and river lines or cleavage steps continuous over more than one W grain, suggesting coplanar grains matched in their crystallographic orientation. W grain porosity did not appear to be a dominant factor in WHA fracture, but was noted as a possible internal nucleation source.

Overall, WHA fracture surfaces in both individual and composite images reveal that the surface-initiation of fracture is very much a local event occurring at discrete locations of the greatest weakness. Fractures propagate into the microstructure along competing axes that follow paths of favorably oriented local nucleation sites, sometimes bypassing more fracture resistant regions. This can be seen in Fig. 34. Within a depth of approximately 400 μm into the surface of the rod, these axes converge. Crack propagation in the body of rods occurs in a similar fashion. Fracture axes advance by lengthening, broadening, branching, and coalescing, as well as linking through bypassed areas. Crack “fronts” are formed when these axes converge.

5.4 EVALUATION OF DYNAMIC FRACTURE TOUGHNESS, K_{ID}

5.4.1 Approach

The determination of the dynamic fracture toughness, K_{ID}, of WHA is not a specific objective of this work. Even so, inferences can be made about the K_{ID}, of the alloys considered using the average initial flaw size of a given material-surface finish and the bending-induced strain prior to fracture resulting from drop tower testing. With these parameters, and the results of the elastic-plastic analysis in Section 5.2.4 indicating that WNiFe sample failure occurs in the plastic regime, K_{ID} can be estimated. If the material flow (true) stress relationship is known, K_{ID} can calculated from Eq. 2.2:

$$K_{ID} = \sigma_f C\sqrt{\pi a} \tag{5.15}$$

where σ_f = failure stress

C = elastic geometric constant, or 0.66 to 1.12 for a semi-elliptical surface crack in a shaft under bending, depending upon the aspect ratio assumed [128]

a = measured average initial flaw size, shown in Table 8

Assuming similar flow behaviors in tension and compression, the true stress – true strain, and thus, flow stress - strain, relationship can be determined from compression testing of WHA rod specimens. Once this relationship is known, the stress resulting from drop tower-induced bending strain can be approximated and used with the average initial flaw sizes to determine K_{ID}.

Compression testing was conducted on an Instron 1125™ with a 1.27 mm (0.05 in)/min extension rate and 10 Hz data capture rate using CG samples approximately 1.5 times as long their diameter to avoid buckling, resulting in a strain rate of ~ 0.3/s. Specimen surfaces in contact with the compression plattens were well lubricated with a high-pressure lubricant (Dow Corning™ G-n Metal Assembly Paste). Two specimens of each alloy, WNiCo and WNiFe, were tested.

5.4.2 K_{ID} Determination

WHA compression data recorded were load versus displacement. These data were converted to true stress, σ_T, versus true strain, ε_T, assuming constant volume and no barreling. The examination of test specimens indicated that any barreling at the strains of interest was slight. Using the documented value of elastic modulus, *E*, for WNiFe from Table 2 (362 GPa) and the linear portion of the compression test data, the test apparatus compliance was calculated. Stress-strain data were then compensated for the apparatus compliance, yielding the σ_T versus ε_T relationships shown in Fig. 38.

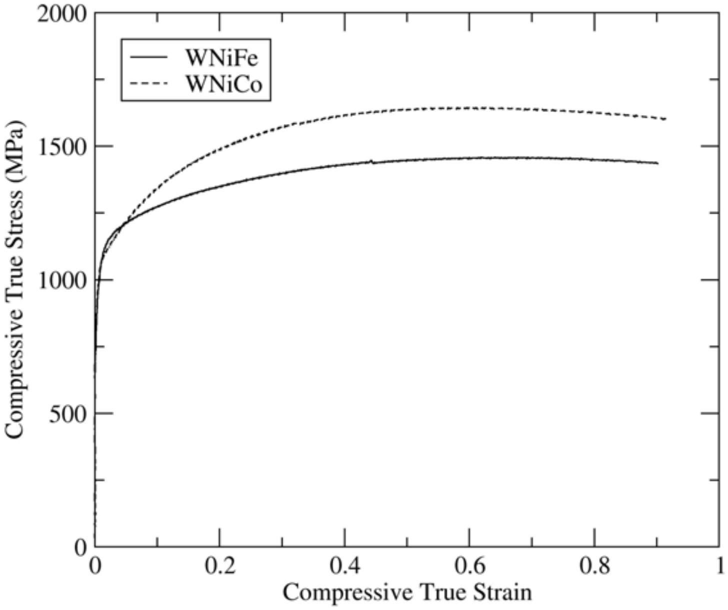

Figure 38: WHA Compressive True Stress vs. Compressive True Strain

The results between specimens of the same alloy were consistent, and the greater strength of WNiCo is apparent at large strains. These data match well with published data for similar alloys and strain rates [59,178].

Bending strains were determined from the bend-angles sustained prior to fracture, shown in Table 11; because micrographs from drop-tower specimen tensile surfaces indicated the presence of cracks, a micrographic evaluation of tensile strain sustained by individual W grains was not practical. It was assumed that true strain at specimen tensile surfaces was equal in magnitude and opposite in sign to that at the compressive surfaces, shown in Section 5.3.2 to be accurately represented by the (engineering) strain determined from the bend angles. Thus, for an EDM WNiFe specimen:

From Table 8, $a = 17.9 \pm 8.6$ μm
From published data [129], $C_{avg} \cong 0.88$
From Table 11, $e = 0.074$
From Fig. 37, $\sigma_f \cong 1200$ MPa

And from Eq. 5.15, $K_{ID} \cong 7.92 \pm 1.97\ MPa\sqrt{m}$

Because of the limited number of drop tower tests conducted with the WNiCo alloy, a K_{ID} analysis was conducted only for the WNiFe alloy.

This calculated range of values for K_{ID} is lower than published values for alloys and strain (or stress intensity) rates similar to those considered in this work which range from approximately 30 to $90 \pm 13\ MPa\sqrt{m}$, depending upon stress intensity rate, microstructure and the orientation tested; swaged WHA has been shown to have rate and directionally dependent K_{ID} values [111]. Published (room temperature) K_{IC} values for pure, single-crystal W provide a better match, ranging from 6.2 ± 1.7 to 20.2 ± 5.5 $MPa\sqrt{m}$, depending upon the crack system considered [78-81].

There are a number of probable causes for the calculated K_{ID} value being so low. First, the initial EDM-induced W grain microcracks are on a microstructural order and much smaller than precracks typically used in K_{ID} determination, rather than many times that size as is typical. Also, these are subcritical cracks, known to be smaller than a critical crack size and less than that required to ensure a plane-strain loading condition. Additionally, it has been shown in this work that damage accumulation leads to failure, rather than growth of a single edge-crack, resulting in a much larger overall fracture length and plastic deformation. Finally, geometric factors for complex geometries such as may be present under these failure conditions may be far different and are likely larger than that used in this calculation.

Chapter 6: High Strain Rate Ballistic Testing

6.1 TEST DESCRIPTION

Ballistic impact testing was conducted at the University of Texas Institute for Advanced Technology's (IAT) two-stage, light-gas gun laboratory in a "reverse ballistic" format. Reverse ballistic testing offers a convenient alternative to conventional ballistic testing when unusual geometries or interactions are involved [179]. With the assumption that the dynamics of penetrator-target interaction are the same regardless of which is moving relative to the other, reverse ballistic testing allows control of yaw angle and interaction geometry, parameters that are very difficult to control in conventional ballistic testing. This is done by positioning the penetrator down-range as a target, and launching the true "target" as a projectile.

Initial experimental goals were to refine instrumentation and procedure for future reverse ballistic testing, to develop a reliable means of recovering rod fragments for micrographic analysis, and to evaluate the test method as a potential screening test for other WHA's. Once the technique was proven viable, fixturing was refined to simplify the process of mounting a rod at the desired attitude.

6.1.1 Two-Stage Gas Gun Principles of Operation

Two-stage gas guns operate much like conventional guns in that expanding gas accelerates a projectile. The distinguishing feature of two-stage gas guns is that instead of accelerating projectiles directly, propellant gases are used to drive a piston, which in turn compresses a light gas, usually helium or hydrogen. A diaphragm or rupture valve initially containing the light gas ruptures at the design pressure, allowing the light gas to accelerate the projectile as shown in Fig. 39. Higher velocities are attainable with light-gas guns than with conventional guns because of the ease with which a light gas can be accelerated.

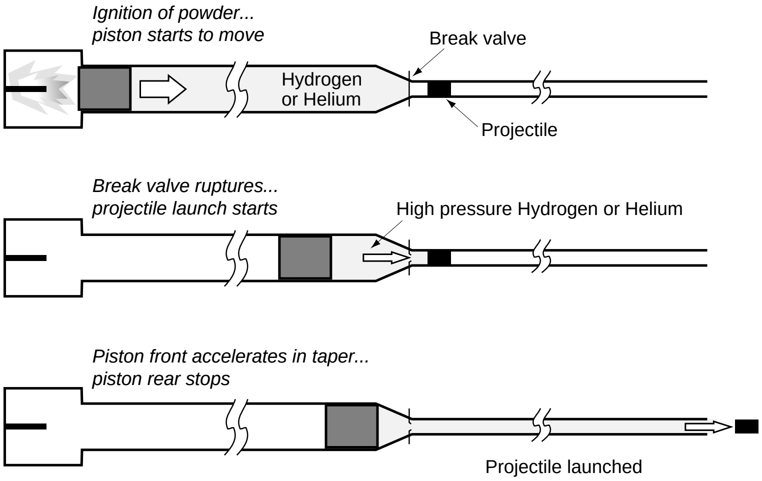

Figure 39: Two-Stage Gas Gun Principles of Operation (adapted from [180])

6.1.2 Reverse Ballistic Experimental Setup

Fixturing was developed such that rods would be subjected to yawed impact by rolled homogeneous armor (RHA, nominally AISI 4340 steel) “targets,” to impart transverse loading leading to rod failure. The interaction geometry is shown in Fig. 40.

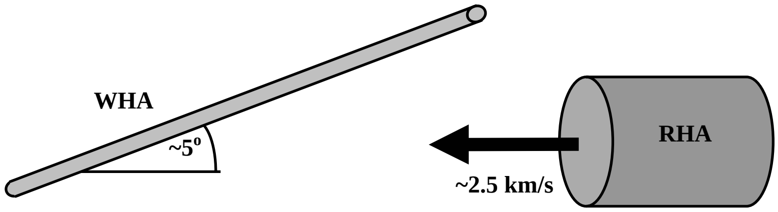

Figure 40: Reverse Ballistic Target Interaction Geometry (not to scale)

6.1.2.1 Rods and Projectiles

Full-length (108 mm) rods were used in reverse ballistic testing, as opposed to the half-length (54 mm) rods used in drop tower testing. Other rod particulars have already been addressed. The launch packages consisted of RHA cylinders that were press-fit into Lexan™ sleeves, as shown in Fig. 41. Initially, each launch package had an approximate mass of 420 grams with outer dimensions of 38.1 millimeters in diameter and 69.85 millimeters in length (including the Lexan™). After preliminary tests discussed further in Section 6.2.1, the design was modified to include a two-piece detachable sleeve to ensure that initial contact between a rod and the sleeve was avoided. Slightly increasing the sleeve thickness and reducing the core diameter as a result dropped the mass to 360 grams while maintaining the exterior dimensions. Launch package (target) velocity was determined by powder charge mass, which was initially chosen to produce velocities of approximately 2.3 km/sec. However, an early shot that produced more remarkable results at approximately 2.4 km/s led to a decision to conduct subsequent shots at this higher velocity, providing strain rates of approximately 10^5/s.

Figure 41: RHA Launch Package

6.1.2.2 Fixturing

A mounting fixture was designed to provide accurate rod position and orientation adjustment, enabling a yaw angle of approximately five degrees to be set for each experiment with a machinist's height gage and a laser boresight device [181]. The fixture is shown in Fig. 42. A new technique was developed to catch rod fragments generated during rod–target interaction by erecting a wood-frame and particleboard assembly over the rod-mounting fixture, as shown in Fig. 43. The particleboard served to catch rod fragments after impact events. Rod fragments were removed from the particleboard by hand and sifted from containment tank debris. For the non-ferromagnetic WNiCo alloy, a large magnet was used to speed this process by magnetic separation of steel projectile remnants; this had to be done visually for the WNiFe alloy, which is ferromagnetic. The rods were reconstructed from recovered fragments using flash X-rays photographs taken during the experiments and by visually matching fracture surfaces.

Figure 42: Rod Mounting Fixture

Figure 43: Down-Bore View of Particleboard Assembly

As the experimental procedure was being developed during initial experiments, each shot required approximately two days of setup and an equal amount of time for recovery and preparation of the next shot. This does not include the time required to reassemble and photograph recovered rods, or the lead time required for rod and launch package fabrication and rod surface treatment. As the process became more refined, the turnaround time was reduced to approximately one day each for setup and recovery.

6.1.2.3 Flash X-Ray Photographs

Flash X-ray photographs were used to document each experiment. Horizontal and vertical plane “static,” or *a priori* flash X-ray photographs, were used to confirm the experimental setup, specifically rod position, pitch, and yaw, as shown in Fig. 44. Dynamic flash X-ray photographs, triggered by the launch package contacting a crush pin set in the projectile’s shot line, were used to capture rod-target interaction. Post-experiment X-rays photographs of the particleboard were used to locate embedded rod fragments.

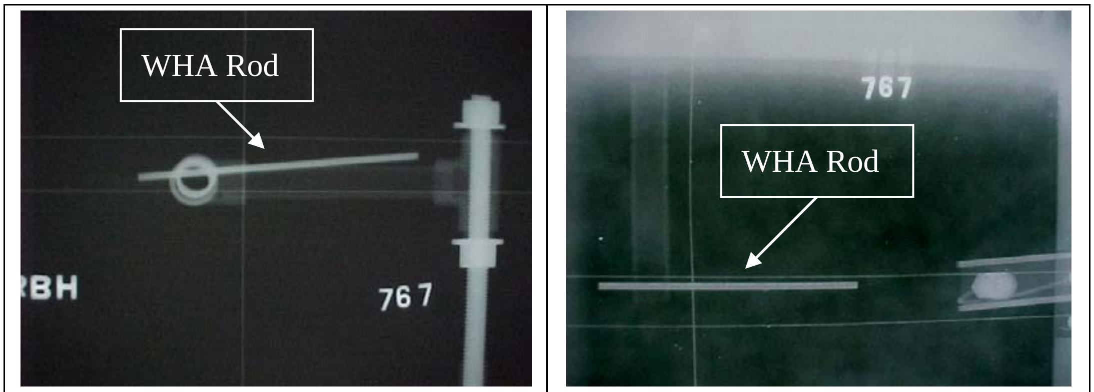

(a) Horizontal Plane

(a) Vertical Plane

Figure 44: Shot #767 – EDM WNiFe Static Flash X-Ray Photographs
(← Projectile Travel)

Also available during initial reverse ballistic experimentation was the capability to convert the “negative” flash X-ray photographs to “positive” contact print images, as well as overlaying static and dynamic images to create “composite” images giving the effect of a double exposure. Unfortunately, this capability was lost prior to the completion of experiments, so only a limited number of flash X-ray photographs were actually converted to contact prints or composite images.

6.1.3 Post Experimental Analysis

6.1.3.1 SEM Investigation of Recovered Samples

Metallographic sample preparation and investigation of rod fragment normal cross sections and fracture surfaces were conducted as previously discussed for drop tower specimens. However, the recovery of rod fragments was complicated by the embedding of wood from the particleboard in recovered rod fragment surfaces. Various ultrasonic cleaning solutions were tried to remove embedded wood fragments, including acetone, mineral spirits, and a commercially available NaOH solution, which was found to attack both the W grains and the matrix upon extended exposure. None was found to be entirely successful at removing all wood particles without damaging the exposed sample surface, as in the case of the NaOH solution. Ultimately, it was decided to disregard the wood particles on specimens being mounted and metallographically prepared and to avoid using specimens heavily embedded with particles for fracture surface analysis.

6.1.3.2 CTH Modeling

One of the overarching motivations for this work was the lack of a useful fracture criterion in numerical simulations, such as those using the CTH code. Even so, such models are beneficial tools in predicting high-rate loading conditions and overall dynamic behavior. Without numerical modeling, the conditions leading to rod failure during reverse ballistic testing would not be known.

Accordingly, CTH hydrodynamic simulations were conducted in support of this work to model the interactions created during reverse ballistic testing. This was accomplished by staff and faculty of the University of Texas Applied Computational Engineering & Sciences (ACES) facility. The modeling included baseline interactions, as well as variations of parameters revealed through the experimentation in this effort as critical to understanding high-rate WHA failure behavior and the development of dynamic WHA failure models.

6.2 EXPERIMENTAL RESULTS

6.2.1 Reverse Ballistic Physical Results

A series of twenty-three reverse ballistic impact experiments subjecting WHA rods to transverse loading was conducted over a period of ten months [182]. A data table reflecting these experiments is shown in the Appendix. As was noted during drop tower testing, it was clear early on in this testing that the two WHA's considered behaved quite differently under the conditions of reverse-ballistic impact. This lends support to the use of dynamic 3-point bend testing as a suitable, less resource-intensive alternative to reverse ballistic testing as a transverse failure-resistance screening test.

The flash X-ray photograph in Fig. 45 of shot #717, conducted at 2.30 km/s with an EDM WNiFe rod, reflects a considerably distorted, segmenting rod with multiple fractures. These fractures are initiated under tensile loading, typically on the side of the rod opposite that interacting with the target. This surface is denoted the "tensile" surface because of the expected bending shown in Fig. 45. However, the surface may not actual be in tension during the entire interaction event. Fractures deflect gradually toward the rod tail, the direction of sliding load motion, developing a characteristic "lazy S" shape. The one exception to this is shown in Fig. 45 fracture #4, caused by initial rod-launch package contact in the vicinity of fracture #3, which forced the nose of the rod to whip clockwise. This generated a "backwards" fracture running from bottom to top, opposite from the fractures caused by the rod bending in response to contact with the launch package, such as in fractures 1-3 in Fig. 45. The rod segments have a fairly uniform size, with an average mass of 1.0 grams as determined from recovered fragments.

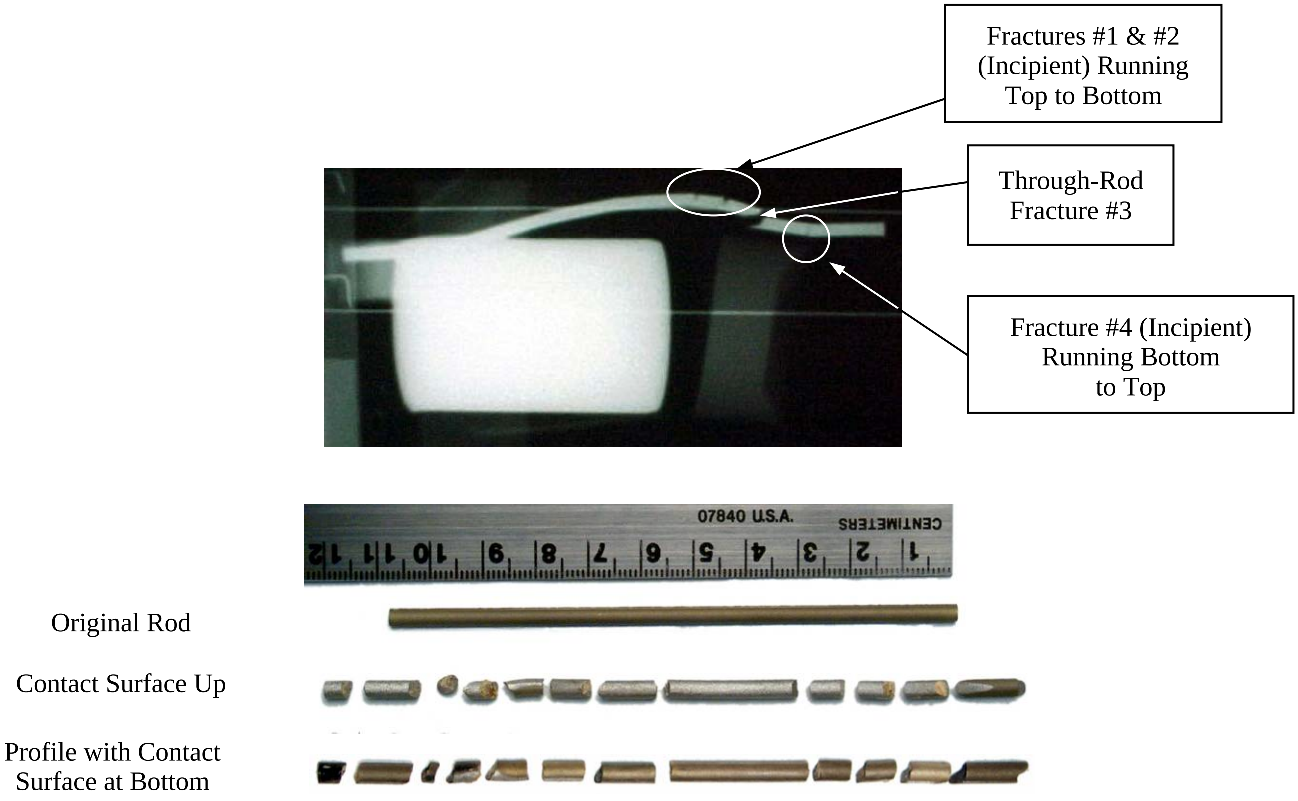

Figure 45: Shot #717 - EDM WNiFe Flash X-Ray Photograph and Recovered Rod Segments (← Projectile Travel)

That the fracture surfaces are not flat is indicative of multi-mode loading leading to rod failure. This has been well documented for pure, swaged, polycrystalline W, where increasing the mode II loading component in a mixed mode I/mode II loading situation caused a significant increase in the crack deflection angle [81].

After initial shots and preliminary CTH modeling, it was thought that the Lexan™ sleeve of the projectiles might be making initial contact with the rods rather than the RHA. A subsequent shot, shown in Fig. 46, was conducted at 2.37 km/s with a primarily Lexan™ launch package against EDM WNiFe specifically to determine if Lexan™-only contact would be sufficient to cause rod fracture. The launch package, shown in Figs. 46(a) and 46(b), consisted of a 38.1 mm diameter, 180 mm long Lexan™

slug with a steel (all-thread) shank embedded to help maintain in-flight stability. This projectile had a mass of 404 g.

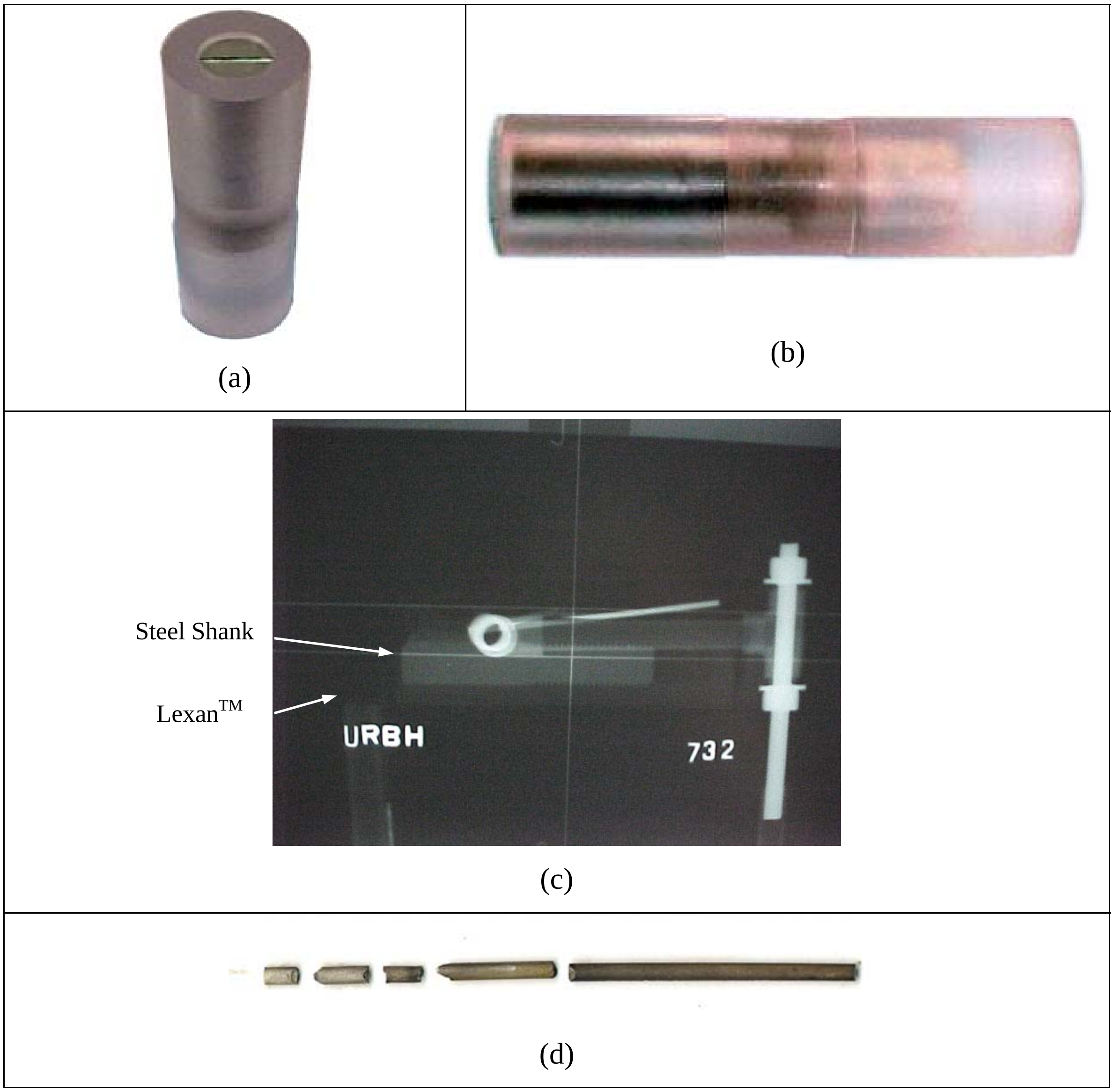

Figure 46: Shot #732 - EDM WNiFe: (a) & (b) Launch Package; (c) Flash X-Ray Photograph (← Projectile Travel); (d) Recovered Rod Segments

Even though rod fracture is not apparent in Fig. 46(c), the recovered rod fragments in Fig.46(d) indicate that Lexan™ contact alone is sufficient to cause rod failure, resulting in rod segmenting due to fracture similar to that seen in shot #717 (shown in Fig. 45). These findings necessitated the change to the two-piece sleeve design mentioned in Section 6.1.2.1 to prevent Lexan™-rod interaction from inadvertently occurring. This shot was not repeated.

The flash x-ray photograph in Fig. 47 of shot #749, conducted at 2.55 km/s with EDM WNiCo alloy, tells a different story, in part because this experiment was conducted with a greater launch velocity. This resulted in the initial impact (nose) portion of the rod breaking into fragments, as confirmed in subsequent shots conducted with both alloys.

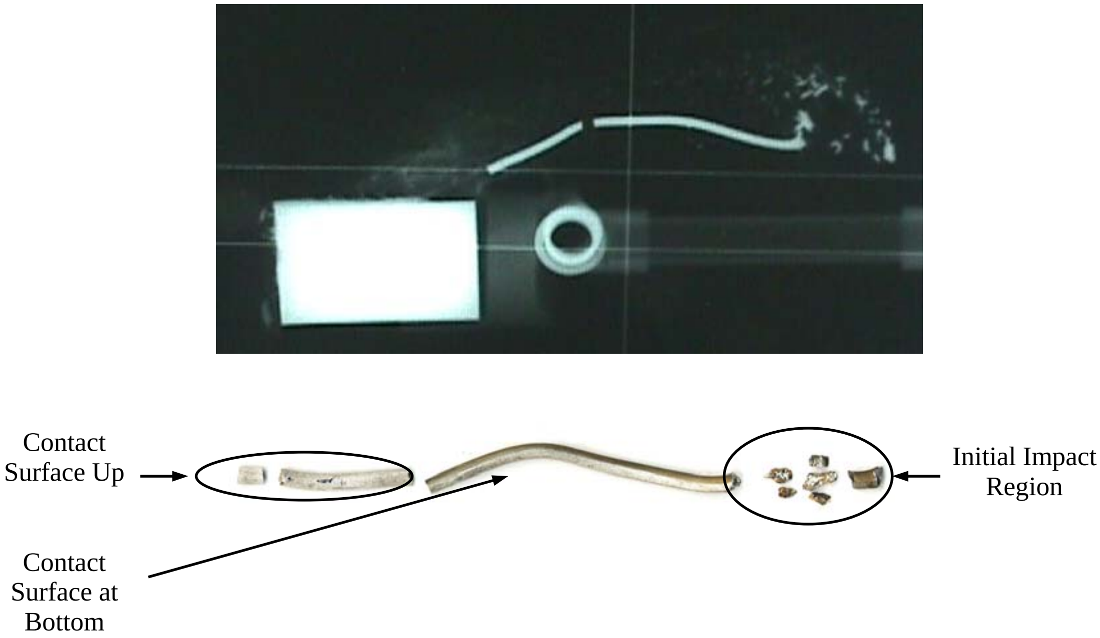

Figure 47: Shot #749 - EDM WNiCo Flash X-Ray Photograph and Recovered Rod Segments (🡐 Projectile Travel)

That notwithstanding, the WNiCo alloy behaved quite differently than its Fe-containing counterpart with the same surface finish, confirming the drop tower results indicating that WNiCo alloy has far more dynamic ductility than does the WNiFe alloy. The portion of the rod beyond the initial impact region was subjected to sliding contact and broke into only three segments with an average mass of 3.2 grams. These segments were separated by characteristically flat fractures indicative of fairly pure mode I (tensile) loading leading to failure.

A number of useful observations can be made from these test results. Overall, both alloys behaved in a fairly brittle manner, having fractured into numerous pieces with relatively flat fracture surfaces. Initial rod-target interaction regions were clearly evident on the contact surfaces of the rods, appearing as “chevrons” with peaks oriented up-range, toward the nose of the rods. These regions, evidenced by silver-tinting, grew until they encompassed half of the rod circumference, indicating that “slot-cutting” occurred in the targets. Qualitative energy-dispersive spectroscopy (EDS) analysis indicated that this silver-tinting was due to a thin layer of steel from the target deposited onto the rod surface. Slot-cutting is also indicated by overlapping of the rod and target in the flash x-ray photographs, as can be seen in Fig. 45.

Shots were conducted at various velocities between 2.2 km/s – 2.6 until a particular three-shot sequence with increasing velocities produced extraordinarily different results for rods of the same alloy and surface finish, revealing a WHA failure mode “velocity effect.” Shot #756, conducted at 2.35 km/s with SP WNiFe alloy, produced results similar to Shot #717 (conducted with EDM WNiFe at 2.30 km/s), segmenting due to fracture into fairly uniform pieces. Shot #757, a repeat of shot #756 conducted at 2.4 km/s and shown in Fig. 48, produced an altogether different outcome. The composite (combined static and dynamic flash x-ray photograph) image in Fig. 48 shows large debris swirls or “plumes” streaming off the rod in conjunction with rod-target contact.

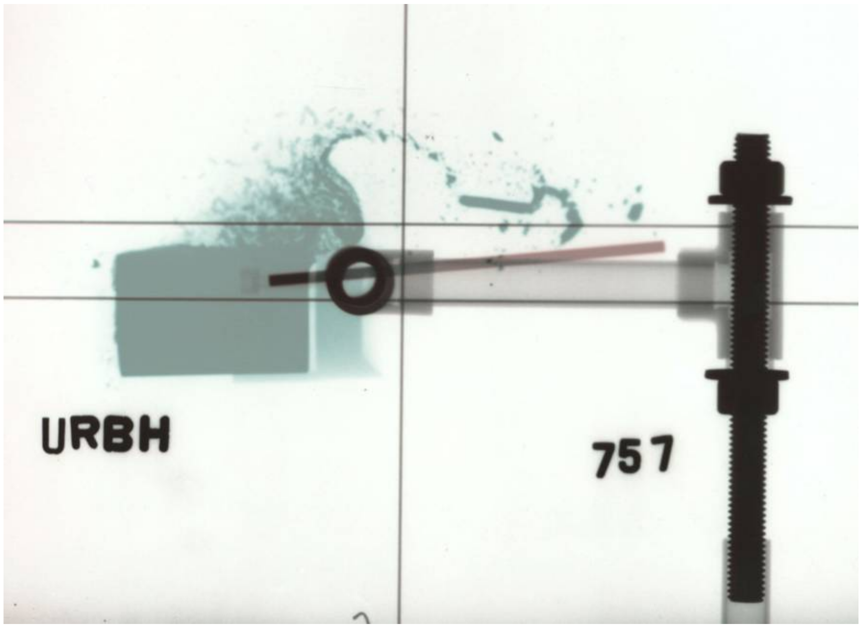

Figure 48: Composite Contact Print Image of Shot #757 - SP WNiFe
(← Projectile Travel)

Shot #756 was again repeated in shot #762 (related reverse-ballistic experiments were not necessarily conducted on consecutive shots, causing frequent gaps in shot numbers), this time at 2.60 km/s. As shown in Fig. 49, results similar to shot #757 were produced despite a late hit (far from the nose) on the rod. In both shots at 2.4 km/s or above, rod failure was catastrophic, producing numerous small fragments.

The recovered rod fragments conveyed the same story, though the difficulty in locating and removing tiny fragments from particleboard and, thus, their absence from the reassembled rod photos, prevented an accurate fragment count. The recovered rods also indicated "axial splitting" of the rod along its long axis as opposed to more typical fracturing along planes normal to the tensile axis.

Horizontal Flash X-Ray Images ↓ Vertical Flash X-Ray Images ↓

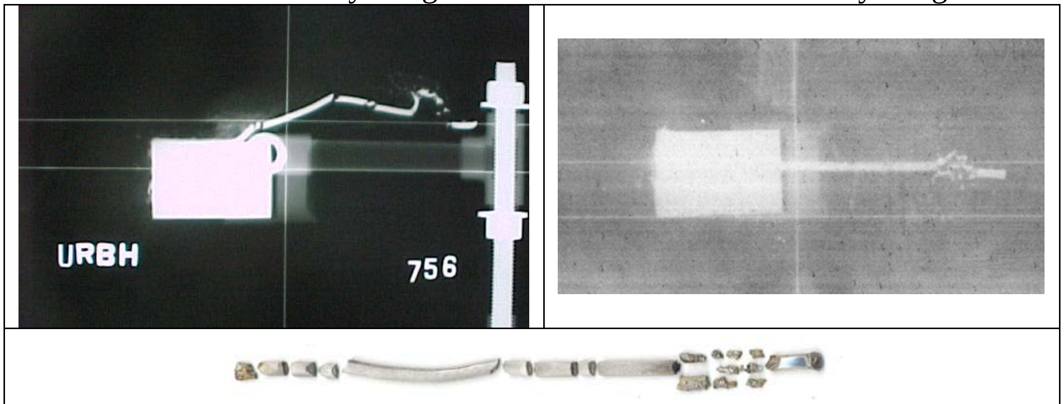

(a) Shot #756 @ 2.25 km/s

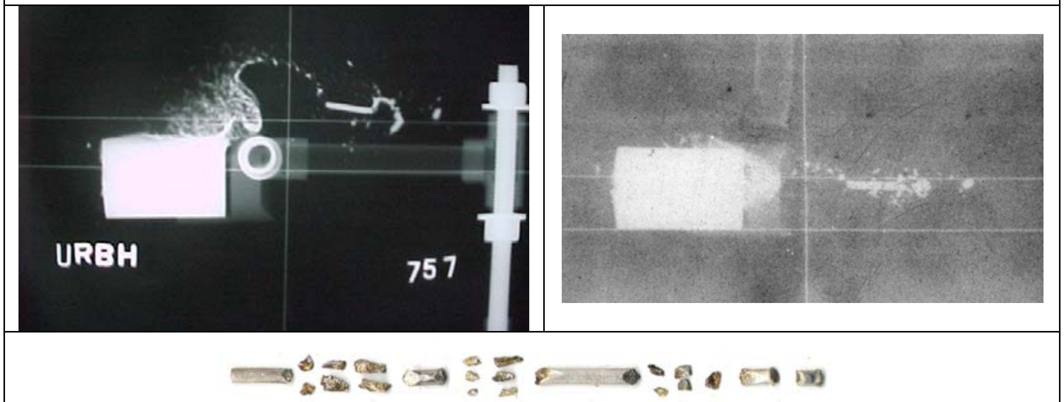

(b) Shot #757 @ 2.40 km/s

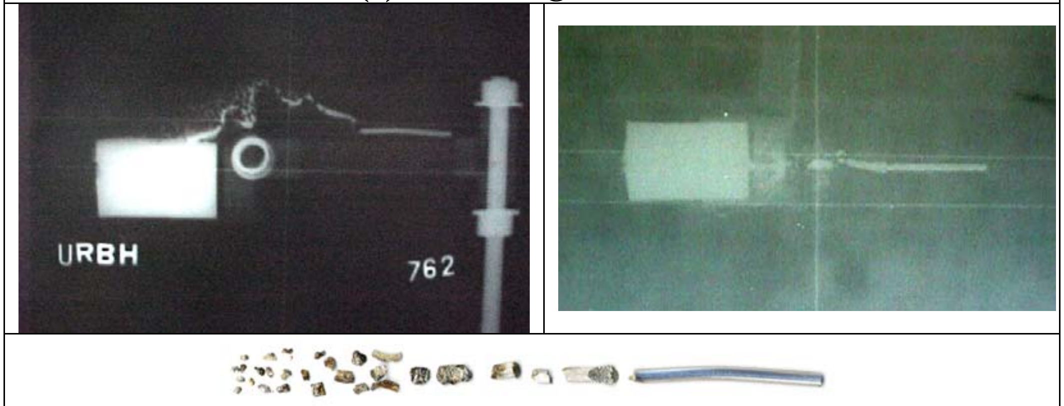

(c) Shot #762 @ 2.60 km/s

Figure 49: Series of Three SP WNiFe Reverse Ballistic Shots (← Projectile Travel)

Through examination of the recovered fragments and comparison with flash x-ray photographs, it became evident that the debris plumes were the result of hypervelocity gouging – the images are in fact images of gouge formation, which has never previously been observed. Rod gouges have a shiny, distorted appearance shown in Fig. 50, indicating the extreme loading conditions under which they are created, and the characteristic teardrop shape. This was a fortuitous outcome as one of the original intentions of transverse loading reverse ballistic testing was to serve as a gouge susceptibility screening test. More surprising was the apparent sensitivity of gouges to velocity and surface finish, even though gouging is well known to occur only when certain loading and velocity parameters are met.

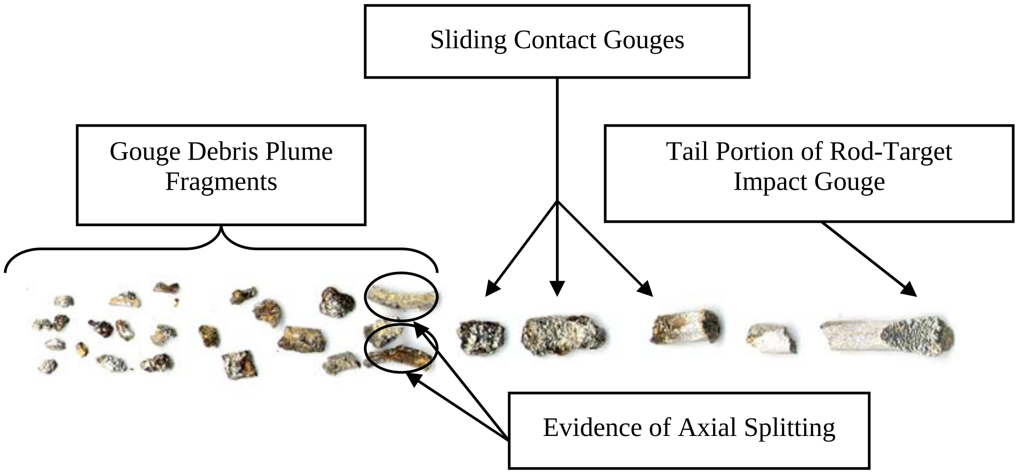

Figure 50: Close-up of Rod Debris and Gouges from Shot #762 – SP WNiFe
(← Projectile Travel)

6.2.1.1 Hypervelocity Gouging

Gouging is known to occur on contact surfaces in applications involving high-velocity sliding, such as rocket sleds and electromagnetic guns, but it has been reported only once previously on a cylindrical geometry in conjunction with ballistic testing [102]. Gouges usually appear in the teardrop shape shown in Fig. 51, with the wider end oriented “downstream” and characterized by a slightly raised lip.

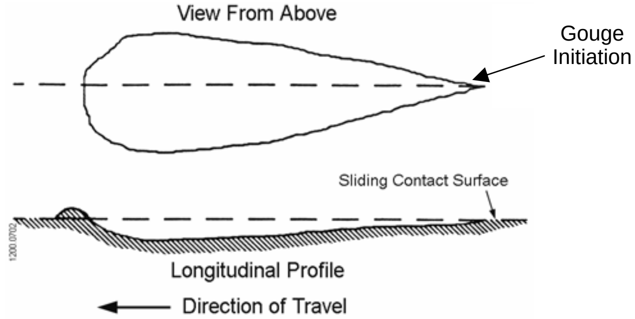

Figure 51: Sketch of a Typical Hypervelocity Gouge [adapted from 183]

Recent work on gouging confirms that it is the result of severe transient loading conditions at a high-velocity sliding interface. It occurs on both sliding surfaces in contact even though only one is usually recovered for examination (as in the case of these experiments), and its onset is somewhat predictable if the properties of the materials involved are known [184-186]. Using these methods of prediction, the gouging onset velocity for an interaction between WHA and steel is calculated to fall between 1.3 – 2.0 km/s, depending upon the approach used and the known or assumed material properties. Undoubtedly, loading conditions vary greatly over the many different experimental configurations reported to have produced gouging and used to develop the cited methodologies. In these experiments, gouging was never observed at velocities below 2.4 km/s or on EDM surfaces (of either alloy). Because of this, and the evidence of gouge onset in the form of flash X-ray photographs and recovered rod fragments, it is expected that gouging onset occurs at or about 2.4 km/s for the conditions in these experiments, surface and loading condition permitting. Further proof is that initial rod-target impact at or above this velocity always produced gouge-like features whether or not gouging occurred during subsequent sliding contact (which did not happen in the case of the EDM rods); this was not the case at velocities below 2.3 km/s. Accordingly, all subsequent experiments were conducted at velocities greater than 2.4 km/s, and the gouges most closely considered were those away from the point of initial contact, resulting only from sliding contact between the RHA packages and the WHA rods. Seventeen of the twenty-three hypervelocity experiments were conducted in this high-velocity range.

6.2.1.2 Surface Finish Influence on Gouge Formation and Catastrophic Rod Failure

Representative results for both alloys and all surfaces finishes are reflected in Fig. 52. A complete listing of reverse-ballistic experiments conducted is shown in Appendix A. For determination of repeatability, at least two shots for every alloy-surface finish combination were conducted, with the exception of the EP-only shots; only one EP-only shot was conducted for each alloy. All shots presented in Fig. 52 were conducted at 2.4 km/s or greater launch velocities.

	WNiFe	WNiCo
EDM	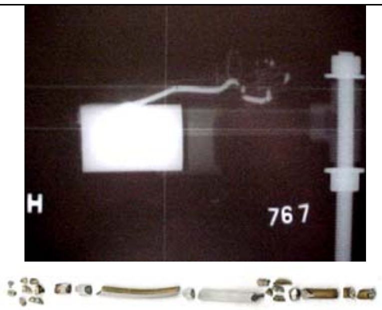	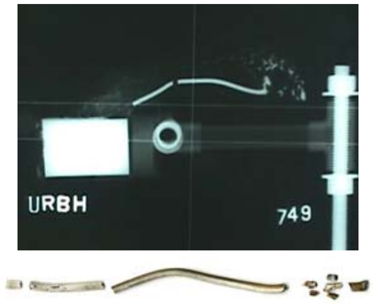
SP	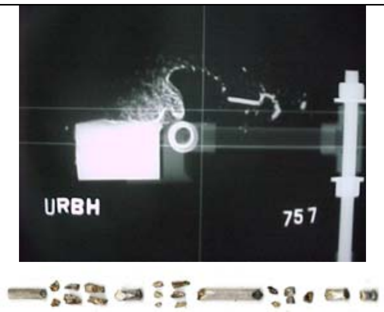	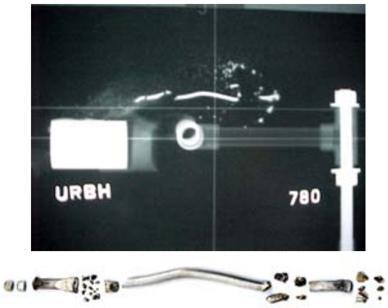
EP	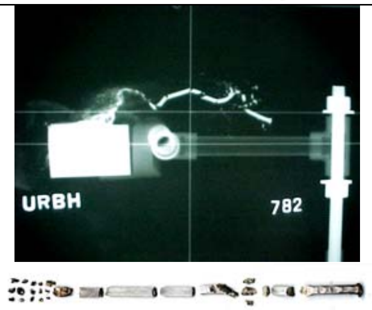	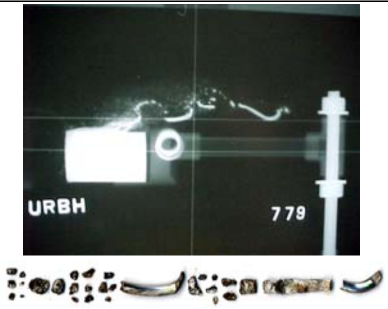
CG	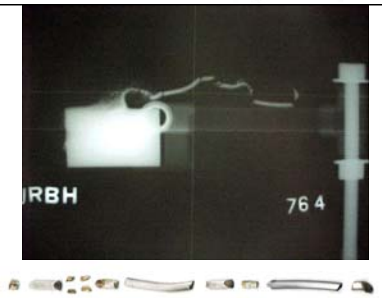	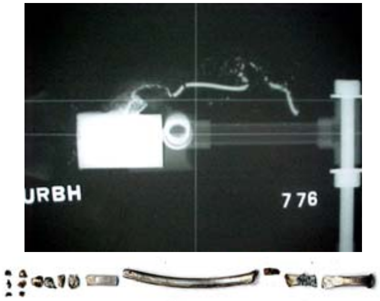
CG-SP-EP	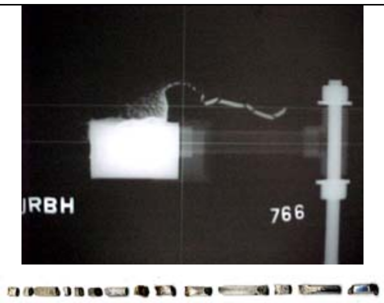	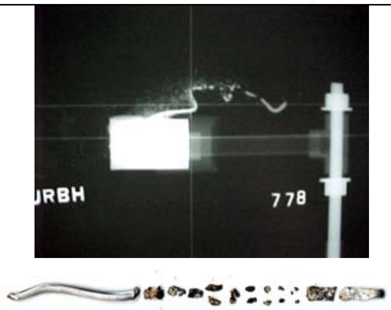

Figure 52: Reverse Ballistic Horizontal Flash X-Ray Photographs and Recovered Rod Segments and/or Fragments (← Projectile Travel)

Both alloys demonstrated a trend toward gouge development and fragmentation failures with surface finish improvement, revealing a WHA failure mode “surface finish effect” in conjunction with the already identified “velocity effect.” Gouging always led to rod failure. In the most extreme case for each alloy, SP for WNiFe and EP for WNiCo, rods failed catastrophically by similar fragmentation. Fragmentation failures between the two alloys are virtually indistinguishable by inspection alone, as shown in Fig. 53. This is unexpected because of the ease of distinguishing between failed EDM specimens.

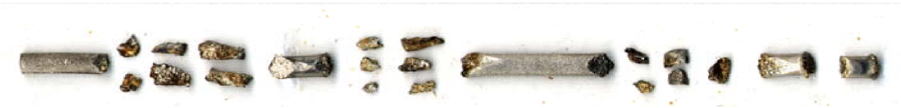

(a) Shot #757 - SP WNiFe

(b) Shot #779 - EP WNiCo

Figure 53: Recovered Reverse Ballistic Rod Fragments (← Projectile Travel)

6.2.2 Data Analysis

6.2.2.1 Average Initial Flaw Size and Fragment Mass Correlations

Recovered rod fragments were used to seek a relationship between surface finish, i.e. decreasing average initial flaw size, and fragment size. A decrease in fragment size with improved surface finish is indicated by the dynamic flash x-ray photographs. Because smaller average fragment sizes make fragments more difficult to locate in and recover from the particleboard, the average recovered fragment mass for a fragmented rod is heavily dependent upon both the average fragment mass and the number of fragments. For these reasons, the mass fraction of rod recovered and the average recovered fragment mass for both alloys are correlated in Figs. 54 and 55, respectively, with the measured average WHA initial flaw sizes from Table 8 for all shots at velocities above 2.4 km/s. As was done with drop tower data, in both plots a linear curve fit has been applied to EDM, SP, and EP data points, i.e. those with measurable initial flaw sizes, and this curve fit has been extrapolated to smaller initial flaw sizes. Data points for the CG and CG-SP-EP finishes are shown using the average Ra values for these finishes (0.26 and 0.27, respectively) as an approximate measure of initial flaw size, but these data are not included in the curve fit analysis.

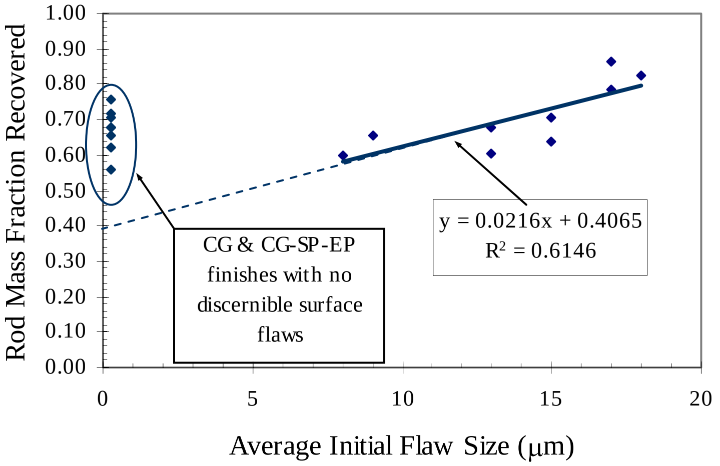

Figure 54: WHA Mass Fraction Recovered vs. Average Initial Flaw Size

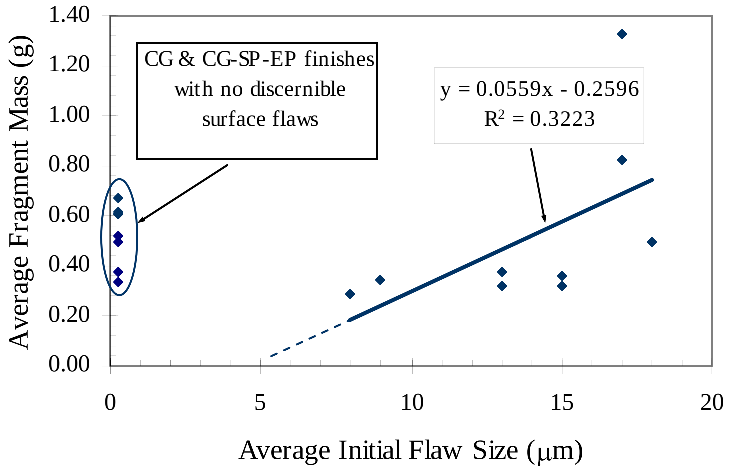

Figure 55: WHA Average Fragment Mass vs. Average Initial Flaw Size

Both of these metrics seem to indicate a correlation with initial flaw size. It appears that decreasing initial flaw size leads to decreasing fragment size, indicating that fragmentation failure is more pronounced as surface finish is improved. However, it is difficult to draw any conclusions from these data even if the trends are correct.

6.2.3 Slot Cutting Efficiency

A new “slot cutting efficiency” parameter was defined for all tests conducted at or above 2.4 km/s from information available in the flash X-ray photographs. From the flash X-ray photographs, the depth and length of slots cut into the projectiles by the WHA rods were determined. These parameters were used to approximate slot area, assumed to be a triangle; slot volume could not be determined as the slot width could not be measured. In Fig. 56 the apparent length, depth, and area are indicated, as is a portion of an “embedded rod” not yet ejected from the slot.

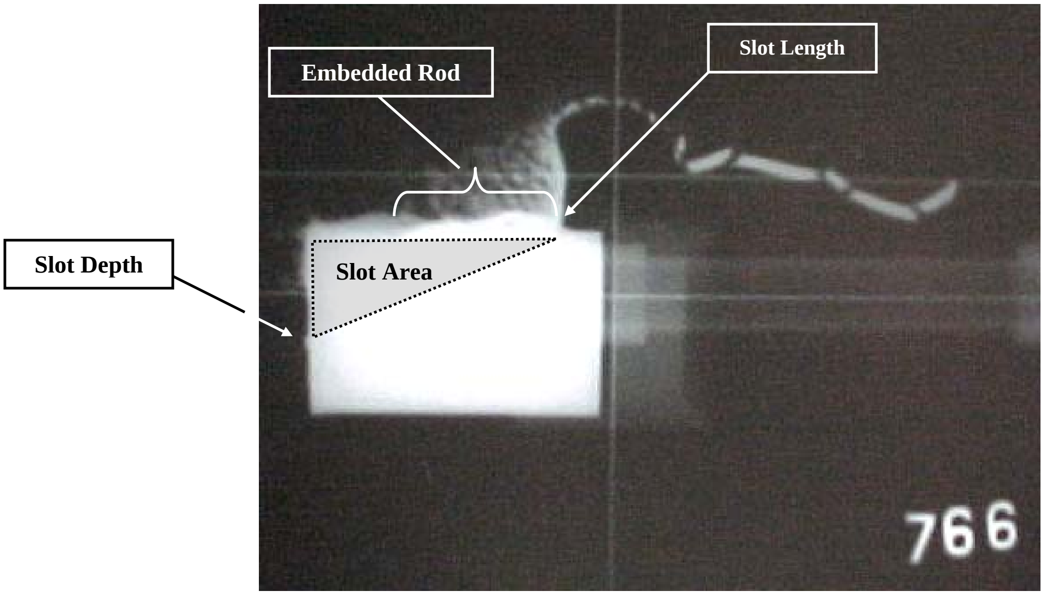

Figure 56: Dynamic Flash X-Ray Photograph From Shot #766 (CG-SP-EP WNiFe) Showing Approximate Slot Area and Embedded Rod Segments (← Projectile Travel)

Slot area values were normalized by the surface area of rod in contact, assumed to be half of the rod circumference multiplied by the length of rod involved in slot cutting, or the "engaged" rod length. Embedded rod length, as in the case of shot #766 in Fig. 56 was subtracted from the engaged rod length. These values were multiplied by the impact velocity, then further normalized by the gouging onset velocity, taken to be 2.4 km/s, resulting in a dimensionless slot-cutting efficiency parameter, E_s, where:

$$E_s = \frac{l_s d_s V_i}{l_r \frac{\pi d_r}{2} V_g} \qquad (6.1)$$

and: l_s = measured slot length

d_s = measured slot depth

V_i = target-rod impact velocity

l_r = engaged rod length = measured rod length – distance of initial target-rod impact from rod nose – embedded rod length (if any)

d_r = rod diameter calculated from initial rod mass and length

V_g = gouging onset velocity determined from experimental results ≈ 2.4 km/s

E_s, will exceed 1.0 when the resulting slot area exceeds the rod surface area involved in cutting the slot.

The slot cutting efficiencies of all shots conducted above 2.4 km/s are correlated with initial flaw sizes in Fig. 57. These data again reflect linear curve fits extrapolated to smaller initial flaw sizes, and data points for the CG and CG-SP-EP finishes again assume the initial flaw size to be equal to the average Ra values for these finishes (0.26 and 0.27, respectively) and are omitted from the curve fit analysis. Data from shot #762 is reflected in Fig. 57 but also omitted from the linear curve fit because it involved an anomalously late hit on the rod (shown in Fig. 49(c)). Calculated values for E_s are shown in Appendix A.

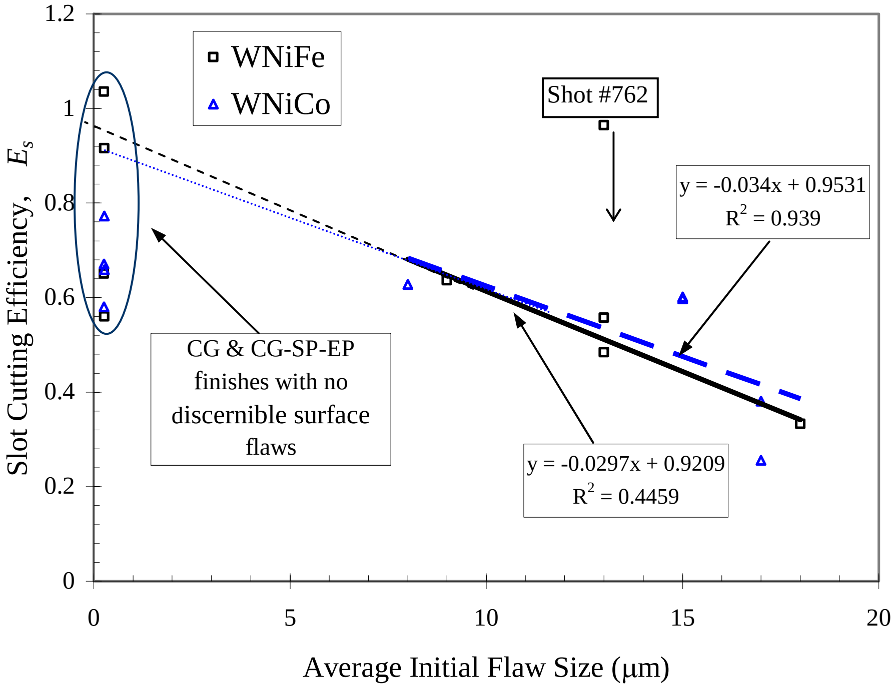

Figure 57: WHA Slot Cutting Efficiency versus Average Initial Flaw Size

Fig. 57 suggests a strong correlation between slot-cutting efficiency and average initial flaw size for both WNiFe and WNiCo, indicating that surface finish influences the slot cutting efficiency of WHA. When flaws are present, they dominate slot cutting efficiency relationships shown in Fig. 57. Slot cutting efficiency is improved by reducing the average initial flaw size, even though this leads to gouging and rod failure due to fragmentation.

6.3 REVERSE BALLISTIC SPECIMEN SEM ANALYSIS

6.3.1 Exterior Tensile Surfaces

As with the drop tower specimens, clear trends emerge upon studying tensile surfaces approaching and adjacent to fractures on reverse ballistic specimens. For both alloys and all surface finishes, fracture is largely initiated by isolated W grain cleavage. This process is accentuated by the presence of preexisting surface W grain microcracks and significant linking thereof.

Damage once again progressively accumulates toward final fracture surfaces, with the largest incipient fractures occurring approximately 200 μm laterally apart, as shown in Fig. 58.

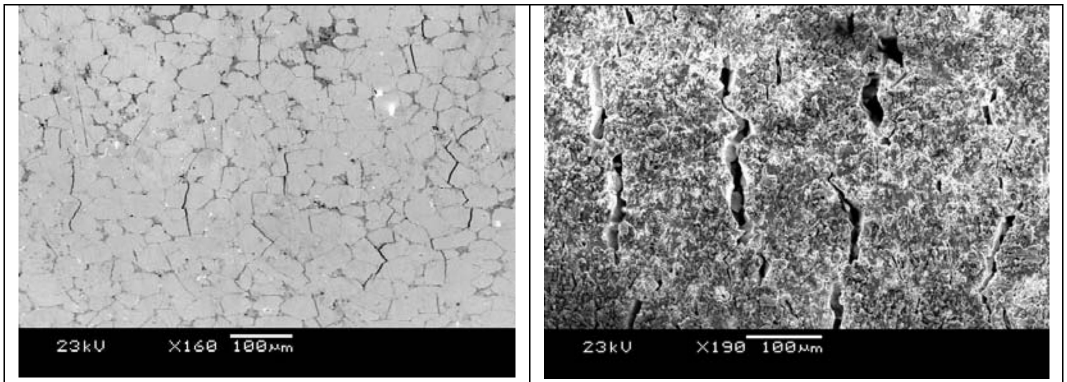

(a) Shot #757 - SP WNiFe

(b) Shot #751 - EDM WNiCo

Figure 58: Parallel Incipient Fracture Arrays (Tensile Stress Orientation ←→)

Unlike the drop tower specimens, damage on the reverse ballistic specimens appears to be periodic, in that the tensile surfaces of most specimens analyzed displayed alternating regions of little and great damage accumulation, as shown by the schematic in Fig. 59. A typical failed rod segment has arrays of surface cracks which are least dense at the rod segment's up-range end (i.e. toward the nose of the rod), moderately dense near the middle of the segment, and most dense near the down-range fracture surface.

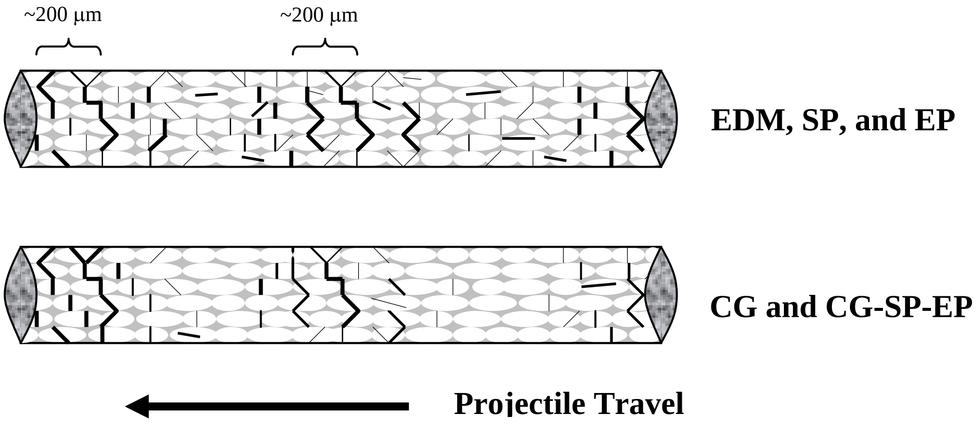

Figure 59: Reverse Ballistic Specimen Tensile Surface Representations with Fracture Surfaces on Both Ends (Tensile Stress Orientation←→)

This same pattern of surface damage accumulation held true for both alloys and all finishes, though specimens with an absence of preexisting surface flaws (CG and CG-SP-EP) typically have little or no apparent surface damage in regions between those with significant accumulations. Conversely, and though not always the case, specimens with significant preexisting flaws were observed that had a fairly uniform presence of "opened" flaws across their entire tensile surface. Unlike the observations from drop tower specimens, microcracks aligned with the tensile axis (i.e. long axis of W grains) were sometimes affected by reverse ballistic loading, not just those normal to the tensile axis, as shown by the schematic in Fig. 59.

The periodicity of fracture development may be due to transient loading of the rods from passing contact with the projectile, the result being an increasing population of developing fractures until one became critical. A critical fracture can relieve the load in the rod and quench all adjacent fractures. If the conditions required for gouging are met prior to those required for fracture of preexisting flaws, then fragmentation occurs. This can shed some light on why only surface-improved rods gouge, while those with large preexisting surface flaws (i.e. EDM) merely fracture.

Though dominated by W grain cleavage, fracture development also included W-W grain boundary failure and sometimes a combination of both failure modes in conjunction with single W grains, as shown in Fig 60. That coupled with the predominance of W grain cleavage conveys the close competition between the two modes, yet one in which W-W bond strength is generally greater than that of individual W grain cleavage strength.

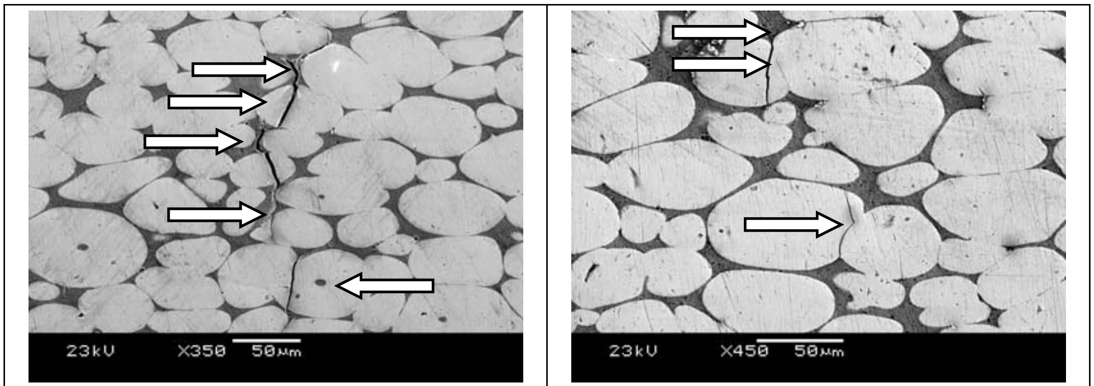

(a) Matrix Blunting and Crack Deflection, Matrix-W Grain Separation, Matrix Failure, and Irrelevant W Grain Porosity

(b) Matrix Blunting, W Grain Cleavage in Lieu of W-W Grain Separation, and Vice Versa

Figure 60: Shot # 765 - CG-SP-EP WNiFe Reverse Ballistic Specimen Tensile Surface Detail (Tensile Stress Orientation←→)

Matrix failure and matrix-W grain separation remain primarily fracture propagation (as opposed to initiation) means, which act to link W grain cleavages and/or W-W grain separations. Many instances of grain porosity are present but do not appear to be a significant factor in fracture development, as can also be seen in Fig. 60.

Instances of axial splitting were also visible on the up-range end of the tensile surfaces of some specimens. Axial splits emanate from gouges and run lengthwise along the rod segment, as shown in Figs. 61 and 62. This is true for initial contact gouges and subsequent sliding contact gouges. As with other tensile surface fractures, axial splits are dominated by W grain cleavage. The fractures shown in Figs. 61 and 62 suggest a tangential failure due to the asymmetric application of an external load on a cylindrical geometry.

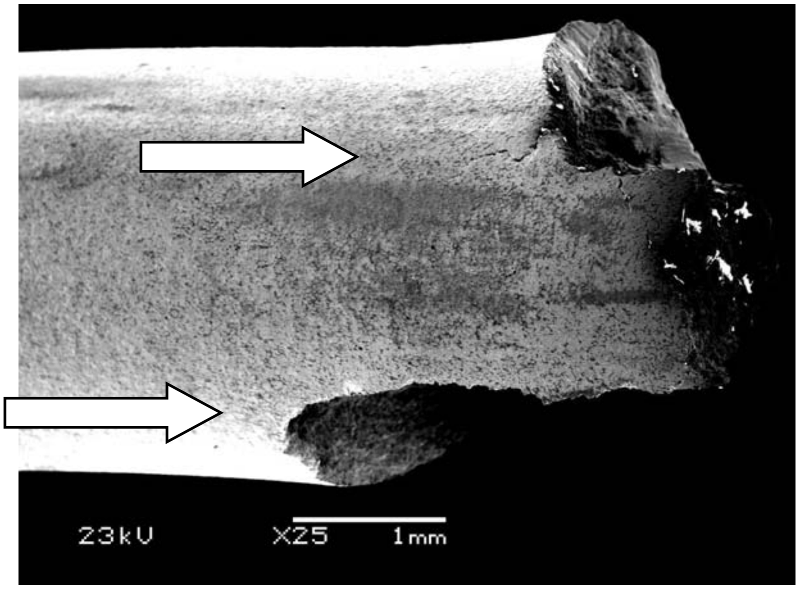

Figure 61: Shot #779 - EP WNiCo Reverse Ballistic Tensile Surface Specimen Showing Axial Splitting at Tail of Preceding Gouge (← Projectile Travel)

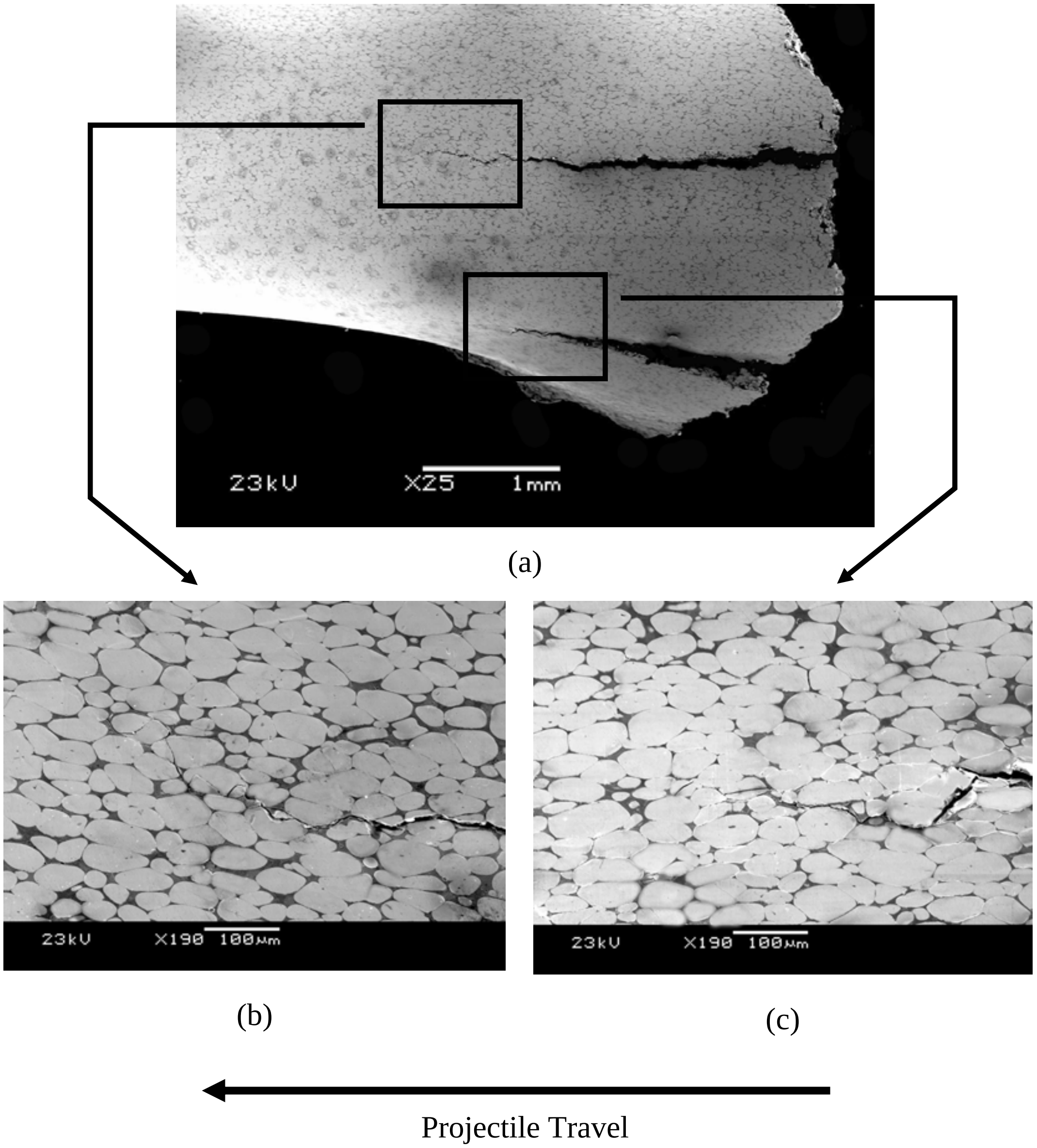

Figure 62: (a) Non-contact (Tensile) Surface of Shot #765 - CG-SP-EP WNiFe Reverse Ballistic Specimen With Axial Splits at Downrange End of Preceding Gouge; (b) Blunting and Process Zone of Primary Split; (c) Blunting and Process Zone of Secondary Split

6.3.2 Tensile Surface Normal Cross-Sections

For both drop tower and reverse ballistic specimens, surface damage accumulation has been observed to be most significant adjacent to fractures which lead to rod failure. In the case of reverse ballistic specimens, this is particularly true for damage accumulation on the up-range side of a fracture toward the nose-end of rod pieces. For these reasons, the focus of surface, normal cross-section, and fracture surface analysis was tensile surfaces immediately adjacent to down-range fractures toward the tail-end of recovered rod pieces.

In considering the surface condition extremes for the two alloys, EDM and CG-SP-EP, it was clear that the trends observed from WNiFe drop tower experiments also held for reverse ballistic testing of both alloys considered. EDM specimens were dominated by surface initiated W grain cleavages, though the WNiCo alloy did exhibit a limited number of internal cleavage sites. Although depths of penetration into the body of the rod varied, observations of the distribution of fractures initiated on tensile surfaces after drop tower testing and reverse ballistic tensile surfaces show the largest cracks to be uniformly spaced approximately 200 μm apart. In contrast, CG-SP-EP surface improvement greatly reduces the damage visible at a 90x magnification for both alloys, and the largest fractures are linked W grain cleavages nucleated in the interior of the rod segments, as shown in Fig. 63. In the case of the WNiCo specimens, the proximity of internal fractures to the tail end of the segment and the absence of any other incipient fractures makes a strong case for rod failure from internally nucleated damage; this is less clear for the WNiFe CG-SP-EP specimen.

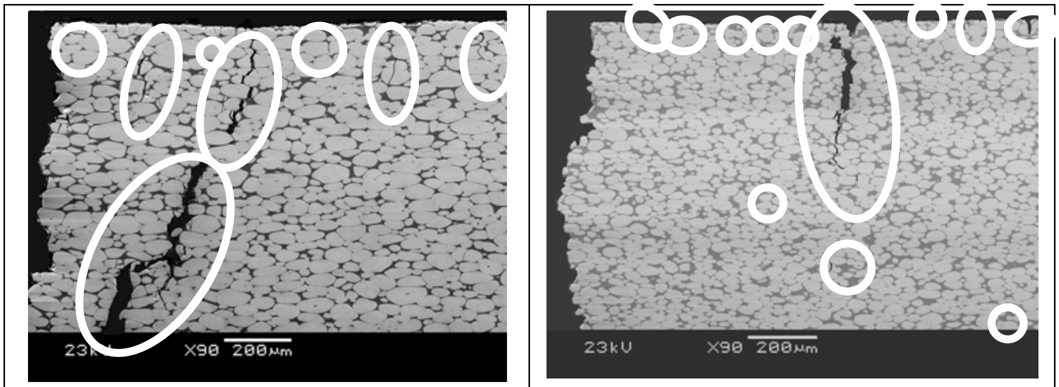

(a) Shot #717 - EDM WNiFe | (b) Shot #751 - EDM WNiCo

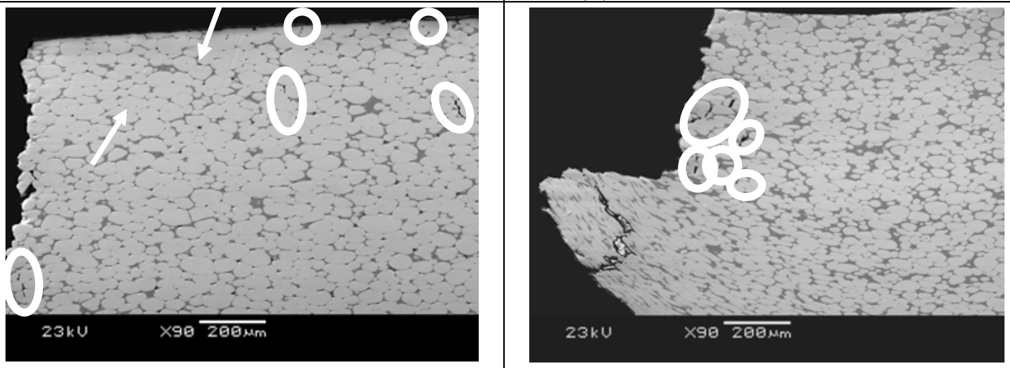

(c) Shot #765 - CG-SP-EP WNiFe | (d) Shot #777 - CG-SP-EP WNiCo

Figure 63: WHA Reverse Ballistic Specimen Normal Cross-Sections of Tensile (at Top) and Fracture (at Left) Surfaces (Tensile Stress Orientation ←→)

The trends observed during drop tower testing with WNiFe are consistent with the previously described results, and with the SP, EP, and CG reverse ballistic cross-sections shown in Fig. 64. The SP and EP specimens have far less damage accumulation than the EDM specimens. CG specimens reflect an increased amount of damage over those that are EP'd.

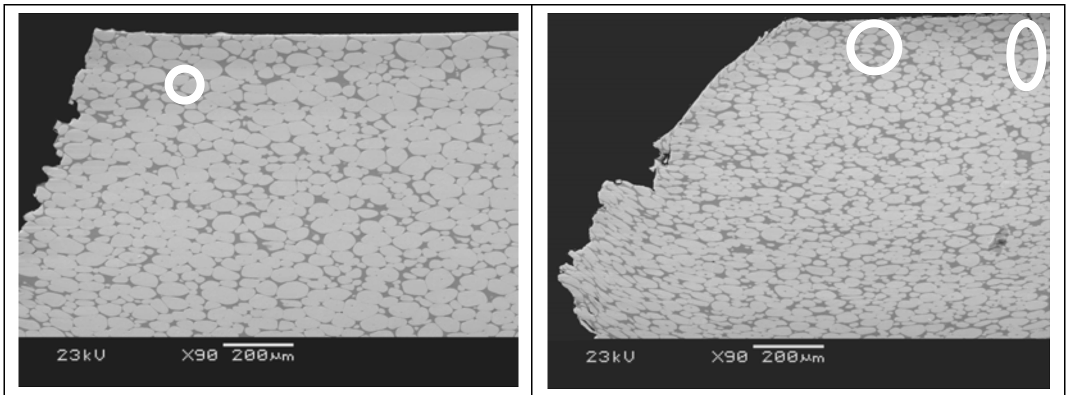

(a) Shot #757 - SP WNiFe

(b) Shot #781 - SP WNiCo

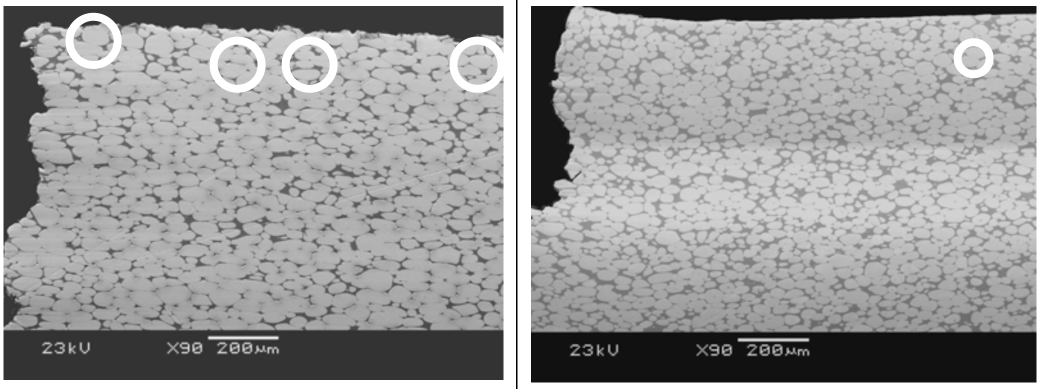

(c) Shot #782 - EP WNiFe

(d) Shot #779 - EP WNiCo

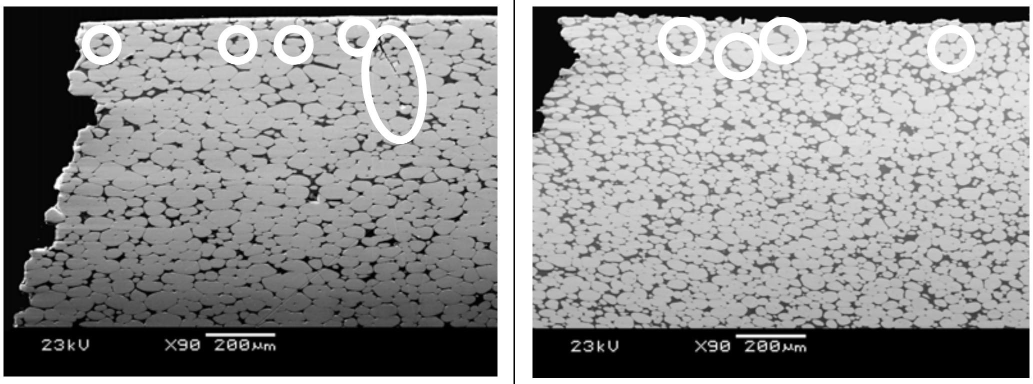

(e) Shot #763 - CG WNiFe

(f) Shot #776 - CG WNiCo

Figure 64: WHA Reverse Ballistic Specimen Normal Cross-Sections of Tensile (at Top) and Fracture (at Left) Surfaces (Tensile Stress Orientation ←→)

6.3.3 Compressive Surfaces

Rod surfaces that were in contact with the passing projectile but not involved in gouging or fracture have a similar appearance for both alloys and all surfaces finishes. These surfaces had a "scoured" appearance that left W grains exposed, and displayed mottled features with unusual patterns and microcracks in the matrix regions and around W grains, as shown in Fig. 65(a). This suggests melting, partial removal of matrix material, as well and the deposition and solidification of a melt-lubrication layer from the projectile, as previously confirmed by EDS analysis. By zero-biasing the SEM's electron detector so that only backscatter electrons (BSE's) and no secondary electrons (SE's) are captured, even more revealing images are created, as shown in Fig. 65(b).

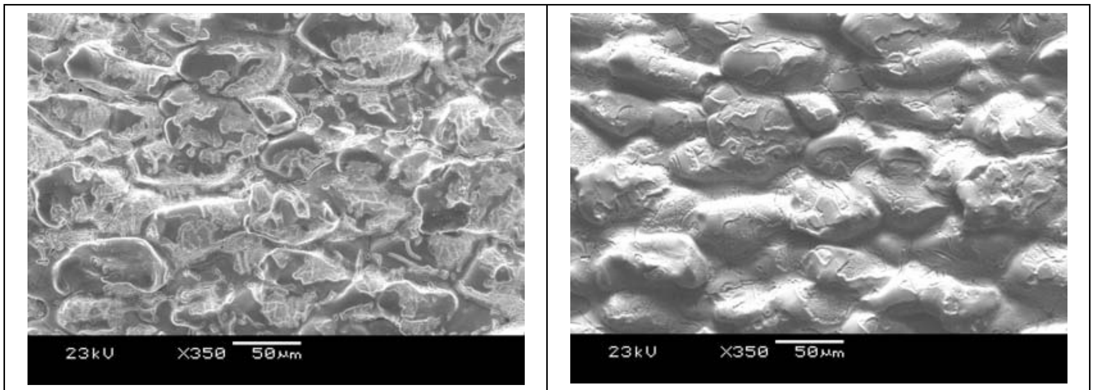

(a) SE's and BSE's

(b) BSE's Only

Figure 65: Shot #767 - EDM WNiFe Sliding Contact Surface SEM Images
(← Projectile Travel)

6.3.4 Hypervelocity Gouging

Recovered specimens with gouges were examined. Transient loading induced by high velocity sliding contact acts first at a discrete location, triggering an expanding region of significant plastic surface deformation, as shown in Fig. 66.

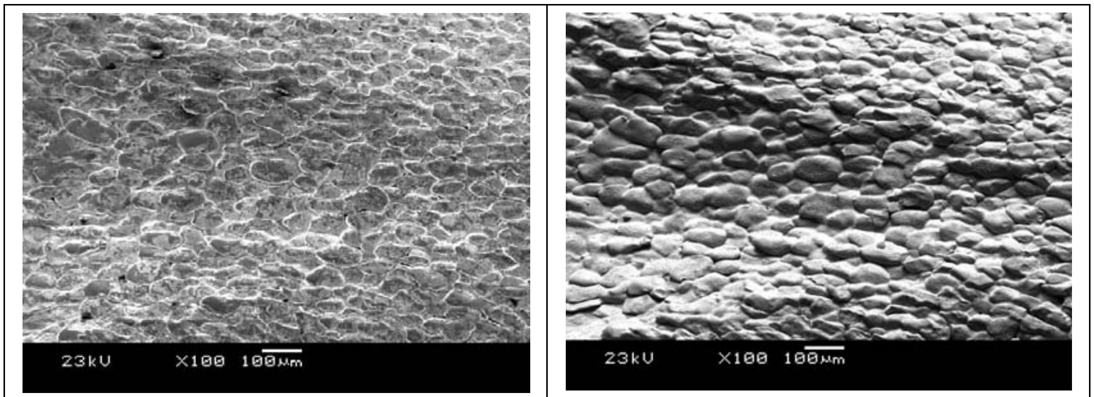

(a) SE’s and BSE’s

(b) BSE’s Only

Figure 66: Shot #757 - SP WNiFe Sliding Contact Surface SEM Images of Gouge Initiation Region (← Projectile Travel)

Contact conditions become more severe as the gouge region expands, leading to surface melting and material removal, as well as gross W grain deformation. This causes a scaly, smeared appearance as W grains are elongated, flattened, and overlapped, as shown in Fig. 67(a). Contact surfaces on the rod and target are expected to gouge simultaneously, and material from the growing crater(s) is drawn downrange as the transient load begins to diminish. Gouges terminate with a lip of this material pushed up at the tail end of the gouge as shown in Fig. 67(b), followed by the region of gradually diminishing surface melting and solidification seen in Fig. 67(c). As steady- state contact conditions resume, the surface reverts to the more usual, scoured appearance of Fig. 67(d).

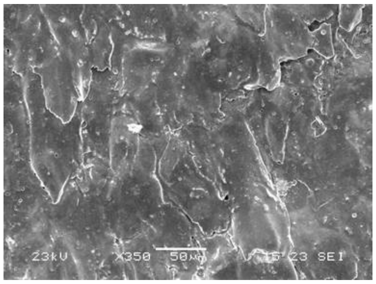

(a) Gouge Surface Interior

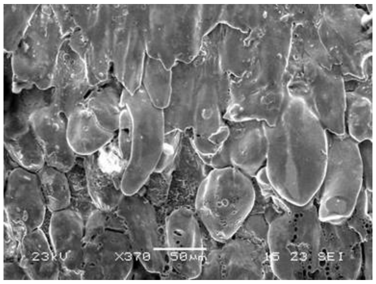

(b) Downstream Gouge Lip

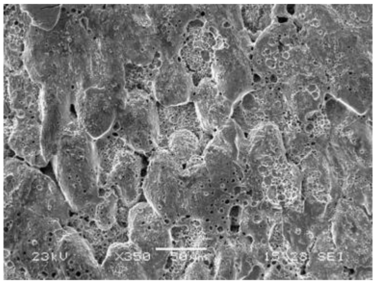

(c) Near Beyond Gouge

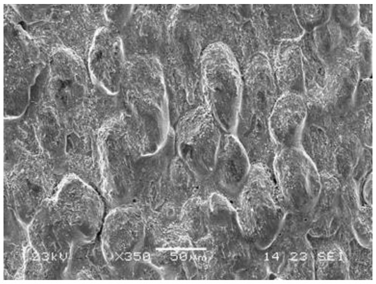

(d) Far Beyond Gouge

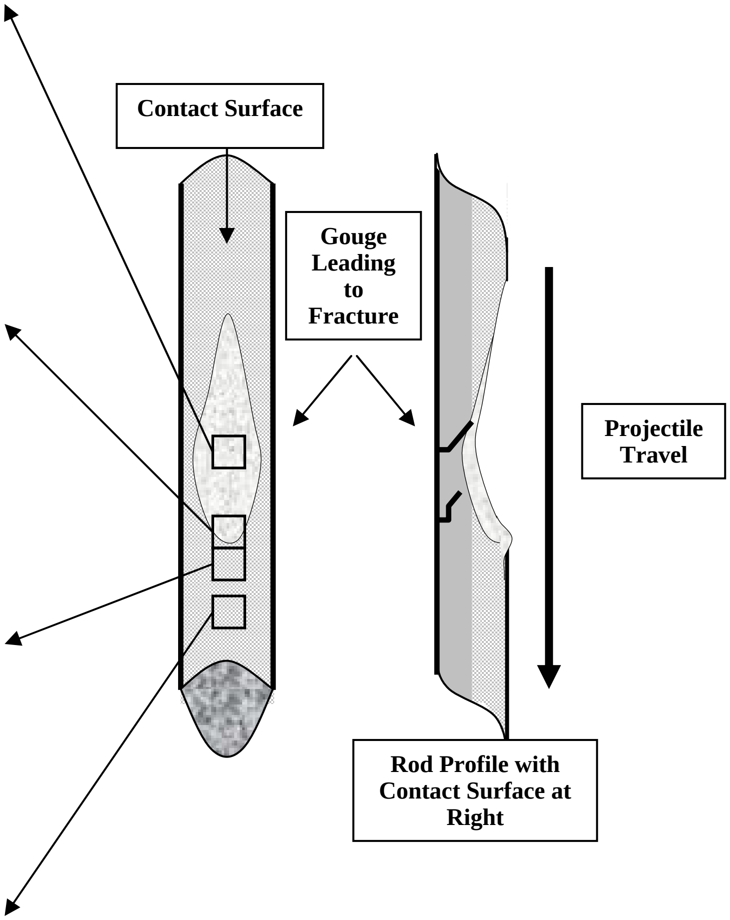

Figure 67: Shot #757 - SP WNiFe Gouge Crater and Nearby Surface Details

6.3.5 Micro-Gouging

An observation that has not previously been reported is “micro-gouging.” Microgouges have all of the same features of normal gouges but are only a fraction of the size. A normal gouge typically has a size of the same length scale as the surface on which it was created. Gouges of this type were no less than 5 mm in length; the largest were anywhere from two to three times that length. Normal gouges typically spanned the entire 3 mm rod diameter. In contrast, micro gouges were an order of magnitude smaller; examples of microgouges are shown in Fig. 68. Microgouges were observed in the initiation region of larger (normal) gouges, and along a long abrasion on the non-contact (tensile surface) of a rod segment.

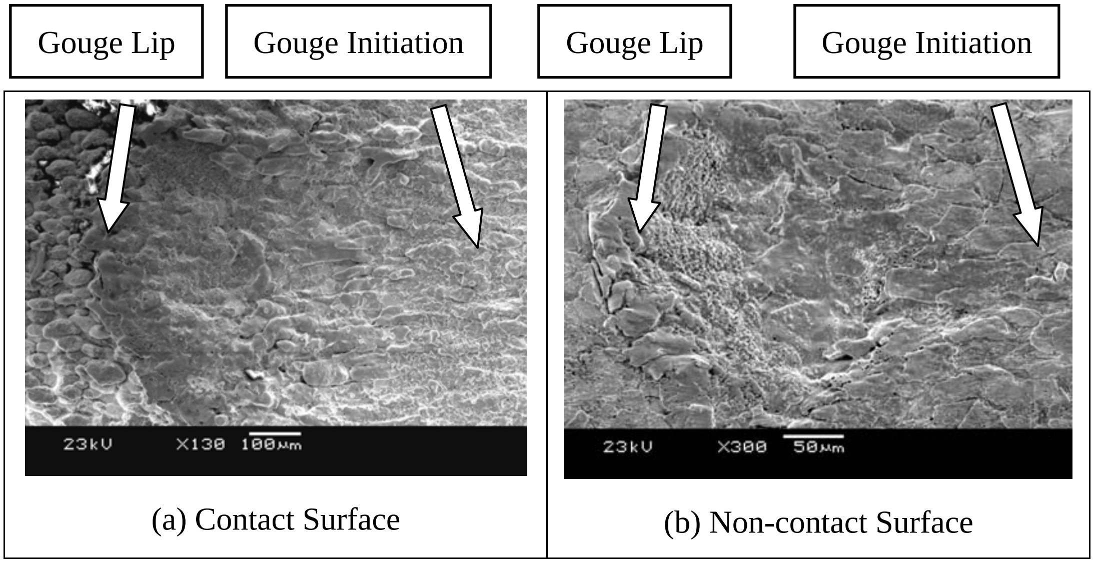

(a) Contact Surface

(b) Non-contact Surface

Figure 68: Micro Gouges on an Shot #781- SP WNiCo Reverse Ballistic Specimen (← Projectile Travel)

6.3.6 Compressive Cross-Sections

The appearance of cross-sections away from fractures and gouging reinforce the observations of sliding contact surfaces, revealing partially exposed grains and removal of matrix material, as shown in Fig. 69. The WNiCo alloy routinely demonstrates greater W grain elongation in this region than does the WNiFe alloy.

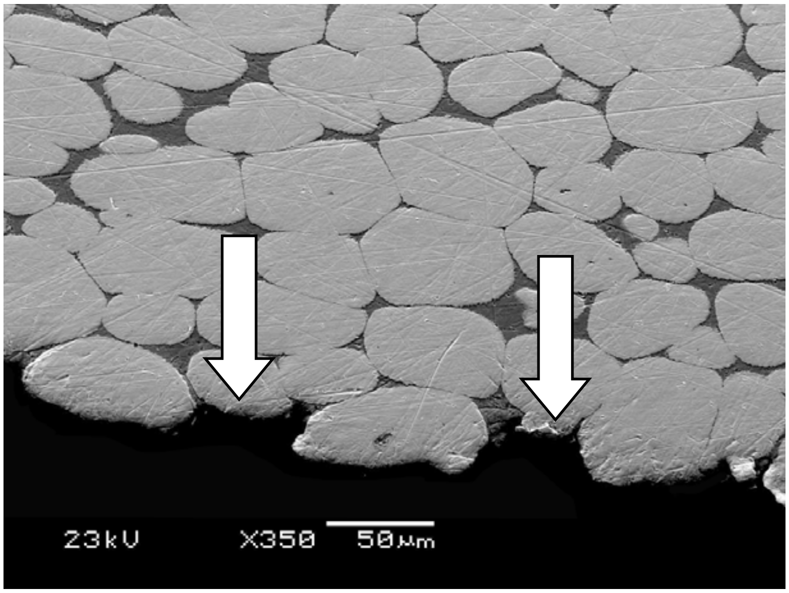

Figure 69: Contact Surface of Shot #763 - CG WNiFe Reverse Ballistic Specimen Showing Matrix Removal and Grain Exposure (← Projectile Travel)

In regions where gouging either initiated or subsided, the situation was different. The deformation of surface W grains observed on the gouge surfaces was most extreme. There was also an unmistakable transition from "normal" contact surface wear and matrix removal to that of W grain elongation, and eventually to significant surface distortion and undulation indicative of contact surface instability, as shown in Fig. 70.

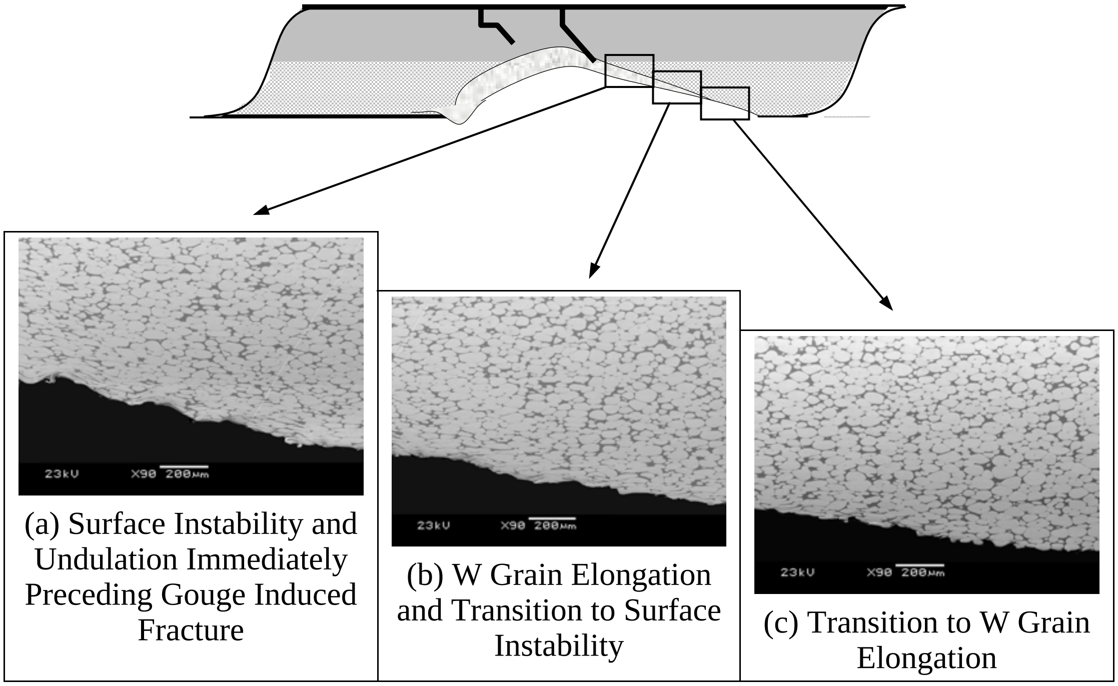

(a) Surface Instability and Undulation Immediately Preceding Gouge Induced Fracture

(b) W Grain Elongation and Transition to Surface Instability

(c) Transition to W Grain Elongation

Figure 70: Shot #757 - SP WNiFe Reverse Ballistic Specimen Contact Surface Reflecting Transition from Normal Wear to Gouging (← Projectile Travel)

This progression was observed in every specimen in which gouging was occurred. Features unique to these gouge-initiated failure regions, some of which can be seen in Fig. 71, include: fractures initiating at rod ends and running axially, at the compressive surface and running toward the tensile surface, or some combination of both; significant W grain and matrix ductility prior to failure; shear banding; and internally nucleating fractures.

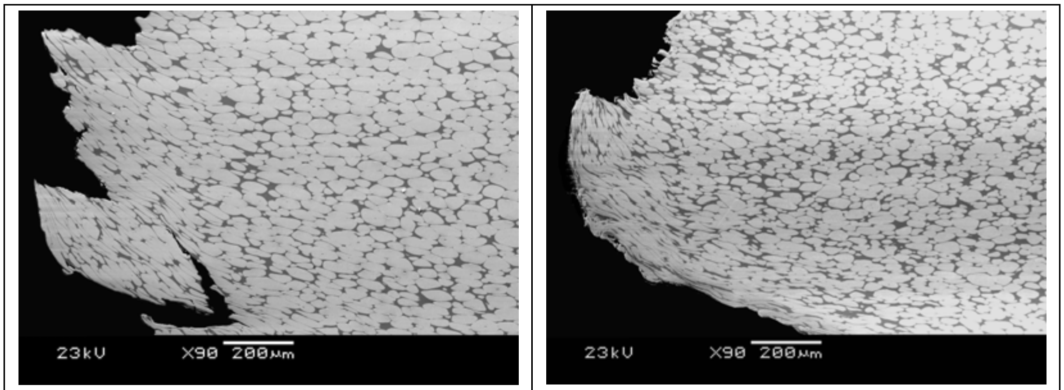

(a) Shot #757 - SP WNiFe

(b) Shot #779 - EP WNiCo

Figure 71: WHA Reverse Ballistic Specimen Cross-Sections Showing Gouged Contact Surface and Fracture Surface (← Projectile Travel)

Surface W grains are distorted, some either toward the tensile surface or back upon themselves, forming the “swirls” seen in Fig. 72. The most grossly elongated grains provide local engineering strain estimates of greater than 100%.

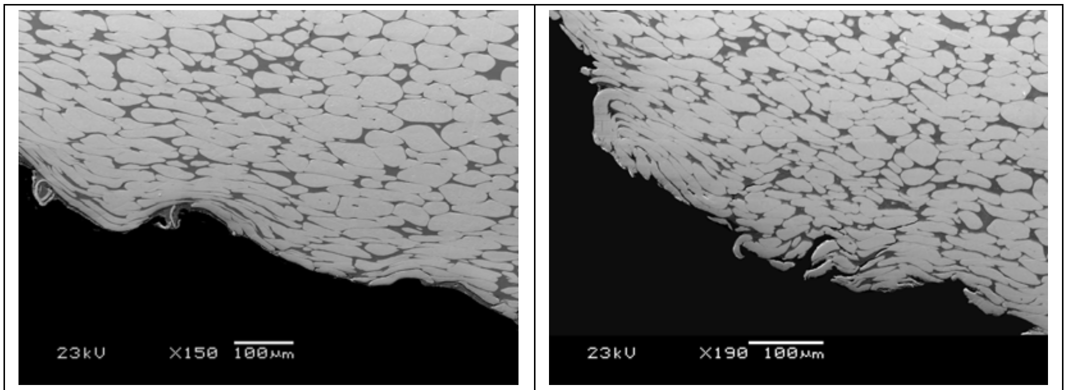

(a) Shot #757 - SP WNiFe

(b) Shot # 779 - EP WNiCo

Figure 72: WHA Reverse Ballistic Specimen Cross-Sections Showing Gouged Contact Surface Features Adjacent to Fracture (← Projectile Travel)

These are reminiscent of jet formation associated with gouging and/or explosive welding and reported in the literature. An example microstructure is shown in Fig. 73.

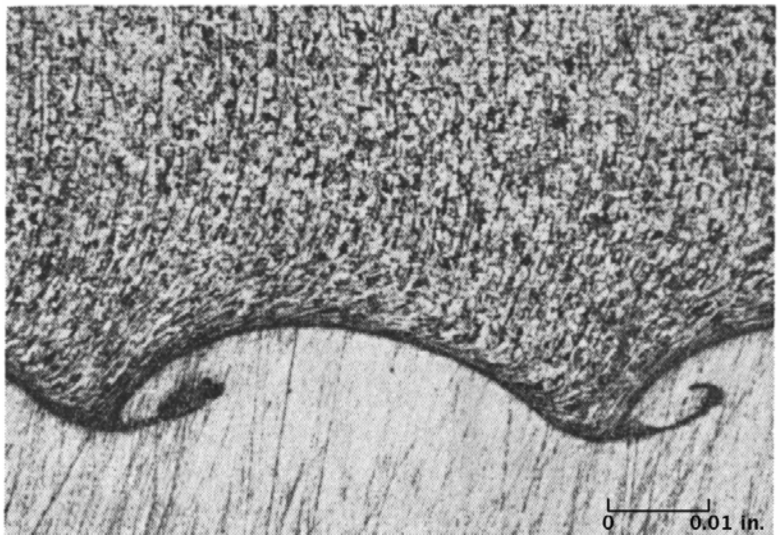

Figure 73: Mild Steel Bullet Joined to a 0.022 inch Thick Copper Target by Impact at an Angle of 30^{o} and Velocity of 2707 ft/sec [187]

Similar features were observed at the up-range, or "nose" end of rod segments bounded by gouges on both ends, as shown in Fig. 74. In such cases, the up range end of the segment would contain the latter half of the preceding gouge, whereas the downrange end of the segment would contain the initiation portion of a subsequent gouge. This was also convenient from a research standpoint, as it allowed the majority of a (composite) gouge to be studied in a single rod segment.

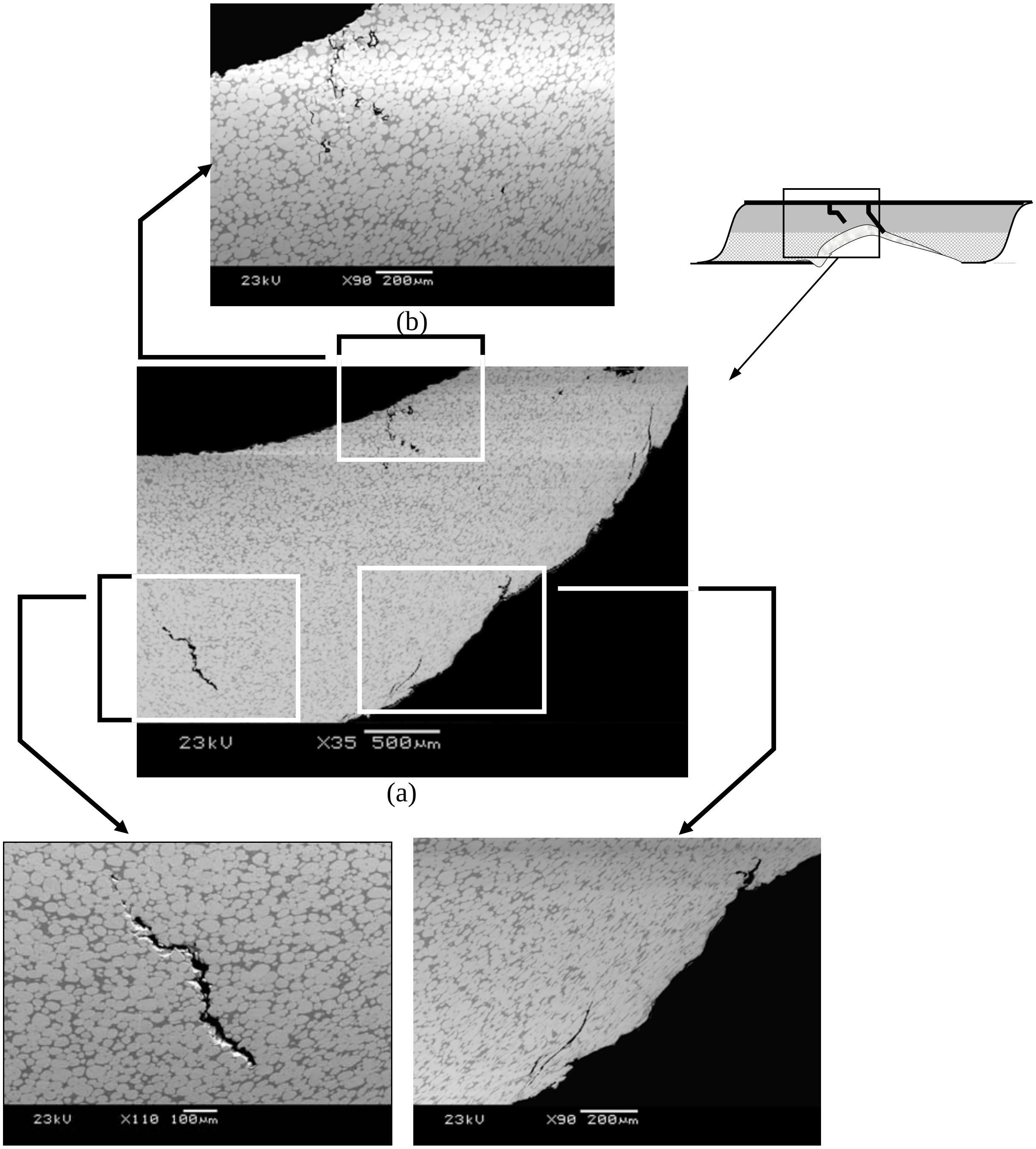

(b)

(a)

(c) (d)

Figure 74: (a) Shot # 779 - EP WNiCo Reverse Ballistic Specimen Reflecting Gouge Tail Portion at Nose End of Rod Segment with: (b) Tensile Surface Fracture Damage; (c) Internally Nucleated Fracture; and (d) Contact Surface-Initiated “Rearward” Running Fractures (← Projectile Travel)

From Fig. 74, gouge-induced rod failure appears to initiate at a rod's tensile and compressive surfaces, and possible internally. These fractures grow and link primarily via W grain cleavage. The images also provide evidence of the origins of axial splitting, observed in these experiments to be associated with gouging.

6.3.7 Fracture Surfaces

As with the drop tower specimens, fracture surface micrographs from reverse ballistic specimens reveal morphologies dominated by W grain cleavage, but with the other failure modes (W-W grain boundary failure, W-matrix separation, and matrix failure) modes present, as shown in Fig. 75. Directional fracture mapping was applied to representative EDM and CG-SP-EP fracture surface micrographs taken near fracture initiation, in the mid-section, and at the compressive surfaces, respectively, shown in Fig. 76. The resultant directions indicate fractures running generally toward the compressive surface. The lone exception is the EDM WNiFe midsection, in which the micrograph's resultant fracture direction indicates a crack front propagating toward the tensile surface.

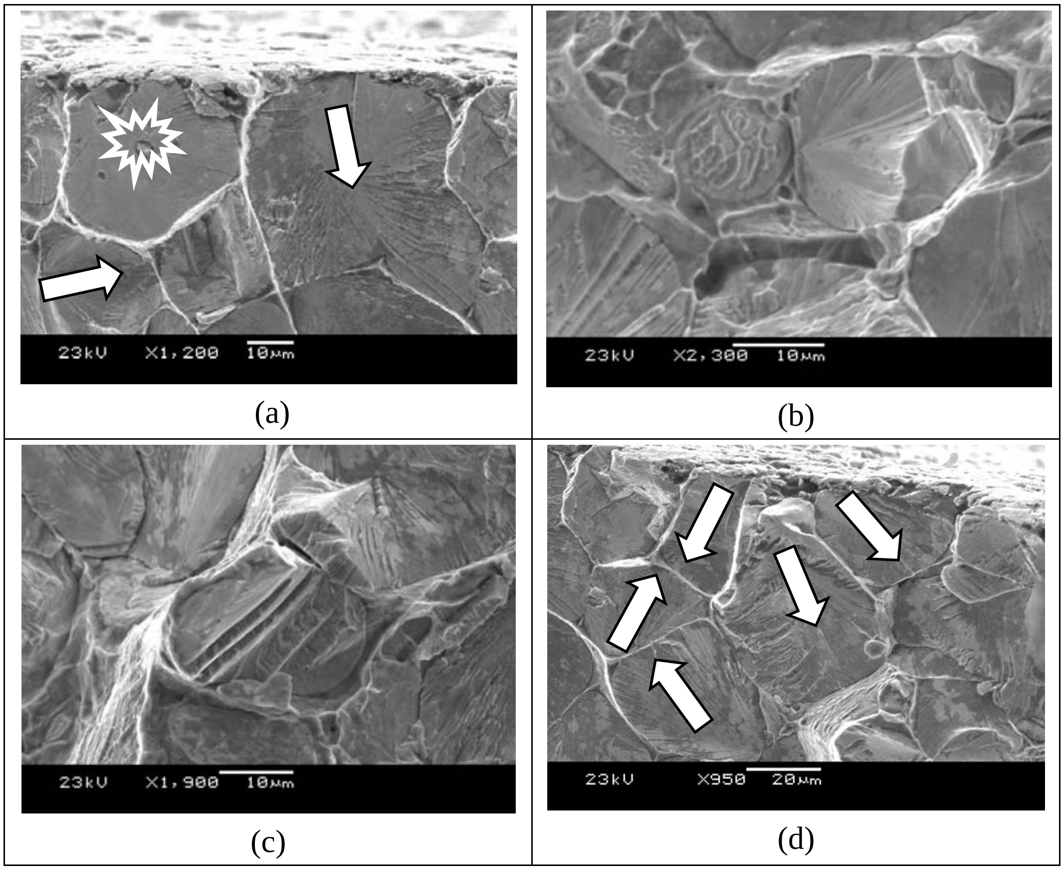

(a) (b)

(c) (d)

Figure 75: Shot # 717 - EDM WNiFe Reverse Ballistic Fracture Surface Features - (a) Internally Nucleated (Due to Porosity) and Surface Initiated W Grain Cleavage Near Site of Fracture Initiation; (b) Matrix Pullout on W-W Grain Separation and W Grain Cleavage; (c) Steps Resulting from W Grain Cleavage on Orthogonal Planes; and (d) Discrete Fracture Initiation Site at W-W Grain Contiguity Near Site of Fracture Initiation

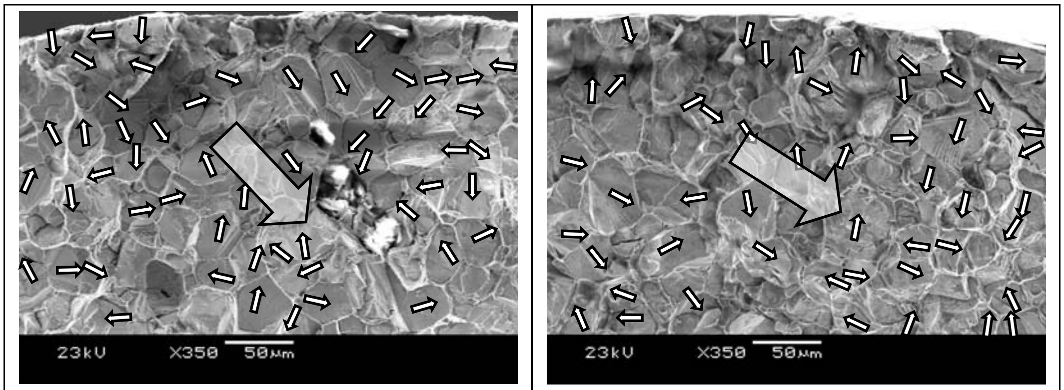

(a) Shot #767 - EDM Tensile Surface

(b) Shot #765 - CG-SP-EP Tensile Surface

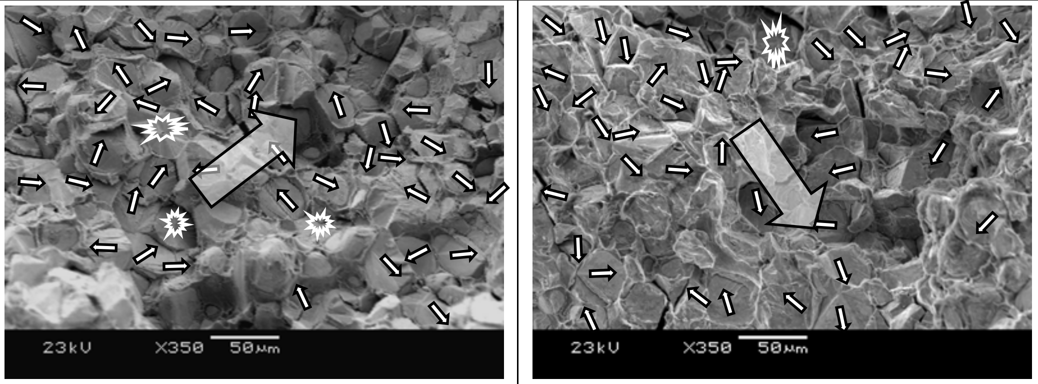

(c) Shot #767 - EDM Mid-Section

(d) Shot #765 - CG-SP-EP Mid-Section

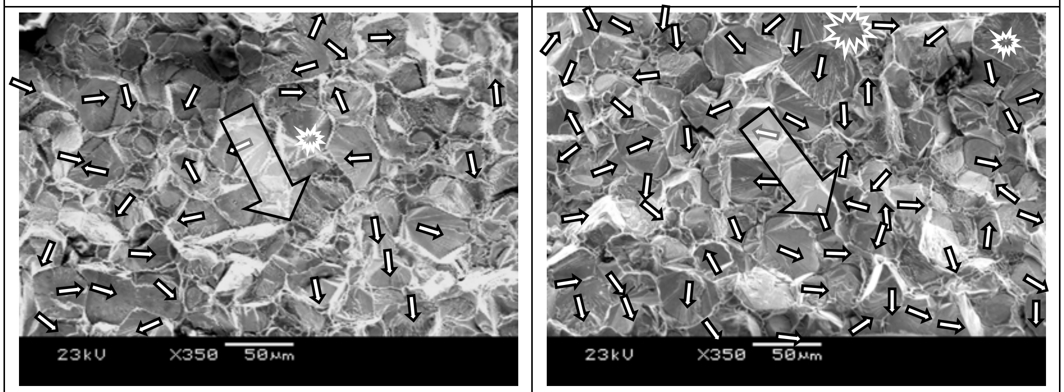

(e) Shot #767 - EDM Near Compressive Surface

(f) Shot #765 - CG-SP-EP Near Compressive Surface

Figure 76: WNiFe Reverse Ballistic Specimen Fracture Surfaces and Directional Mapping

6.4 CTH MODELING

The dynamics of rod-projectile interaction are difficult to deduce from the flash X-ray photographs for each event, particularly without foreknowledge of where the rods break. As previously discussed, numerical simulations, such as CTH, do not presently have the ability to capture the full physics involved in these types of interactions. However, they can provide information on the loading conditions present up to the point of experimentally observed fracture. Three-dimensional CTH simulations were conducted in support of this research effort to model reverse ballistic experiments [188]. The interaction of shot #717 – EDM WNiFe, simulated at a velocity of 2.2 km/s, was used as a baseline to determine the qualitative accuracy of the model. Once this was established, the model was modified to determine the effects of increased velocity and an altered surface profile.

The CTH model frame of shot #717, shown in Fig. 77, appears remarkably similar to the X-ray image for the same shot and provides a wealth of information about conditions at the time of failure that is otherwise unknown.

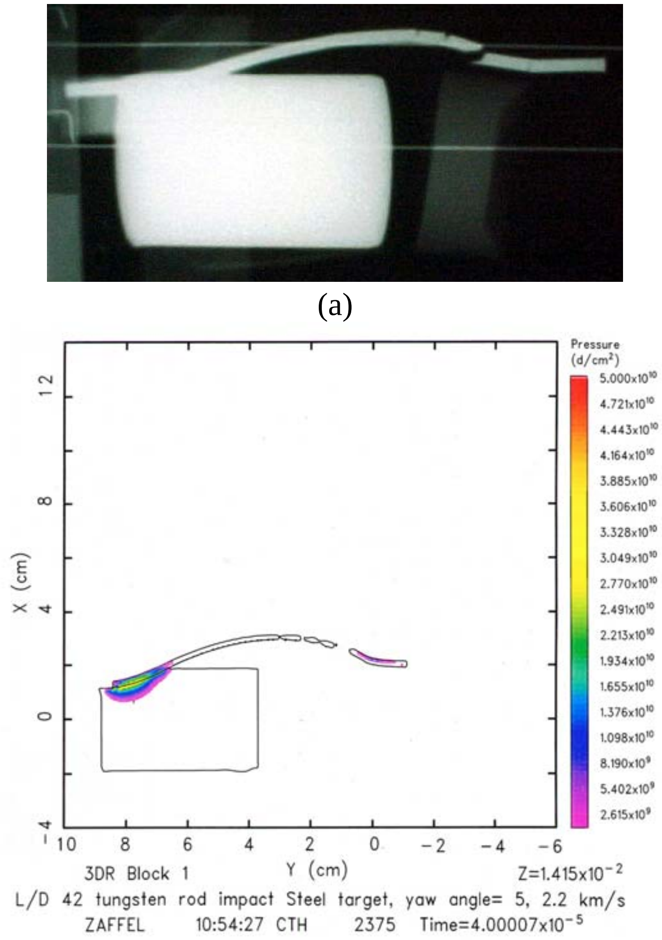

(a)

(b)

Figure 77: Shot #717 – EDM WNiFe: (a) Flash X-Ray Photograph; (b) Frame from CTH Model [181]

The model results indicate that the contact surface mean pressure is in excess of 3.0 x 10^{10} dynes (3,000 MPa), which is significantly more than the compressive yield stresses of either WHA or the RHA considered in this work (approximately 2,000 MPa at 15% strain for WNiFe and WNiCo, and 1,600 MPa for RHA [178]); the hydrostatic stress is:

$$\frac{\sigma_x + \sigma_y + \sigma_z}{3} \tag{6.2}$$

where σ_x = x-direction stress

σ_y = y-direction stress

σ_z = z-direction stress

Upon more detailed examination, however, the CTH model is found to predict rod failure resulting from the localization of plastic flow rather than brittle fracture. The lack of an accurate material model for dynamic fracture, again one of the motivations for this work, prevents the CTH model from accurately predicting specimen failure. Additionally, the lone WHA constitutive model available in CTH prevents the model from distinguishing between WNiFe and WNiCo, when there are clearly differences in their behaviors. CTH also lacks the fidelity to distinguish between microscopic surface roughness differences and initial flaw sizes.

Both the flash X-ray photograph and CTH model indicate that rod fracture is not instantaneous, but rather a latent event occurring some time after rod-projectile contact has ceased. In contrast, debris plumes captured in the X-rays from other shots indicate that gouging is fairly instantaneous, occurring directly in conjunction with rod-projectile contact. This sheds further light on why surface-improved rods tend to gouge. If the contact velocity is greater than the gouging threshold velocity and the contact pressure is sufficient to yield both surfaces involved, then instantaneous gouging would be expected in advance of bending-induced Mode I rod failure.

Based upon the remarkable experimental results with surface-improved rods at velocities above 2.4 km/s, the CTH model was rerun at both 2.3 km/s and 2.6 km/s with artificial surface “roughening,” the closest approximation presently possible for capturing micrometer scale surface finish variations. Sine wave-shaped “asperities” were placed along the rod exterior, such that volumes of material were removed from below the rod surface and placed on the surface while maintaining constant rod mass and volume. The dimensions of these asperities were limited to some multiple of the model’s mesh cell dimension of 0.3 mm x 0.3 mm x 0.3 mm. They were chosen to be two cells long, or 0.6 mm, and placed 0.6 mm apart for a total of ninety grooves on a 108 mm long rod. Asperity depths of one, two and three cells were considered, resulting in “initial flaw” sizes of 330 μm, 660 μm, and 990 μm, respectively. In comparison, an EDM WNiFe rod, as was used in shot #717, is estimated to have an 18 μm average initial surface flaw size.

In agreement with the experimental findings in this work, the CTH model results indicate a subtle but discernible behavior difference to surface roughening. This was particularly true at 2.6 km/s with a two-cell asperity depth, where lower peak stresses and reduced stress localization led to less, or at least delayed, rod damage, as shown in Fig. 78. This is analogous to the segmenting of rods due to bend-induced fracture as observed experimentally, which occurs after rod-projectile contact has passed. In contrast, no surface roughening led to stress localization, which seems analogous to gouging.

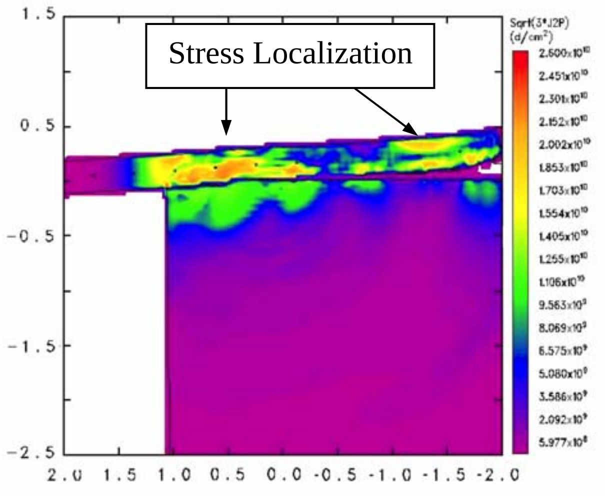

(a) Without Surface Roughening

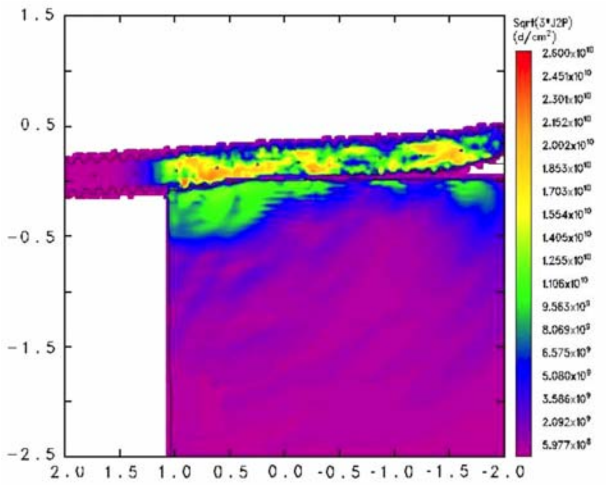

(b) With Surface Roughening

Figure 78: CTH Frames of a 2.6 km/s Reverse Ballistic Impact [188]

Chapter 7: Discussion

7.1 SYNOPSIS OF WORK

The purpose of this experimental investigation was to characterize the dynamic WHA failure process as a function of surface condition under generic transverse loading conditions. Primary research objectives were to: 1) characterize WHA damage at different, high strain rates; 2) quantify the effect of surface condition on damage initiation, accumulation, and the dynamic failure of WHA; and 3) quantify the effect of microstructure on the same. Accordingly, a WNiFe alloy and a WNiCo alloy were subjected to transverse loading-induced failure at dynamic ($\sim 10^3$/s) and ballistic impact ($\sim 10^5$/s) strain rates. Their behaviors and sensitivity to surface finish changes were investigated through experimental observation and data analysis, and by recovered specimen micrographic and metallographic observation. Though differences were noted in composition, microstructure, and fundamental behavior, with one alloy exhibiting significantly more room temperature ductility and toughness than the other, both alloys considered were found to exhibit significant sensitivity to surface finish enhancement. In the extreme case for room temperature drop tower testing, the more brittle of the two alloys (WNiFe) behavior was improved by surface finish improvement to the extent that the majority of samples tested did not break. In reverse ballistic testing, surface finish improvement induced a change in failure mode from primarily segmenting via bend-induced fracture to that of rod fragmentation caused by hypervelocity gouging. In the extreme cases here, rod failure was equally catastrophic regardless of alloy in that rods of both alloys were no longer distinguishable by their behavior and the average size of recovered fragments.

Results from both sets of tests showed a significant improvement in alloy performance with surface finish enhancement. For drop tower testing, this was observed as an increase in strain prior to failure and specific fracture energy with decreasing initial flaw size. In the case of reverse ballistic testing, the slot cutting efficiency of both alloys improved with initial flaw size reduction, notwithstanding the fact that rod failure became more catastrophic.

Micrographic and metallographic analysis revealed that initial sample preparation by EDM-induced surface W grain microcracking, while subsequent surface finishing mitigated this damage. The most beneficial finishes were those that completely eliminated preexisting microcracks. Tensile surface damage accumulation and final failure characteristics were found to be consistent across both testing means and alloys. Failure behavior was dominated by W grain cleavage, with incipient surface fractures becoming most numerous and severe immediately adjacent to final fracture. For EDM samples with the largest preexisting microcracks, fracture occurred exclusively by the opening, growth, and coalescence of these surface flaws. With surface finish improvement, damage initiation primarily in the form of W grain cleavage with limited W-W separation began in the interior of specimens. For CG-SP-EP samples in both drop tower testing and reverse ballistic testing, damage nucleation was observed to be almost exclusively internal and exhibited a close competition between W cleavage and contiguous W grain separation as failure initiation modes. The evaluation of river lines and cleavage steps on the surfaces of cleaved W grains showed that fracture progresses most rapidly along favorable axes, typically via cleavage of contiguous W grains. The crack front initially bypasses more fracture resistant regions of the microstructure, frequently resulting in subsequent local propagation opposed to the overall crack front propagation direction. A collective evaluation of a statistically significant number of these features was shown to accurately indicate the overall fracture propagation direction by generating "fracture maps".

By comparing flash X-ray photographs with reverse ballistic rod fragments recovered through a newly developed technique, catastrophic rod failure was found to be due to hypervelocity gouging. Micrographic analysis of gouged segments revealed unusual and extreme grain distortion, indicative of jet formation and surface strains in excess of 100%, as well as other atypical failure features. These included fractures initiating at compressive (contact) surfaces and propagating toward the tensile surfaces, usually opposed to the direction of sliding contact. Other fractures initiated at the ends of segments and ran axially, confirming the apparent "axially splitting" sometimes indicated by flash X-ray photographs and recovered rod fragments.

The results of numerical modeling conducted in support of this work appear to be in agreement with reverse ballistic experimental results. Rods with artificial surface roughening experience less stress localization and lower peak stresses, resulting in delayed, if not less, overall rod damage.

7.2 ORIGINAL CONTRIBUTIONS

The following accomplishments during the course of this work represent new contributions to the understanding of dynamic WHA failure:

1) Conducting a direct comparison of the dynamic failure behavior of two WHA's subjected to transverse loading.
2) The identification of WHA fracture initiation microprocesses.
3) The determination that surface finish has a significant influence upon the manner in which WHA damage initiates, accumulates, and leads to dynamic failure.
4) The identification of the detrimental effects of EDM on WHA.
5) Use of fracture surface mapping to determine WHA crack propagation directions.

6) The use of reverse ballistic testing specifically to induce transverse-loading WHA rod failure.
7) The determination that dynamic transverse loading WHA failure behavior at moderate (drop tower) strains rates is indicative of high (reverse-ballistic) rate failure behavior.
8) The identification of hypervelocity microgouges through flash X-ray photographs in combination with recovered rod fragments.
9) The development of a technique for the recovery of reverse-ballistically generated WHA rod segments and/or fragments in a condition conducive to further (metallographic) analysis.
10) The establishment of a ballistic slot cutting efficiency parameter.

7.3 SIGNIFICANT FINDINGS

Significant findings pertaining to the elevated strain rate failure behavior of WHA during the course of this experimental study include the following:

1) W grain cleavage was the dominant failure mode for both alloys considered.
    a. W cleavage and contiguous W grain separation are WHA fracture initiation modes.
    b. WHA fracture progresses most rapidly along axes populated by contiguous W grains.
    c. W grain – matrix separation and matrix failure are fracture coalescence modes.
    d. W grain porosity, at the small levels present in the two alloys studied, contributes to but does not alter the fundamental failure behavior of these alloys.

    e. River markings and steps on the face of cleaved W grains can be used *a posteriori* to deduce local and global fracture propagation directions.

2) WHA dynamic failure behavior is greatly influenced by the size and nature of preexisting surface flaws.
    a. EDM induces W grain microcracking on the surface of a work piece.
    b. Any surface treatment causing a reduction in the size of these preexisting flaws will improve the alloy's dynamic behavior.
    c. Increasing removal of surface material from EDM rods by any of the evaluated means will provide an increasing improvement in dynamic WHA behavior.
    d. The most significant improvements in dynamic WHA behavior are obtained by removing enough material so that preexisting surface microcracks are eliminated.
    e. EP preferentially attacks the matrix phase of WHA. Notwithstanding, it provides a tangible improvement in dynamic WHA behavior beyond that which can be quantified by the amount of surface material removed or average surface roughness (Ra).
3) Hypervelocity transverse-loading contact by Lexan™ alone can induce EDM WHA rod failure.
4) Surface finish enhancements increase the propensity of WHA rods to gouge and fail catastrophically due to fragmentation, but also improve their performance.
    a. Other than at initial contact, WHA rod gouging does not occur below the apparent gouging threshold velocity of approximately 2.4 km/s, revealing a failure mode "velocity effect." Rod failure below this threshold is due to fracture-induced segmentation.

    b. Gouging may or may not occur above the threshold velocity.
    c. Only rods with improved surfaces gouged above the threshold velocity, revealing a failure mode “surface finish effect.”
    d. Severe hypervelocity gouging of WHA rods, as occurred in this work, always leads to catastrophic rod failure.
    e. Microgouging is possible and may precede macro gouging.
    f. Surface finish enhancement increases the slot cutting efficiency of WHA rods.
5) Dynamic WHA three point bend test behavior is indicative of ballistic strain rate behavior.
    a. Overall comparative alloy behavior, more brittle in the case of WNiFe and more ductile in the case of WNiCo, held true at both strain rates.
    b. Surface finish enhancements provided a marked improvement in rod performance at both strain rates.
    c. Brittle fracture surfaces generated at both strain rates bear similar features.

These findings represent foundational knowledge critical to the development a fracture criterion for the numerical codes used to predict the dynamic behavior of WHA’s and other materials.

7.4 INSIGHTS

7.4.1 The Nature of WHA Failure

Observations in this work indicate that fracture initiation in WHA is controlled by the W phase, but both the W and matrix phases participate in the failure process. As alloy failure occurs, the matrix can work harden without causing cracking in the alloy, and if the W grains cleave, the cracks can be stopped by the enveloping phase. This has been identified in the literature [189] and was observed to be true in this work, even when numerous "brittle" (W grain cleavage and contiguous grain separation) fracture initiation sites existed. Final WHA failure is ultimately controlled by the matrix, as evidenced by ductile matrix dimpling visible in fracture surface micrographs.

Discussions in literature describing microscopic and macroscopic WHA failure as "ductile" or "brittle" are confusing, inconsistent, and often misleading. W grain cleavage is by definition a distinctly brittle failure mode, whether or not it occurs in an alloy that experiences macroscopic ductility prior to failure. As was observed in this work, W grain cleavage was prevalent in microstructures regardless of the amount of ductility demonstrated. The same is true of W-W grain boundary failure. Conversely, matrix failure is a ductile failure mode regardless of macroscopic failure behavior. It can be said, then, that the WHA rod failures observed in this work were brittle events, but the fracture surface morphologies were indicative of both brittle and ductile failure modes.

7.4.2 Improving the Behavior of WHA

One of the initial thrusts of this work was an evaluation of the influence of surface roughness on dynamic WHA behavior. Once the detrimental effects of EDM were identified, it was apparent that two versions of the initial approach were to be pursued. The first, involving the EDM, SP, and EP rods, was an investigation of varied average initial flaw sizes on dynamic WHA behavior. The other, involving CG and CG-SP-EP rods, was more in keeping with the original objective and entailed contrasting the influence of two surfaces finishes with no preexisting surface W grain microcracks.

As is indicated in the literature and has been shown in this work, surface initiation controls WHA failure unless specimen surface finish causes the surface to become resistant to fracture initiation, forcing internal failure nucleation to dominate the fracture process. Reducing the measured average initial flaw size from EDM to SP to EP improved WHA rod performance in drop tower testing and was demonstrated to be one way of bring about a transition to internal fracture nucleation. Another was the surface finish enhancement rendered by going from CG and CG-SP-EP, even though rods treated by these processes returned almost the same average (Ra) and root mean square (Rq) roughness measurements, depending upon the cutoff length considered. To wit, CG-SP-EP WNiFe rods usually did not break in drop tower testing and required greater specific fracture energy to fail than rods with any other surface finish evaluated. The specific fracture initiation, propagation, and total fracture energies of CG-SP-EP rods were also unsurpassed, exceeding those of CG rods by 34%, 88%, and 53%, respectively.

Collectively, this suggests that fracture mechanics considerations controlled the failure behavior of rods with EDM, SP, and EP surface finishes, whereas intrinsic properties may control the failure of CG & CG-SP-EP rods. If dynamic ductility and resistance to fracture are the measures, the best possible WHA behavior appears to be obtained by eliminating measurable surface flaws, ensuring a profilometrically smooth surface, and avoiding pre-stressing / straining (and likely strain-hardening, leading to increased brittleness) of the specimen surface in the process of obtaining a smooth surface. This only seems possible using EP as the final surface-finishing step.

It is well documented that EP greatly enhances the ductility of pure single and polycrystalline W. As a result of this present effort, it is also clear that the same holds true for WHA and at high strain rates, despite EP preferentially attacking the matrix phase and leaving surface W grains as “raised islands,” as noted in Section 4.3.3. Though beyond the scope of this work, the benefits of EP likely stem from the competition between dislocation nucleation and mobility at an advancing crack tip. As EP is known to effectively reduce the dislocation density at the surface of a sample and

CG effectively increases the same due to inducing surface strains during the process of removing material, EP can be viewed as raising the DBTT or ductile-to-brittle transition strain rate, resulting in increased ductility for a given strain rate and temperature.

7.4.3 On the Catastrophic Failure of Surface-Improved WHA Rods During Reverse Ballistic Testing

Under the conditions of hypervelocity impact, fracture and gouging appear to be competing failure modes. Gouging, if present, suppresses fracture. Despite their fundamental differences, both WNiFe and WNiCo were shown to selectively gouge dependant upon surface treatment and reverse ballistic test conditions. Below the apparent threshold velocity of 2.4 km/s, no gouging subsequent to initial target rod impact was observed. Above the threshold velocity, only EDM rods did not gouge, whereas all other alloy and surface finish combinations routinely gouged. In addition, with surface finish improvement leading to a reduction in the average initial flaw size, gouge propensity and slot cutting efficiency both increased. Collectively, this suggests that the dynamic loading required for rod gouging is comparable to but greater than that leading to fracture, and that gouging precedes fracture when the conditions for gouging are present. It also suggests that given a sufficiently large initial flaw size, gouging will not occur due to the critical stress intensity factor and thus failure (fracture) stress being reached prior to that required for gouging. Catastrophic WHA rod failure by gouge-induced fragmentation, then, is indicative of performance superior to failure by fracture-induced rod segmentation.

This is reasonable due to a number of factors. First, the tensile and compressive flow stresses of WHA have both been shown to increase with strain rate, suggesting that strain rate strengthening would offset any tendency to prematurely fracture at high strain rates. Second, the velocity of fracture propagation in a brittle material is limited theoretically by the material's Rayleigh wave speed, c_R, but is known in reality to be some fraction thereof, typically half. Using representative dilatational and shear wave speeds, which are comparable for the alloys considered [163], c_R can be determined from [190]:

$$\frac{c_1}{c_2} = \left(\frac{2-2\nu}{1-2\nu}\right)^{\frac{1}{2}} \tag{7.1}$$

$$\frac{c_R}{c_2} = \frac{(0.87+1.12\nu)}{(1+\nu)} \tag{7.2}$$

where c_1 = dilatational wave speed (~5180 m/s)

c_2 = shear wave speed (~2830 m/s)

ν = Poissons ratio = 0.29

and $c_R \cong$ 2620 m/s

Assuming the maximum possible crack tip speed to be half of c_R, or 1310 m/s, reveals that the sliding interaction velocity and, thus, the gouging velocity (~2.4 km/s), was always greater than c_R in these experiments. Thus, if gouging was possible, it would always occur more quickly than fractures could run. In this light, it is logical to conclude that, conditions permitting, gouging preempts fracture. Because the average initial flaw size was the independent variable in these experiments, one can envision a flaw-size dependent failure mode change, or crossover, from fracture to gouging, as suggested by Fig. 79.

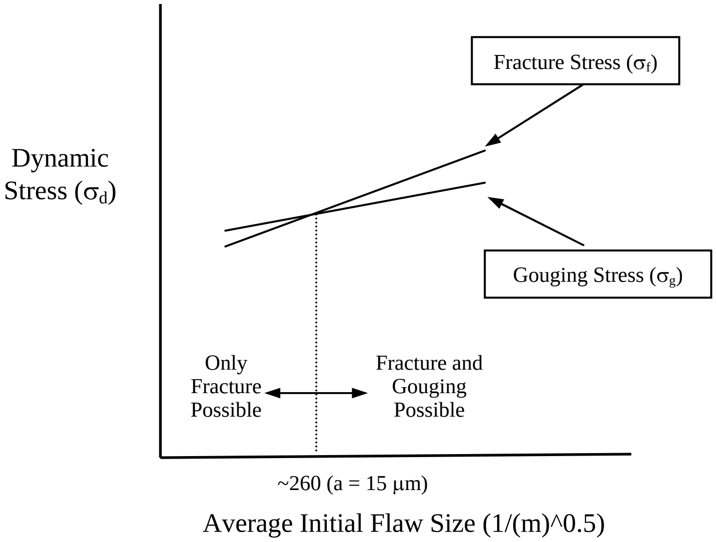

Figure 79: Speculative WHA Fracture and Gouging Stress Crossover Occurring Above the Gouging Threshold Velocity

It is also possible that gouging did not occur on EDM rods because the W-Cu surface layer resulting from the EDM process provided melt-lubrication during sliding contact. This does not seem likely, though, for a number of reasons. Among them, rough surfaces have been shown to be more prone to gouging than smooth surfaces, and harder surfaces with greater yield strengths have been more resistant to gouging than softer, weaker surfaces. The latter is in keeping with the fact that the yielding of both surfaces in contact is required for gouging to occur. Additionally, Cu is known to be prone to gouging. Finally, as the EDM surface layer failed to prevent initial impact gouges from occurring, it is unlikely that it would be able to prevent subsequent gouging due to sliding contact.

7.5 RECOMMENDATIONS FOR FUTURE WORK

Many unresolved issues pertaining to understanding, predicting, and modeling dynamic transverse loading WHA failure remain. Among them are the following.

1) EDM has been shown to have a detrimental effect on WHA by inducing surface microcracking of W grains. It is not known if this is an inherent problem of the EDM process, or rather an artifact of the specific (W-carbide) settings used to prepare samples in this work. An important contribution to the understanding of this effect would be a parameter study to determine the sensitivity of W grain microcracking to the EDM settings used, and whether or not microcracking can be eliminated with the use of different settings.
2) One of motivations for this effort was the fact that the numerical simulations used to predict high-rate WHA failure are only accurate up to the point of fracture initiation. As a result of findings in this work, CTH has already demonstrated sensitivity to surface roughening despite still lacking a useful fracture criterion. However, until brittle failure behavior can be properly modeled, accurately predicting the full physics of experimentally observed failures will remain elusive. A starting point in this endeavor would be increasing the model's mesh number to more accurately reflect the polycrystalline nature of WHA, then assigning varying strength properties to cells so that the microstructure does not behave uniformly. The mesh used in modeling conducted in support of this work contained only ten cells across a rod diameter, whereas an actual microstructure might contain two orders of magnitude more W grains over the same dimension.
3) The detrimental effects of EDM upon WHA, the SP-only and EP-only finishes did not receive a fair evaluation as considered due to preexisting flaws. As

indicated by the responses of CG and CG-SP-EP specimens to testing, surface finish and/or intrinsic properties that may be induced by surface finishing are important factors in dynamic WHA failure behavior. All require further evaluation on WHA specimens without preexisting microcracks to isolate the true influence of the finishes alone. Other common finishing approaches, such as turning, should also be considered.

4) Because the removal of surface flaws has been shown to dramatically improve the high-rate performance of WHA, particularly with EP as a final step, it is conceivable that a reverse process might be equally effective at improving WHA surfaces by effectively "healing" them. Specifically, the notion of electroplating WHA with a W alloy to add a dislocation free surface layer is intriguing. Typical W contents of plated alloys range from 5 to 15 atomic percent (~15 to 35 wt. %), which seem too low to be of interest. However, electroplating of amorphous W-Ni alloys with W contents as high as 50 atomic percent (76 weight percent) has been demonstrated, and similar approaches have been developed for W-Co alloys [191,192]. Either these or yet to be developed plating approaches for higher W content alloys may be of benefit to WHA.

5) The K_{ID} of WHA was addressed only in a limited fashion in this work but is of great importance in the development of accurate fracture models. Specifically, its rate and alloy dependence requires greater understanding and must be incorporated into the numerical models. Accordingly, both quasistatic and dynamic fracture toughness testing should be conducted on the alloys considered in this work.

Chapter 8: Conclusion

In this experimental investigation, a broad understanding of the high-rate transverse-loading fracture behavior of WHA has been developed. Dynamic fracture events spanning a range of strain rates and loading conditions were created via mechanical testing and used to determine the influence of surface condition and microstructure on dynamic damage initiation, accumulation, and sample failure under different loading conditions. At two different dynamic strain rates, the failure initiation mode was changed from primarily external (at the surface) to primarily internal nucleation as surface condition was improved by diminishing the size of preexisting flaws until they were eliminated. This led to greatly enhanced performance in three-point bend testing and the onset of hypervelocity gouging during reverse ballistic testing. Fracture surface analysis revealed W grain cleavage to be the dominant failure mode, that fractures propagated similarly regardless of where they initiated, and that the global fracture propagation direction could be determined *a posteriori* using visual evidence.

These results are significant for a number of reasons. First, they shed important light on a category of particulate composites widely used in present defense applications as kinetic energy penetrators. For this reason alone, their influence may be far reaching. Next, they characterize the manner in which WHA damage initiates, accumulates, and leads to failure under the conditions of dynamic transverse loading. This is a practical problem whose understanding was vague prior to this work. Further, they highlight the sensitivity of WHA to parameters critical to the development of useful dynamic WHA fracture criterion, but on a scale that cannot yet be addressed with current model fidelity. In so doing, they underscore focus areas for numerical code improvement. Additionally, they reveal gouging to be a potentially negative side effect of hypervelocity sliding on improved surfaces. This foreshadows that the stronger, smoother surfaces seen as a panacea to eliminating gouging may not provide a final solution to the problem. Finally, they prove that moderate dynamic strain rate WHA results are indicative of higher strain rate behavior.

Appendix: Reverse Ballistic Shot Matrix

Shot #	Date	Rod				Launch Package		Primary Failure Type[1]	Calculated Slot Cutting Eff., E_s
		W Alloy	Surface Finish	Initial Mass (g)	Rec'd Mass (g)	Mass (g)	Vel. (km/s)		
717	1/27/03	Fe	EDM[2]	13.90	11.75	419.8	2.30	Seg.	-
718	1/29/03	Fe	EDM	13.90	13.17	419.7	2.23	Seg.	-
719	2/4/03	Co	F/NP[3]	13.29	12.67	419.7	2.25	Seg.	-
729	3/20/03	Co	F/NP[3,4]	13.19	11.11	419.0	2.45	Seg.	-
732	4/7/03	Fe	EDM[5]	13.99	11.54	404.0[6]	2.37	Seg.	-
749	6/17/03	Co	EDM	13.81	11.95	370.0	2.55	Seg.	0.38
751	6/24/03	Co	EDM	13.73	10.75	370.0	2.55	Seg.	0.26
756	7/16/03	Fe	SP	13.81	11.95	370.0	2.25	Seg.	0.48
757	7/18/03	Fe	SP	13.70	8.32	370.0	2.40	Frag.	0.56
762	8/12/03	Fe	SP	13.83	9.36	370.0	2.60	Frag.	0.96
763	8/14/03	Fe	CG	11.20	8.01	370.0	2.55	Mixed	0.65
764	8/19/03	Fe	CG	11.38	8.05	369.0	2.46	Mixed	1.04
765	8/21/03	Fe	CG-SP-EP	10.71	7.25	370.0	2.52	Mixed	0.56
766	8/26/03	Fe	CG-SP-EP	11.31	8.55	369.0	2.48	Mixed	0.92
767	8/28/03	Fe	EDM	13.94	11.49		2.46	Seg.	0.33
768	9/2/03	Co	CG	11.38	7.46		2.48	Mixed	0.58
776	10/2/03	Co	CG	11.46	7.75	369.8	2.50	Mixed	0.67
777	10/7/03	Co	CG-SP-EP	11.48	7.13	369.4	2.55	Frag.	0.69
778	10/9/03	Co	CG-SP-EP	11.44	6.39	370.9	2.46	Frag.	0.77
779	10/14/03	Co	EP	13.90	8.31	369.7	2.57	Frag.	0.63
780	10/16/03	Co	SP	14.22	10.02	369.9	2.47	Mixed	0.60
781	10/21/03	Co	SP	13.94	8.88	369.9	2.57	Mixed	0.60
782	10/23/03	Fe	EP	13.45	8.85	369.7	2.57	Mixed	0.64

Notes:

1) Rod failures were categorized as fracture-induced segmentation., gouged-induced fragmentation, or both (mixed).
2) Only shot with 3.5 degree rod pitch; all shots other than 717, 729, & 732 were conducted with 5.5 ± 0.5 degree rod pitch.
3) F/NP = As EDM rod mounted in lathe, filed, then shined with an abrasive nylon pad. Rods of this finish were used during two diagnostic reverse ballistic shots only, and were not considered in any other testing.
4) Only shot with 10.0 degree rod pitch; all shots other than 717, 729, & 732 were conducted with 5.5 ± 0.5 degree rod pitch.
5) Only shot with 7.0 degree rod pitch; all shots other than 717, 729, & 732 were conducted with 5.5 ± 0.5 degree rod pitch.
6) Only shot with Lexan™ launch package.

References

[1] E. Lassner and W.-D. Schubert, Tungsten: Properties, Chemistry, Technology of the Element, Alloys, and Chemical Compounds, Kluver Academic/Plenum Publishers, New York, Boston, Dordrecht, London, 1999, pp. 77-80.

[2] L. Ekbom, “Microstructural Study of the Deformation and Fracture Behavior of a Sintered Tungsten-Base Composite,” *Modern Developments in Powder Metallurgy*, Volume 14 (1981), *Proceedings of the 1980 International Powder Metallurgy Conference for Special Materials*, Washington, DC, USA, pp. 177-188.

[3] A. Bose and R.J. Dowding, “Processing and Alloying of Tungsten Heavy Alloys,” *Advanced Composites '93*, International Conference on Advanced Composite Materials, edited by T. Chandra and A.K. Dhinga, The Minerals, Metals, & Materials Society, 1993, pp. 1279-1285.

[4] Y.H. Chiou, Y.S. Zu, and S.T. Lin, “Partition of Tungsten in the Matrix Phase for Liquid Phase Sintered 93%W-4.9%Ni-2.1%Fe,” Scripta Materiala, Volume 34 (1996), pp. 135-140.

[5] Y.H. Chiou, Y.S. Zu, and S.T. Lin, “Structural Evolution of Matrix Phase for Liquid Phase Sintered 93W-4.9Ni-2.1Fe,” *Journal of Materials Science Letters*, Volume 31 (1996) pp. 4039-4046.

[6] A. Upadhyaya, “Processing Strategy for Consolidating Tungsten Heavy Alloys for Ordnance Applications,” *Materials Chemistry and Physics*, Volume 67 (2001), pp. 101-110.

[7] Binary Alloy Phase Diagrams, 2nd Edition, editor-in-chief, T.B. Massalski, editors, H. Okamoto, P.R. Subramanian, L. Kacprzak, ASM International, Materials Park, Ohio, 1990, pp. 1258, 1792.

[8] R.M. German, J.E. Hanafee, and S.L.T. DiGiallonardo, “Toughness Variation with Test Temperature and Cooling Rate for Liquid Phase Sintered W-3.5Ni-1.5Fe,” *Metallurgical Transactions A*, Volume 15 (1984), pp. 121-128.

[9] R.M. German and K.S. Churn, “Sintering Atmosphere Effects on the Ductility of W-Ni-Fe Heavy Metals,” *Metallurgical Transactions A*, Volume 19 (1984), pp. 747-754.

[10] R.M. German, L.L. Bourguignon, and B.H. Rabin, "Microstructure Limitations of High Tungsten Content Heavy Alloys," *Journal of Metals*, Volume 37 (1985), pp. 36-39.

[11] B.H. Rabin, "Microstructure and Tensile Properties of Liquid Phase Sintered Tungsten-Nickel-Iron," PhD Thesis, Rensselaer Polytechnic Institute, Troy, NY 1986.

[12] B.H. Rabin and R.M. German, "Microstructure Effects on Tensile Properties of Tungsten-Nickel-Iron Composites," *Metallurgical Transactions A*, Volume 19 (1988), pp. 1523-1532.

[13] L.L. Bourguignon and R.M. German, "Sintering Temperature Effects on a Tungsten Heavy Alloy," *The International Journal of Powder Metallurgy*, Volume 24 (1988), pp. 115-121.

[14] R.M. German, A. Bose, and S.S. Mani, "Sintering Time and Atmosphere Influences on the Microstructure and Mechanical Properties of Tungsten Heavy Alloys," *Metallurgical Transactions A*, Volume 23 (1992), pp. 211-219.

[15] E. Lassner and W.-D. Schubert, Tungsten: Properties, Chemistry, Technology of the Element, Alloys, and Chemical Compounds, Kluver Academic/Plenum Publishers, New York, Boston, Dordrecht, London, 1999, pp. 20-22, 274.

[16] T.E. Tietz and J.W. Wilson, Behavior and Properties of Refractory Metals, Stanford University Press, Stanford California, 1965, pp. 275-330.

[17] R.H. Krock and L.A. Shepard, "Mechanical Behavior of the Two-Phase Composite, Tungsten-Nickel-Iron, *Transactions of the Metallurgical Society of AIME*, Volume 227 (1963), pp. 1127-34.

[18] D.V. Edmonds and P.N. Jones, "Interfacial Embrittlement in Liquid-Phase Sintered Tungsten Heavy Alloy," *Metallurgical Transactions A*, Volume 10 (1979), pp. 289-295.

[19] R.M. German, J.E. Hanafee, and S.L.T. DiGiallonardo, "Toughness Variation with Test Temperature and Cooling Rate for Liquid Phase Sintered W-3.5Ni-1.5Fe," *Metallurgical Transactions A*, Volume 15 (1984), pp. 121-128.

[20] K.S. Churn and R.M. German, "Fracture Behavior of W-Ni-Fe Heavy Alloys," *Metallurgical Transactions A*, Volume 15 (1984), pp. 331-338.

[21] R.M. German, L.L. Bourguignon, and B.H. Rabin, "Microstructure Limitations of High Tungsten Content Heavy Alloys," *Journal of Metals*, Volume 37 (1985), pp. 36-39.

[22] B.H. Rabin, “Microstructure and Tensile Properties of Liquid Phase Sintered Tungsten-Nickel-Iron,” PhD Thesis, Rensselaer Polytechnic Institute, Troy, NY 1986.

[23] B.H. Rabin and R.M. German, “Microstructure Effects on Tensile Properties of Tungsten-Nickel-Iron Composites. *Metallurgical Transactions A*, Volume 19 (1988), pp. 1523-1532.

[24] L.L. Bourguignon and R.M. German, “Sintering Temperature Effects on a Tungsten Heavy Alloy,” *The International Journal of Powder Metallurgy*, Volume 24 (1988), pp. 115-121.

[25] A. Bose, D. Sims, and R.M. German, “Test Temperature and Strain Rate Effect on the Properties of a Tungsten Heavy Alloy,” *Metallurgical Transactions A*, Volume 19 (1988), pp. 487-493.

[26] R.G. O'Donnell and R.L. Woodward, “The Composition and Temperature Dependence of the Mechanical Properties of Tungsten Alloys,” *Metallurgical Transactions A*, Volume 21 (1990), pp. 744-748.

[27] R.L. Woodward and R.G. O'Donnell, R.G., “Microstructural Influences on the Ductility of Tungsten Alloys,” *Tungsten and Tungsten Alloys - 1992, Proceedings of the first International Conference on Tungsten and Tungsten Alloys*, Metal Powder Industries Federation, edited by A. Bose and R.J. Dowding, McLean, VA, 1992, pp. 389-396.

[28] R.L. Woodward, and R.G. O'Donnell, “Tensile Rupture of Tungsten Alloys by the Cascade of Crack Nucleation Events,” *Journal of Materials Science*, Volume 35 (2000), pp. 4067-4072.

[29] R.G. O'Donnell and R.L. Woodward, “Influence of Temperature on the Fracture of a W-Ni-Fe Alloy,” *Journal of Materials Science*, Volume 35 (2000), pp. 4319-4324.

[30] R. Gero, L. Borukhin, and I. Pikus, “Some Structural Effects of Plastic Deformation on Tungsten Heavy Metal Alloys,” *Materials Science and Engineering A*, Volume 302 (2001) pp. 162-167.

[31] E.S. Chang, D. Zhao, D.A. Koss, and G.T. Gray III, “Evaluation of Deformation and Fracture Behavior of Tungsten Alloys,” *Advances in Powder Metallurgy and Particulate Materials*, Proceedings of the 1994 International Conference & Exhibition on Powder Metallurgy & Particulate Materials. Part 5 (of 7), May 8-11 1994, Volume 5, pp. 303-316.

[32] C. Tang, J. Zhu, and H. Zhou, “Effect of Strain Rate on Ultimate Strength and Fractograph in Tungsten,” *Rare Metals*, Volume 17 (1998), pp. 198-202.

[33] D.K. Kim, S. Lee, and H.S. Song, "Effect of Size and Shape of Tungsten Particles on Dynamic Torsional Properties in Tungsten Heavy Alloys," *Metallurgical Transactions A*, Volume 30 (1999), pp. 1261-1273.

[34] K.S. Churn, J.W. Noh, H.S. Song, E.P. Kim, S. Lee, and W.H. Baek, "The Effect of Contiguity on the Mechanical Properties of 93W-5.6Ni-1.4Fe Heavy Alloys," *Proceedings of International Conference on Tungsten and Tungsten Alloy*s, Metal Powder Industries Federation, edited by A. Bose and R.J. Dowding, McLean, VA, 1992, pp. 397-405.

[35] J.W. Noh, E.P. Kim, H.S. Song, W.H. Baek, K.S. Churn, and S.J.L. Kang, "Matrix Penetration of W/W Grain Boundaries and Its Effect On Mechanical Properties of 93W-5.6Ni-1.4Fe Heavy Alloy," *Metallurgical and Materials Transactions A*, Volume 24 (1993) pp. 2411-2416.

[36] J.W. Noh, M.H. Hong, G.H. Kim, S.J.L. Kang, and D.Y. Yoon, "The Cause of Matrix Penetration of W/W Grain Boundaries During Heat Treatment of W-Ni-Fe Heavy Alloy," *Metallurgical and Materials Transactions A*, Volume 25 (1994), pp. 2828-283.

[37] H.S. Song, J.W. Noh, W.H. Baek, S.J.L. Kang, and B.S. Chun, "Undulation of W/Matrix Interface by Resintering of Cyclically Heat-Treated W-Ni-Fe Heavy Alloys," *Metallurgical and Materials Transactions A*, Volume 28 (1997), pp. 485-489.

[38] H.J Ryu and S.H. Hong, "Effects of Sintering Conditions on Mechanical Properties of Mechanically Alloyed Tungsten Heavy Alloys," *Key Engineering Materials*, Volumes 183-187 (2000), pp. 1291-1296.

[39] H.J. Ryu, S.H. Hong, and W.H. Baek, "Microstructure and Mechanical Properties of Mechanically Alloyed and Solid-State Sintered Tungsten Heavy Alloys," *Materials Science and Engineering A: Structural Materials: Properties, Microstructure and Processing*, Volume 291 (2000), pp 91-96.

[40] E. Fortuna, Z. Ludynski, K. Sikorski, K. Kurzydlowski, "Studies of the Correlation Between Microstructure and Toughness of Tungsten Alloys," Tungsten, Hard Metals, and Refractory Alloys 5 - 2000, Proceedings of the fifth International Conference on Tungsten, Hard Metals, and Refractory Alloys, Metal Powder Industries Federation, edited by M. Greenfield and J. Oakes, September 25-27, 2000, Annapolis, MD, pp. 63-70.

[41] H. Kolsky, "An Investigation of the Mechanical Properties of Materials at Very High Rates of Loading," *Proceedings of the Physical Society of London*, Sec. B, Vol. 62 (1949) pp. 676-700.

[42] T. Nicholas, "Dynamic Tensile Testing of Structural Materials Using a Split Hopkinson Bar Apparatus," Report AFWAL-TR-80-4053, 1980.

[43] S.J. Cimpoeru and R.L. Woodward, “High Strain Rate Properties of Three Liquid Phase Sintered Tungsten Alloys .” *Journal of Materials Science Letters*, Volume 9 (1990), pp. 187-191.

[44] J. Lankford, H. Couque, and A. Bose, “Dynamic Deformation and Failure of Tungsten Heavy Alloys,” *Tungsten and Tungsten Alloys - Recent Advances,”* edited by A Crowson and E. Chen, The Minerals, Metals & Materials Society, 1991, pp. 151-159.

[45] J. Lankford, A. Bose, and H. Couque, “High Strain Rate Behavior of Tungsten Heavy Alloys,” *High Strain Rate Behavior of Refractory Metals and Alloys*, edited by R. Asfahani, E. Chen and A. Crowson, The Minerals, Metals & Materials, Society, 1992, pp. 267-287.

[46] K.T. Ramesh, “The Influence of Tungsten Content, Swaging, and Grain Size on the Viscoplastic Response of Tungsten Heavy Alloys,” *High Strain Rate Behavior of Refractory Metals and Alloys*, edited by R. Asfahani, E. Chen and A. Crowson, The Minerals, Metals & Materials, Society, 1992, pp. 193-209.

[47] K.T. Ramesh and R.S. Coates, “Microstructural Influences on the Dynamic Response of Tungsten Heavy Alloys.” *Metallurgical Transactions A*, Volume 23 (1992), pp. 2625-2630.

[48] T. Weerasooriya and P.A. Beaulieu, “Deformation and Failure Behavior of 93W-5Ni-2Fe at Different Shear Strain Rate Loading,” *International Conference on Tungsten and Tungsten Alloys - 1992*, edited by A. Bose and R.J. Dowding, Metal Powder Industries Federation, Princeton, NJ, 1992, pp. 317-324.

[49] T. Weerasooriya, “Effects of Strain Rate on the Deformation and Failure Behavior of 93wt.%-5wt.%Ni-2wt.%Fe Under Shear Loading,” *Materials Science and Engineering A*, Vol. 172 (1993), pp. 71-78.

[50] M.M. LeBlanc and D.H. Lassila, "Dynamic Tensile Testing of Sheet Material using the Split Hopkinson Bar Technique," *Experimental Techniques*, January/February 1993, pp. 37-42.

[51] L.S. Magness Jr. and C. Lopatin, “Split Hopkinson Bar Compression Screening Tests of High Density Penetrator Materials,” *Thirteenth Army Symposium on Solid Mechanics Proceedings*, 17-19 August 1993, Plymouth, Massachusetts, pp. 633-644.

[52] T. Weerasooriya, “Effect of Sudden Change in Strain Rate on the Deformation and Failure Behavior of a Tungsten Heavy Alloy,” *Proceedings of the 2nd*

International Conference on Tungsten and Refractory Metals - 1994, edited by A. Bose and R.J. Dowding, Metal Powder Industries Federation, Princeton, NJ, 1994, pp. 455-462.

[53] T. Weerasooriya, P. Moy, and R.J. Dowding, "Effect of W-W Grain Contiguity on the High Shear Strain Rate Behavior of 93W-5Ni-2Fe Tungsten Heavy Alloy," *Proceedings of the 2nd International Conference on Tungsten and Refractory Metals - 1994*, edited by A. Bose and R.J. Dowding, Metal Powder Industries Federation, Princeton, NJ, 1994, pp. 401-409.

[54] H. Couque and J.D. Walker, "On the Use of the Compression Split Hopkinson Pressure Bar to High Strain Rate," *Journal De Physique IV*: Colloque C8, supplement au Journal de Physique III, Volume 4 (1994), pp. C8-23-28.

[55] T. Weerasooriya and L. Magness, "High Rate Testing of Kinetic Energy Penetrator Materials," *Metallurgical and Materials Applications of Shock-Wave and High Strain-Rate Phenomena*, edited by L.E. Murr, K.P. Staudhammer, and M.A. Meyers, 1995, pp. 895-899.

[56] W.S. Lee and S.T. Chiou, "The Influence of Loading Rate on Shear Deformation Behaviour of Tungsten Composite," *Composites* Part B: Engineering, Volume 27 (1996), pp. 193-200.

[57] E. El-Magd, H. Scholles, and H. Weisshaupt, "Dynamic Ductility of Metals," *Journal De Physique IV* , Vol. 7, Colloque C3, Supplement au Journal de Physique III (1997), pp. C3-349-354.

[58] T. Weerasooriya and P. Moy, "High Shear Strain Rate Behavior of W-Ni-Fe Tungsten Heavy Alloy Composites as a Function of Matrix Volume Fraction," U.S. Army Research Laboratory Technical Report ARL-TR-1694, May 1998.

[59] T. Weerasooriya, "Deformation Behavior of 93W-5Ni-2Fe at Different Rates of Compression Loading and Temperature, U.S. Army Research Laboratory Technical Report ARL-TR-1719, July 1998.

[60] H. Lips, M. Brodmann, and E. El-Magd, "Correlation Between Elongation at Fracture and Strain Rate for Dynamic Loading," *Journal De Physique IV*, Volume 10 (2000) pp. 371-376.

[61] T. Weerasooriya, Tensile Hopkinson Bar Results, Personal correspondence (email) dated April 2, 2002.

[62] J. Lankford, C.E. Anderson Jr, and S.R. Bodner, "Fracture of Tungsten Heavy Alloys Under Impulsive Loading Conditions," *Journal of Materials Science Letters*, Volume 7 (1988), pp. 1355-1358.

[63] L.S. Sigl and H.E. Exner. “Experimental Study of the Mechanics of Fracture in WC-Co Alloys,” *Metallurgical Transactions A*, Volume 18 (1987), pp. 1299-1308.

[64] H.E. Exner, L. Sigl, M. Fripan, and O. Pompe, “Fractography of Critical and Subcritical Cracks in Hard Materials,” *International Journal of Refractory Metals and Hard Materials*, Volume 19 (2001), pp. 329-334.

[65] J.H. Bechtold and P.G. Shewmon, “Flow and Fracture Characteristics of Annealed Tungsten,” *Transactions American Society for Metals*, Volume 46 (1954), pp. 397-407.

[66] G.E. Gazza, “Survey of the Deformation Characteristics of Tungsten,” DTIC Report AD610658, Metals and Ceramics Research Laboratories, U.S. Army Materials Research Agency, July 1963.

[67] D.H. Lassila and M.M. LeBlanc, “Deformation and Fracture Behavior of Tungsten-5% Rhenium and Unalloyed Tungsten Under Dynamic Tensile Loading,” High Strain Rate Behavior of Refractory Metals and Alloys, edited by R. Asfahani, E. Chen and A. Crowson, The Minerals, Metals & Materials, Society, 1992, pp. 157-165.

[68] A. Peikrishvili, L. Japaridze, G. Gotsiridze, N. Chikhradze, “Shock-wave Deformation of W-Ni-Fe Heavy Alloys at Elevated Temperatures, “Shock-wave and High-Strain-Rate Phenomena in Materials,” edited by M. A. Meyers, L.E. Murr, and K. P. Staudhammer, 1992, pp. 223-229.

[69] D.H. Lassila and G.T. Gray III, “Ductile-brittle Transition Behavior of Tungsten Under Shock Loading,” *Journal De Physique IV* : Colloque C8, supplement au Journal de Physique III, Volume 4 (1994), pp. C8-349 - C8-354.

[70] C. Tang, J. Zhu, and H. Zhou, ”Effect of Strain Rate on Ultimate Strength and Fractograph in Tungsten,” *Rare Metals*, Volume 17 (1998) pp. 198-202.

[71] Y. Xu and J. Zhu, “Temperature Effects on the Mechanical Properties and Fracture Surfaces of Tungsten Alloy,” *Hsi-An Chiao Tung Ta Hsueh/Journal of Xi'an Jiaotong University*, Volume 35 (2001) pp. 755-758.

[72] G. Nicolas and M. Voltz, “Tungsten Heavy Metal Alloys Relations Between the Crystallographic Texture and the Internal Stress Distribution, “ Internal Report No 188, Cime Boucuze, St. Pierre en Fuacigny, France, Subsidiary of Plansee AG.

[73] L. Ekbom and T. Antonsson, “Tungsten Heavy Alloy: Deformation Texture and Recrystallization of Tungsten Particles,” *International Journal of Refractory Metals and Hard Materials*, Volume 20 (2002), pp. 375-379

[74] A.A. Argon and S.R. Maloof, “Plastic Deformation of Tungsten Single Crystals at Low Temperatures,” *Acta Metallurgica*, Volume 14 (1966), pp. 1449-1462.

[75] W. J. Bruchey Jr., R.N. Herring, P.W. Kingman, and E.J. Horwath, “Deformation Mechanisms in Tungsten Single Crystals in Ballistic Impact Experiments,” High Strain Rate Behavior of Refractory Metals and Alloys, edited by R. Asfahani, E. Chen and A. Crowson, The Minerals, Metals & Materials, Society, 1992, pp. 145-155.

[76] E.J. Horwath and K.T. Ramesh, “The High Strain Rate Deformation of Tungsten Single Crystals,” *International Conference on Tungsten and Tungsten Alloys - 1994*, edited by A. Bose and R.J. Dowding, Metal Powder Industries Federation, Princeton, NJ, 1994, pp. 365-377.

[77] D. Hull, Fractography: Observing, Measuring, and Interpreting Fracture Surface Topography, Cambridge University Press, The Pitt Building, Trumpington Street, Cambridge, United Kingdom, 1999, p. 161.

[78] P. Gumbsch, J. Riedle, A. Hartmaier, and H.F. Fischmeister, “Controlling Factors for the Brittle-to-Ductile Transition in Tungsten Single Crystals, *Science*, Volume 282 (1998), pp. 1293-1295.

[79] J. Riedle, P. Gumbsch, H.F. Fischmeister, V.G. Glebovsky, and V.N. Semenov, “Cleavage Fracture and the Ductile-to-Brittle Transition of Tungsten Single Crystals,” *Materials Research Society Symposium Proceedings*, Volume 409, Fracture - Instability, Dynamics, Scaling, and Ductile/Brittle Behavior, Symposium, edited by R.L. Blumberg Selinger, J.J. Mecholsky, A.E. Carlsson, and E.R. Fuller, Jr., November 27-December 1, 1995, Boston, Massachusetts, U.S.A., pp. 23-28.

[80] J. Riedle, P. Gumbsch, and H.F. Fischmeister, “Cleavage Anisotropy in Tungsten Single Crystals,” *Physical Review Letters*, Volume 76 (1996) pp. 3594-3597.

[81] R.W. Margevicius, J. Riedle, and P. Gumbsch, “Fracture Toughness of Polycrystalline Tungsten Under Mode I and Mixed Mode I/II Loading,” *Materials Science and Engineering A*, Volume 270 (1999) pp. 197-209.

[82] W.S. Lee, C.F. Lin, and G.L. Xiea, “Dynamic Shear Deformation and Failure Behavior of Pure Polycrystalline Tungsten,” *Materials Science and Engineering A*, Volume 247 (1998) pp. 102-112.

[83] K. Sedlatschek and D.A. Thomas, “The Effect of Surface Treatment on the Mechanical Properties of Tungsten,” *Powder Metallurgy Bulletin*, Volume 8 (1957), pp. 35-50.

[84] Metals Handbook, Ninth Edition, Volume 5, Surface Cleaning, Finishing, and Coating, coordinated by W.G. Wood, American Society for Metals, Metals Park, Ohio, 1982, pp. 303-309.

[85] S.A. Syed and J.B. Pethica, " Nano Scale Creep and the Role of Defects," *Materials Research Society Symposium Proceedings*, Volume 436, Thin Films: Stresses and Mechanical Properties VI, April 8-12, 1996, edited by W.W. Gerberich, H. Gao, J.-E. Sundgren, and S.P. Baker, 1997, pp. 201-206.

[86] J.R. Stephens, An Exploratory Investigation of Some Factors Influencing the Room-Temperature Ductility of Tungsten, NASA Technical Note D-304, August 1960.

[87] J.R. Stephens, "Effect of Surface Condition on Ductile-to-Brittle Transition Temperature of Tungsten," Lewis Research Center, NASA Technical Note D-676, February 1961.

[88] K. Schroder, P. Packman, and V. Weiss, "Crack Initiation in Metallic Materials," Quarterly Report No. 3 for Dept. of the Navy, Bureau of Naval Weapons, Washington 25, D.C, Metallurgical Research Laboratories, Department of Chemical Engineering and Metallurgy, Syracuse University, MET E. 1040-63008Q3, August 1963.

[89] V. Weiss, K. Schroder, P. Packman, and J.G. Sessler, "Crack Initiation in Metallic Materials," Final Report for Dept. of the Navy, Bureau of Naval Weapons, Washington 25, D.C, Syracuse University Research Institute, Department of Chemical Engineering and Metallurgy, MET 878-6211-F, November 1962.

[90] A.P. Valentine and D. Hull, "Effect of Temperature on the Brittle Fracture of Polycrystalline Tungsten," *Journal of the Less-Common Materials*, Volume 17 (1969), pp. 353-361.

[91] A.M. Lennon and K.T. Ramesh, "The Thermoviscoplastic Response of Polycrystalline Tungsten in Compression," *Materials Science and Engineering*, Volume A276 (2000), pp. 9-21.

[92] L.E. Peterson, P.A. Guarino, and E.A. Coomes, "Electrolytic Polishing of Tungsten," *Physical Review*, Volume 57 (1940) p. 1081.

[93] W.E. Gurwell, M.R. Garnich, G.B. Dudder, and C.A. Lavender, "Bend Ductility of Tungsten Heavy Alloys," *Proceedings of the First International Conference on Tungsten and Tungsten Alloys - 1992*, Nov 15-18 1992, Arlington, VA, USA, 1992, pp. 221-232.

[94] B,H, Rabin, "Microstructure and Tensile Properties of Liquid Phase Sintered Tungsten-Nickel-Iron Composites, Ph.D. Dissertation, Rensselaer Polytechnic Institute, Troy, New York, 1986.

[95] E. El-Magd, H. Scholles, H. Weisshaupt, "Dynamic Ductility of Metals," *Journal de Physique Colloque C3, Supplement au Journal de Physique III*, Volume 7 (1997) pp. 349-354.

[96] S.W. Jung, D.K. Kim, S. Lee, J.W. Noh, and S.J.L. Kang, "Effect of Surface Carburization on Dynamic Deformation and Fracture of Tungsten Heavy Alloys," *Metallurgical and Materials Transactions A*, Volume 30A (1999), pp. 2027-2035.

[97] T.W. Bjerke, G.F. Silsby, D.R. Scheffler, and R.M. Mudd, "Yawed Long-Rod Armor Penetration," *International Journal of Impact Engineering*, Volume 12 (1992) pp. 281-292.

[98] D.J. Gee and D.J. Littlefield, "Yaw Impact of Rod Projectiles," *International Journal of Impact Engineering*, Volume 26 (2001) pp. 211-220.

[99] S. Satapathy, A. Bedford, and S. Bless, "Behavior of a Yawed Projectile Penetrating a Thin Plate," *International Journal of Impact Engineering*, Volume 1 (1998) pp. 597-608.

[100] S. Satapathy and S. Bless, "Response of Long Rods to Moving Lateral Pressure Pulse: Numerical Evaluation in DYNA3D," *International Journal of Impact Engineering*, Volume 26 (2001) pp. 663-674.

[101] D.J. Gee, "Plate Perforation by Eroding Rod Projectiles," *International Journal of Impact Engineering*, Volume 28 (2003) pp. 377-390.

[102] S. Satapathy, C. Persad, R.M. Gee, and S. Bless, "Gouging Induced Fractures in Tungsten Long Rods," *International Journal of Impact Engineering*, Volume 29 (2003), pp. 621-630

[103] S.J. Bless, S. Satapathy, and M. Normandia, " Transverse Loads on a Yawed Projectile, " *International Journal of Impact Engineering*, Volume 23 (1999) pp. 77-86.

[104] J.M. McGlaun and S.L. Thompson, "CTH: A Three-Dimensional Shock Wave Physics Code," *International Journal of Impact Engineering*, Volume 10 (1990), pp. 351-360.

[105] R.G. Whirley and B.E. Engelmann, "DYNA3D: A Nonlinear, Explicit Three-Dimensional Finite Element Code for Solid and Structural Mechanics - User Manual," Report UCRL-MA-107254, Lawrence Livermore National Laboratory, Livermore, CA, November 1993.

[106] G.R. Johnson, Gordon R. and W.H. Cook, "A Constitutive Model and Data for Metals Subjected to Large Strains, High Strain Rates and High Temperatures,

"*Proceedings of the 7th International Symposium on Ballistics,*" The Hague, The Netherlands, April 19-21, 1983, pp. 541-547.

[107] F.J. Zerilli and R.W. Armstrong, "Dislocation-Mechanics-Based Constitutive Relations for Material Dynamic Calculations," *Journal of Applied Physics*, Volume 51 (1987), pp. 1816-1825.

[108] V. Ramachandran, R.W. Armstrong, and F.J. Zerilli, "Dislocation Mechanics Based Constitutive Equations for Tungsten Deformation and Fracturing," *Tungsten and Tungsten Alloys - Recent Advances*, edited by A. Crowson and E. Chen, The Minerals, Metals & Materials Society, 1991, pp. 111-119.

[109] D. Fuentes, Personal correspondence (email) dated June 26, 2003.

[110] A.A. Griffith, "The Phenomena of Rupture and Flow in Solids," *Philosophical Transactions of the Royal Society of London,* Series A, Volume 221 (1921), pp. 163-198.

[111] D. Rittel and G. Weisbrod, "Dynamic Fracture of Tungsten Base Heavy Alloys," *International Journal of Fracture*, Volume 212 (2001) pp. 87-98.

[112] R.G. O'Donnell and R.L. Woodward, "The Composition and Temperature Dependence of the Mechanical Properties of Tungsten Alloys," *Metallurgical Transactions A*, Volume 21 (1990), pp. 744-748.

[113] R.L. Woodward and R.G. O'Donnell, R.G., "Microstructural Influences on the Ductility of Tungsten Alloys," *Tungsten and Tungsten Alloys - 1992, Proceedings of the first International Conference on Tungsten and Tungsten Alloys*, Metal Powder Industries Federation, edited by A. Bose and R.J. Dowding, McLean, VA, 1992, pp. 389-396.

[114] R.L. Woodward, and R.G. O'Donnell, "Tensile Rupture of Tungsten Alloys by the Cascade of Crack Nucleation Events," *Journal of Materials Science*, Volume 35 (2000), pp. 4067-4072.

[115] R.G. O'Donnell and R.L. Woodward, "Influence of Temperature on the Fracture of a W-Ni-Fe Alloy," *Journal of Materials Science*, Volume 35 (2000), pp. 4319-4324.

[116] A.J. Bush, "Experimentally Determined Stress-Intensity Factors for Single-Edge-Crack Round Bars Loaded in Bending," *Experimental Mechanics*, Volume 16 (1971), pp. 249-257.

[117] R.N. Johnson, "Fracture of a Cracked Solid Circular Cylinder," Ph.D. Dissertation, University of Wisconsin, June 1972.

[118] W.S. Blackburn, “Calculation of Stress Intensity Factors for Straight Cracks in Grooved and Ungrooved Shafts,” *Engineering Fracture Mechanics*, Volume 8 (1976), pp. 731-736.

[119] A.J. Bush, “Stress Intensity Factors for Single Edge-Crack Solid and Hollow Round Bars Loaded in Tension,” *Journal of Testing and Evaluation*, Volume 9 (1981), pp. 216-223.

[120] O.E.K. Daoud and D.J. Cartwright, “Strain Energy Release Rates for a Straight-Fronted Edge Crack in a Circular Bar Subject to Bending,” *Engineering Fracture Mechanics*, Volume 19 (1984), pp. 70-707.

[121] O.E.K. Daoud and D.J. Cartwright, “Strain Energy Release Rates for a Circular-Arc Edge Crack in a Bar Under Tension or Bending,” *Journal of Strain Analysis*, Volume 30 (1985), pp. 53-58.

[122] C. Mattheck, P. Morawietz, and D. Munz, “Stress Intensity Factors of Sickle-Shaped Cracks in Cylindrical Bars,” *International Journal of Fatigue*, Volume 7 (1985), pp 45-47.

[123] R.G. Forman and V. Shivakumar, “Growth Behavior of Surface Cracks in the Circumferential Plane of Solid and Hollow Cylinders,” Fracture Mechanics: Seventeenth Volume, ASTM STP 905, J.J. Underwood, R. Chait, C.W. Smith, D.P. Wilhelm, W.A. Andrews, and J.C. Newman, Eds., American Society for Testing and Metals, Philadelphia, 1986, pp. 59-74.

[124] I.S. Raju and J.C. Newman, “Stress-Intensity Factors for Circumferential Surface Cracks in Pipes and Rods Under Tension and Bending Loads,” Fracture Mechanics: Seventeenth Volume, ASTM STP 905, J.J. Underwood, R. Chait, C.W. Smith, D.P. Wilhelm, W.A. Andrews, and J.C. Newman, Eds., American Society for Testing and Metals, Philadelphia, 1986, pp. 789-805

[125] T. Lorentzen, N. Kjaer, and T. Henriksen, “The Application of Fracture Mechanics to Surface Cracks in Shafts,” *Engineering Fracture Mechanics*, Volume 23 (1986), pp. 1005-1014.

[126] C.K. Ng and D.N. Fenner, “Stress Intensity Factors For an Edge Cracked Circular Bar in Tension and Bending,” *International Journal of Fracture*, Volume 36 (1986), pp. 291-303.

[127] K.J. Nord and T.J. Chung, “Fracture and Surface Flaws in Smooth and Threaded Round Bars,” *International Journal of Fracture*, Volume 30 (1986), pp. 47-55.

[128] Y. Murakami (Editor-in-Chief), Stress Intensity Factors Handbook, Committee on Fracture Mechanics, The Society of Materials Science, Japan (1987), pp. 654-665.

[129] J.H. Underwood, F.I. Baratta, and J.J. Zalinka, “Fracture-Toughness Tests and Displacement and Crack-Stability Analyses of Tungsten Round Bend Specimens,” *Experimental Mechanics*, Volume 31 (1991), pp. 353-359.

[130] A. Carpinteri, “Stress Intensity Factors for Straight-Fronted Edge Cracks in Round Bars,” *Engineering Fracture Mechanics*, Volume 42 (1992), pp. 1035-140.

[131] A. Carpinteri, “Elliptical-Arc Surface Cracks in Round Bars,” *Fatigue Fracture of Engineering Material Structures*, Volume 15 (1992), pp. 1141-115

[132] F.I. Baratta, “Wide Range Stress Intensity Factors for a Straight-Fronted Edge Crack in a Three-Point, Round Bar Specimen,” *International Journal of Fracture*, Volume 60 (1993), pp. R59-R63.

[133] F.I. Baratta, “Stability Revisited for a Straight-Fronted Edge Crack in a Three-Point Loaded Round Bend Bar,” *International Journal of Fracture*, Volume 62 (1993), pp. R29-R35.

[134] J.H. Underwood, “Stress Intensity Factor and Load-Line Displacement Expressions for the Round Bar Bend Specimen,” *International Journal of Fracture*, Volume 62 (1993), pp. R49-R55.

[135] M. da Fonte and M. de Frietas, “Stress Intensity Factors for Semi-Elliptical Surface Cracks in Round Bars Under Bending and Torsion, *International Journal of Fatigue*, Volume 21 (1999), pp. 457-463.

[136] N. Couroneau and J. Royer, “Simplifying Hypotheses for the Fatigue Growth Analysis of Surface Cracks in Round Bars,” *Computers and Structures*, Volume 77 (2002), pp. 381-389.

[137] V.C. Chan, “A New Test Technique to Measure Resistance to Dynamic Fracture of Tungsten Alloys,” Master of Science Thesis, Department of Mechanical Engineering, University of Texas at Austin, August 1999.

[138] S.N. Chang and J.H. Choi, “High Strain Rate Response of a Tungsten Heavy Alloy,“ *Shock Compression of Condensed Matter - 1997*, Proceedings of the Conference of the American Physical Society Topical Group on Shock Compression on Condensed Matter, July 27-August 1, 1997, edited by S.C. Schmidt, D.P. Dandekar, and J.W. Forbes, American Institute of Physics, 1998, pp. 415-418.

[139] S. Satapathy, J. Cazamias, S. Bless, R. Gee, L. Meyer, and S. Brar, “Dynamic Strength of Tungsten-Nickel-Cobalt Alloys,” *Shock Compression of Condensed Matter – 1999*, Proceedings of the 1999 Topical Conference on Shock Compression of Condensed Matter, June 27-July 2, 1999, edited by M.D. Furnish,

L.C. Chhabildas, and R.S. Hixson, American Institute of Physics, 2000, pp. 463-466.

[140] K. Dannemann and J.D. Walker, “Evaluation of Tungsten Alloy Rods,” Final Report, Southwest Research Institute Project 18-03562, prepared for the University of Texas Institute for Advanced Technology, May 2000.

[141] H.S. Song, E.P. Kim, S. Lee, J.W. Noh, and W.H. Baek, “The Effect of Ni/Fe Ratio on the Mechanical Properties for Tungsten Heavy Alloy,” *Advances in Powder Metallurgy & Particulate Materials - 1992*, Volume 6, Non-Ferrous Materials, Proceedings of the 1992 Powder Metallurgy World Congress sponsored by the Metal Powder Industries Federation and APMI International, June 21-26 1992, San Francisco, CA, 1992, pp. 77-83.

[142] S.H. Hong, H.J. Ryu, E.P. Kim, and W.H. Baek, “Impact and Dynamic Deformation Behavior of Mechanically Alloyed Tungsten-Based Composites, *Materials*, Volumes 141-143 (1998), pp. 453-462.

[143] S.W. Jung, D.K. Kim, S. Lee, J.W. Noh, and S.J.L. Kang, “Effect of Surface Carburization on Dynamic Deformation and Fracture of Tungsten Heavy Alloys,” *Metallurgical and Materials Transactions A*, Volume 30 (1999), pp. 2027-2035.

[144] H.J. Ryu and S.H. Hong, “Effects of Sintering Conditions on Mechanical Properties of Mechanically Alloyed Tungsten Heavy Alloys,” *Key Engineering Material*s, Volumes 183-187 (2000), pp. 1291-1296.

[145] H.J. Ryu, S.H. Hong, W.H. Baek, and H. Woon, “Microstructure and Mechanical Properties of Mechanically Alloyed and Solid-State Sintered Tungsten Heavy Alloys,” Materials *Science and Engineering A: Structural Materials: Properties, Microstructure and Processing*, Volume 291 (2000) pp. 91-96.

[146] J.M. Hughes and E.A. Coomes, “Electrolytic Polishing of Tungsten,” *Physical Review*, Volume 55 (1938) p. 1138.

[147] S.A. Syed, and J.B. Pethica, “Nano Scale Creep and the Role of Defects,” Materials Research Society Symposium Proceedings, Vol. 436, *Thin Films: Stresses and Mechanical Properties* VI, April 8-12, 1996, San Francisco, U.S.A., edited by W.W. Gerberich, H. Gao, J.-E. Sundgren, and S.P. Baker, 1997, pp. 201-206.

[148] J. Tousek, “Electropolishing of Tungsten in Acid Baths, “*Physical Metallurgy* (Brno, Czech), translated from *Praktische Metallographie*, Volume 21 (1984), pp. 552-555.

[149] P. Sachenko, J.H. Schneibel, and W. Zhang, “Effect of Faceting on the Thermal Grain-Boundary Grooving of Tungsten,” Philosophical *Magazine A*, Volume 82 (2002), pp. 815-829.

[150] N.V. Bogoyavlenskaya and V.P. Zhuravel, “Investigation of the Process of Electropolishing of Tungsten-Rhenium Alloys,” *Protection of Metals*, Volume 12:1 (1976), pp. 87-88.

[151] B.M. Rovinskii, Y.V. Baranov, and E.P. Kostyukova, “Effect of the Polishing Medium on the Nature of the Substructure in the Deformation of Tungsten Single Crystals,” *Soviet Physics, Solid State* (English translation of *Fizika Tverdogo Tela*), Volume 16 (1975), pp. 2087-2089.

[152] E. Kennedy, “Influence of Microstructure on Fracture Characteristics and Tensile Properties of Two Tungsten Heavy Alloys,” *Proceedings of the 2nd International Conference on Tungsten and Refractory Metals - 1994,* edited by A. Bose and R.J. Dowding, Metal Powder Industries Federation, Princeton, NJ, 1994, pp. 101-110.

[153] D. Hull and P. Beardmore, “Velocity of Propagation of Cleavage Cracks in Tungsten,” *International Journal of Fracture Mechanics,* Volume 2 (1966) pp. 468-487.

[154] J.E. Cordwell and D. Hull, “Brittle Fracture of [100] Axis Tungsten Single Crystals, *Philosophical Magazine*, Volume 19 (1969), pp. 951-66.

[155] D. Hull, P. Beardmore, and A.P. Valentine, ”Crack Propagation in Single Crystals of Tungsten.” *The Philosophical Magazine*, Volume 12 (1965), pp. 1021-1041.

[156] J.E. Cordwell and D. Hull, “The Brittle Fracture of [100] Axis Tungsten Single Crystals,” *The Philosophical Magazine*, Volume 19 (1969), pp. 951-966.

[157] K. Ravi-Chandar and B. Yang, “On the Role of Microcracks in the Dynamic Fracture of Brittle Materials,” *Journal of the Mechanics and Physics of Solids*, Volume 42 (1997), pp. 535-563.

[158] D. Hull, “Tilting Cracks: The Evolution of Fracture Surface Topology in Brittle Solids,” *International Journal of Fracture*, Volume 62 (1993), pp. 119-38.

[159] D. Hull, “The Effect of Mixed Mode I/III on Crack Evolution in Brittle Solids,” *International Journal of Fracture*, Volume 70 (1995), pp. 59-79.

[160] D. Hull, “Influence of Stress Intensity and Crack Speed on Fracture Surface Topography: Mirror to Mist Transition,” *Journal of Materials Science*, Volume 31 (1996), pp. 1829-41.

[161] D. Hull, "Influence of Stress Intensity and Crack Speed on Fracture Surface Topography: Mirror to Mist to Macroscopic Bifurcation, *Journal of Materials Science*, Volume 31 (1996), pp. 4483-92.

[162] T.L. Bjerke, Personal correspondence (emails) dated February 2 and September 9, 2003.

[163] Struers homepage web address: http://www.struers.com.

[164] G. F. Vander Voort, Metallography : Principles and Practice, Materials Park, Ohio, ASM International, 1999, pp. 632, 697.

[165] E.E. Underwood, Quantitative Stereology, Addison-Wesley Publishing Company, Inc., Reading, Massachusetts, 1970, p. 29.

[166] National Institutes of Health ImageJ website: http://rsb.info.nih.gov/ij/.

[167] N.J. Petch, "The Cleavage Strength of Polycrystals," Journal of the Iron and Steel Institute, Volume 174 (1953), pp. 25-28.

[168] M.F Ashby, *Philosophical Transactions of the Royal Society of London*, Volume 22 (1975), pp. 75-198.

[169] T. Baumeister, Mark's Standard Handbook for Mechanical Engineers, Eighth Edition, McGraw-Hill Book Company, New York, 1978, pp. 13-71.

[170] B. Geisler, "Instrumented Impact Tester," University of Houston, Department of Mechanical Engineering, Houston, Texas, April 1996.

[171] ASTM E 23-02, "Standard Test Methods for Notched Bar Impact Testing of Metallic Materials," approved May 10, 2002.

[172] A. Higdon, E.H. Ohlsen, W.B. Stiles, J.A. Weese, and W.F. Riley, Mechanics of Materials, John Wiley & Sons, Inc., New York, 1976, p. 348.

[173] K. Ravi-Chandar, "Dynamic Loading and Crack Arrest," CMSSM Report Number 02-10, Center for Mechanics of Solids, Structures, & Materials, The University of Texas at Austin, December 4, 2002, p. 21.

[174] R.A. Wullaert, "Applications of the Instrumented Charpy Impact Test," ASTM STP 466, Impact Testing of Metals, A symposium presented at the Seventy-second Annual Meeting for the American Society for Testing and Materials, Atlantic City, NJ, 22-27 June 1969, 1970, pp. 148-164.

[175] Y.I Zvezdin, A.A. Popov, A.B. Karaev, Y.G. Dragunov, B.A. Sugerbecov, and A.S. Sokolov, "Method for Structural Material Critical Brittle Temperature

Evaluation Based on Instrumented Charpy Impact Test Analysis," Fracture Mechanics Verification by Large-Scale Testing, Mechanical Engineering Publications Ltd., London, 1991, pp. 401-407.

[176] J.M. Gere and S. P. Timoshenko, Mechanics of Materials, Second Edition, Wadsworth, Inc. Belmont, CA, 1984, p. 515.

[177] J.N. Price and D. Hull, "Propagation of Stress Corrosion Cracks in Aligned Glass Fibre Composite Materials," *Journal of Materials Science*, Volume 18 (1983), pp. 2798-2810.

[178] W. Gray, S. Mullin, H, Couque, and Neil Blaylock, "Heavy Metal Fragment Effects with Light Armor," Table 11, prepared by Southwest Research Institute for the U.S. Air Force AFATL, Eglin Air Force Base, Florida, Project 06-2494, September 1990.

[179] R. Subramanian, S.J. Bless, J. Cazamias, and D. Berry, "Reverse Impact Experiments Against Tungsten Rods and Results for Aluminum Penetration Between 1.5 and 4.2 km/s," *International Journal of Impact Engineering*, Volume 17 (1995), pp. 817-824.

[180] A.C. Mueller and E.M. Fernando," The Dynamics of Projectiles Launched by a Two-Stage Light-Gas Gun," DTIC Report AD-A274 380, Arnold Engineering Development Center, Arnold Air Force Base, Tennessee, November 1991.

[181] R. Russell, K. Tarcza, H. Hart, S. Bless, and D. Fuentes, "Reverse Ballistic Experiment Demonstrates Varying Performance of Long Rod Penetrators," presented at the 54th Meeting of the Aeroballistic Range Association (ARA), Santa Fe, New Mexico, October 19-24, 2003.

[182] K. R. Tarcza, R.T. Russell, D.T. Fuentes, S.J. Bless, and E.M. Taleff, "Transverse Loading of Tungsten Alloy Rods via Reverse Ballistic Experiments," *Proceedings of the SME Annual Conference on Experimental and Applied Mechanics*, June 2-4, 2003, Charlotte, North Carolina.

[183] R.D.M. Tachau," An Investigation of Gouge Initiation in High-Velocity Sliding Contact," Ph.D. Dissertation, Department of Aerospace Engineering and Engineering Mechanics, University of Texas at Austin, August 1991.

[184] K.R. Tarcza and W.F. Weldon, "Metal Gouging at Low Relative Sliding Velocities, *Wear*, Volume 209 (1997), pp. 21-30

[185] F. Stefani and J.V. Parker, "Experiments to Measure Gouging Threshold Velocity for Various Metals Against Copper," *IEEE Transactions on Magnetics*, Volume 35 (1999), pp. 312-316.

[186] D.J. Laird, “The Investigation of Hypervelocity Gouging, Ph.D. Dissertation, Air Force Institute of Technology, Wright-Patterson Air Force Base, Ohio, March 2002.

[187] G.R. Abrahamson, “Permanent Periodic Surface Deformations Due to a Traveling Jet,” *Journal of Applied Mechanics*, Volume 83 (1961), pp. 519-528.

[188] D. Littlefield and D. Fuentes, Personal correspondence (numerous emails and meetings).

[189] W. Rostoker and J.R. Dvorak, Interpretation of Metallographic Structures, 3rd Edition, Academic Press, Inc., 1990, p. 19.

[190] K.E. Graff, Wave Motion in Elastic Solids, Dover Publications Inc., New York, copy write 1975 by Oxford University Press, pp. 277, 326.

[191] O. Younes and E. Gileadi, “Electroplating of High Tungsten Content Ni/W Alloys,” *Electrochemical and Solid-State Letters*, Volume 3 (2000), PP. 543-545.

[192] O. Younes, L. Zhu, Y. Rosenberg, Y. Shacham-Diamand, and E. Gileadi, “Electroplating of Amorphous Thin Films of Tungsten/Nickel Alloys, *Langmuir*, Volume 17 (2001), pp. 8270-8275.

Vita

Kenneth Robert Tarcza was born in Falls Church, Virginia on September 9, 1963, the son of Robert and Elsie Tarcza and the grandson of Hungarian immigrants. After graduating from George C. Marshall High School in 1981, he entered the United States Military Academy, graduating in May 1985 with a Bachelor of Science in Mechanical Engineering and was commissioned as a Second Lieutenant of Armor. After an assignment in Schweinfurt, (West) Germany where he met his future wife, he returned the United States and married the former Margaret Elizabeth Smith on July 1, 1989. Subsequent assignments took them to: Fort Knox, Kentucky; Fort Hood, Texas, where he was deployed to Southwest Asia for Operations Desert Shield and Desert Storm; Austin, Texas, where he earned a Master of Science degree in Mechanical Engineering from the University of Texas at Austin; West Point, New York; Fort Leavenworth, Kansas; and most recently to Picatinny Arsenal, New Jersey. In August 2001, he reentered the Graduate School of the University of Texas at Austin on the Army's Advanced Civil Schooling program. He is currently a Lieutenant Colonel in the United States Army and a member of the Army Acquisition Corps. He is also follower of Jesus Christ, a devoted husband, and the proud father of Anna and Aaron.

Permanent address: 10108 Crooked Creek Court
Fairfax Station, Virginia 22039

This dissertation was typed by the author.